Faculty of Science & Technology

Engineering Department

THIRD YEAR BEng PROJECT

‘Radiotherapy Linac Design’

James Alexander Mitchell

Supervisor: Dr Graeme Burt

June 2015

Lancaster University

Faculty of Science and Technology

Engineering Department

Signed Declaration on the Submission of a Project

I declare that this project is my own work and has not been submitted in substantially the same form towards the award of a degree or other qualificatory work, and affirm that acknowledgement has been made to assistance given and that all major sources have been appropriately referenced.

Signed: ……

Date: ……

ACKNOWLEDGEMENTS

The research supervisor for this project, Dr Graeme Burt, devoted much of his time and effort to assist in the completion of this project. I would like to express my gratitude for his continued support and feedback.

Furthermore, Lancaster University's engineering technician, Jonathan Gates, dedicated a large amount of time to the complex construction of the linear accelerator section. His help and enthusiasm during the build stage of this project was a huge contribution to its overall success.

I would also like to thank the RF group at the Cockcroft Institute for allocating time to help with the professional Bead-Pull measurements conducted after the measurements at Lancaster University were taken.

SUMMARY

An application of particle accelerators, and therefore an area of interest for the accelerator engineer, is cancer therapy. By directing a charged particle at cancerous tissue, it is possible to damage the cells and remove the cancer.

Specifically, it is possible to use a radio frequency (RF) linear accelerator (linac) in order to accelerate the charged particle to a specific energy. There are an array of particles available for acceleration, but a particle of much interest in the area of cancer therapy is the proton. The proton possesses characteristics which make it ideal for irradiating cancers without harming surrounding tissues, as explained in further detail in the literature review section of this report. Protons also have a lower likelihoods of secondary cancers arising when compared with other charged particles. For these reasons therapy using protons, or hadron therapy, has applications in treating cancers near vital organs and as a treatment for children.

Due to the applications of RF linear accelerators for hadron therapy, this project will consist of the design, build and test of an RF linac cavity. The cavity is the void within the accelerator which is responsible

for accelerating the charged particles, in this case protons, and specifically an RF cavity uses radio frequencies to transfer electromagnetic energy to the particle beam.

The cavity will firstly be virtually designed using the software package CST Microwave Studio (CST MWS). At this stage the cavity will be optimised iteratively in order to produce a structure which is capable of efficiently accelerating a beam of protons at the required energy. Several figures of merit will be calculated throughout the optimisation stage and these values will be developed, allowing them to act as assessments of the cavity's performance in order for comparison with existing structures and to use as references for improvements.

Following the design stage, the metallic structure which will house the designed cavity will be implemented using the computer aided design (CAD) program SolidWorks and a metallic structure will be built using a computerised numerical control (CNC) lathe. The physical structure will then be tested in the RF laboratory and the results will be compared to the values returned virtually from simulations in CST MWS.

CONTENTS

LIST OF FIGURES

LIST OF TABLES

CHAPTER 1 – LITERATURE REVIEW

Reading and evaluating existing resources allowed a literature review detailing key concepts surrounding 'Radiotherapy Linac Design' to be produced. The review sets out to establish a foundation of knowledge in areas of importance to the field, in order to maximise progress by eliminating basic research in later stages of the project.

1 History of the Linear Accelerator

The invention and evolution of the linear accelerator (linac) are both factors that can be put down to a multitude of scientific discoveries and historical events. This section details these happenings and the results that arose from them.

In the early 20th century, scientist's dreams of breaking down nuclei created a demand for particle accelerators. This demand spawned from Ernest Rutherford's famous experiment where the constituents of a Nitrogen (N) nucleus were disunited by alpha particles (α) emitted from the radioactive decay of Radium (Ra) and Thorium (Th). In 1927 Rutherford, in a speech given at the Royal Society, went on to ask for machines capable of accelerating a source to multiple MeV, in order to break down heavier nuclei [1], [2].

In 1924, prior to Rutherford's Speech, a Swedish physicist named Gustav Ising proposed an accelerator that utilised time varying fields. The accelerator design consisted of a straight vacuum tube and several drift tubes with holes to allow a particle beam to pass through. Pulsed voltages were to be applied across the drift tubes which would, in turn, accelerate the particles. This type of accelerator is now known as a 'true accelerator', which means it is able to achieve energies above the highest energy received from the input voltage [2]. His proposal sparked the interest of a Norwegian student named Rolf Wideröe [3].

In 1927 Wideröe proceeded to design and exhibit the first Radio Frequency (RF) linear accelerator known as the drift-tube linac (DTL), Section 5.5.1. This design incorporated a 1 MHz, 25 kV oscillator

which was capable of making 50 KeV Potassium (K) Ions. Wideröe's design was the first conventional linac [2]. The high frequencies required to accelerate protons were not possible due to the available drift tubes and circuit losses [1].

Wideröe's designs and progress in the field encouraged Ernest Lawrence to work more on RF acceleration and this resulted in a DTL, designed by himself and David H. Sloan, which consisted of 30 drift tubes and was able to accelerate heavy ions [3], [1] . The frequency of the linac however, could not be increased to a value high enough to accelerate high energy light proton and electron beams [3].

The demand for Radar systems during World War 2 (WWII) incurred huge advancements in high frequency power generation [3]. These advancements were utilised by Luis Alvarez who, in 1947, built a DTL which was capable of operating at much higher frequencies and energies, 200 MHz and 32 MeV respectively [2]. Hence Alvarez's linac was able to accelerate proton beams [1].

The next year Edward Ginzton, William Hansen and W. Kennedy established the first electron linac which consisted of an array of pillbox cavities [3]. The assembly was known as an iris-loaded waveguide due to the propagation holes in each wall [1].

2 Basic Concepts Surrounding the Linear Accelerator

Since Wideröe's first accelerator, a lot of progress has been made which has given rise to a multitude of linear accelerators which differ in design and purpose. The development of the linear accelerator can be put down to a set of distinct advantages over other accelerator types [3]:

- High quality charged particle beams can be produced with high energies and intensities. They are very favourable when a small beam diameter and energy spread are required.
- Confinement of the beam can be achieved easily as linear accelerators can provide strong focusing.
- They have an advantage over synchrotrons as the beam travels in a straight line meaning there is no power loss from synchrotron radiation.
- Repetitive error conditions are avoided as the beam only passes each accelerating structure once.
- They provide a much simpler method of beam injection and extraction.
- Acceleration at any duty factor is possible.

It is possible to sort linear accelerators into 2 general categories [4]:

- Linear accelerators with cells that increase in length in order to correspond with the increase in beam velocity in a precise manner. This is typical of a low energy linear accelerator.
- Linear accelerators with an array of identical accelerating cells. This design is utilised in high energy accelerators.

3 Basic Operations and Structures of the RF Linac

This paper is concerned with the design and optimisation of RF cavities and for this reason RF linear accelerators are the focus of this review.

In a linear accelerator charged particles are accelerated by obtaining energy from an external source and the particles definitively only pass each accelerating structure on one occasion [4]. In the case of the RF linac this energy is provided by a radio-frequency electromagnetic field that has a harmonic time dependence, giving the charged particles momentum [3], [5]. Acceleration is due to an electric field component changing the energies of the charged particles and transverse focusing is due to a magnetic field, resulting from the presence of external magnets, changing the direction of the particle velocity [6].

RF linacs are categorised as 'resonance accelerators' as the particles move in resonance with the driving electromagnetic wave. Today's linacs generally consist of an array of accelerating structures of which there are two main types. Either the linac will consist of several segments of waveguide or it will have an array of high-Q, Section 5.1, resonant cavities. In the case of the resonant cavity design, of which this paper is concerned, a radio-frequency electromagnetic field acts to excite these accelerating structures. The cavities are tuned to resonance and a source of RF power is applied (often this power comes from a klystron, discussed further in Section 5.5.2.3). Transmission lines or waveguides transport the radio-frequency electromagnetic waves to the main linac cavity array. The cavities then transfer the energy arising from these waves to the charged particles in order for acceleration to take place as described in the previous paragraph [3].

In order to understand the above general workings of an RF cavity linac it is helpful to view it as a series of processes, where the results of these processes are inputted into the main linac structure in order to accelerate charged particles. This is demonstrated visually in the block diagram shown in Figure 1.

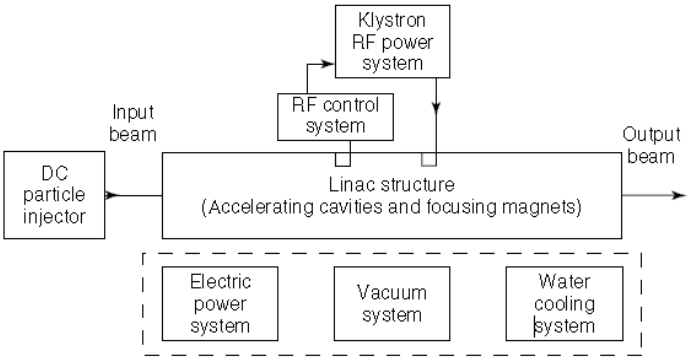

Figure 1 - Block Diagram Representing RF Linac Operation [3]

Figure 1 shows an electric power system, a vacuum system and a water cooling system. These have not been described in the previous two paragraphs. The electric power system provides power to the linac, the majority of which goes to the RF power system. The vacuum system enables good beam transmission and the cooling system removes heat generated by resistive wall losses [3].

4 Proton RF Linacs and their Applications to Hadrontherapy

As this project will concern itself mostly with the design of an RF cavity for a linac capable of accelerating protons for applications in hadrontherapy, an important area of research is that of the proton RF linac.

Proton linacs are used in a range of different areas and have a variety of different applications. These applications consist of:

- Particle physics research using high energy synchrotrons use proton accelerators to inject the particle at speed during the initial stages.
- Continuous wave neutron sources can be provided by proton linacs. Applications arising from the neutron sources are: for use nuclear fuel production, fission reactors, the transmutation of nuclear waste, condensed matter research and irradiation studies.
- Boron neutron capture therapy (BNCT) uses low energy neutrons which can be formed with the use of a proton linac.
- Proton therapy, a subcategory of hadron therapy, uses these linacs for cancer treatment [3].

Concentrating on the last point, hadron therapy has distinct advantages when compared to other types of radiotherapy. This is mainly due to the characteristics of the charged particles, in this case protons, which are used to attack the cancerous cells. When travelling, a proton is not absorbed by tissue, instead it deposits its energy at a rate that is inversely proportional to the quantity of energy it possesses. This means that the highest amount of energy is deposited at the end of the proton's path, allowing most of the energy to be deposited at the location of the cancerous tissue. This characteristic means that tissue surrounding the target volume [7] is much less affected than if an electron were used. The area of high dose energy deposition is called the Bragg peak and is represented graphically in Figure 2 [8].

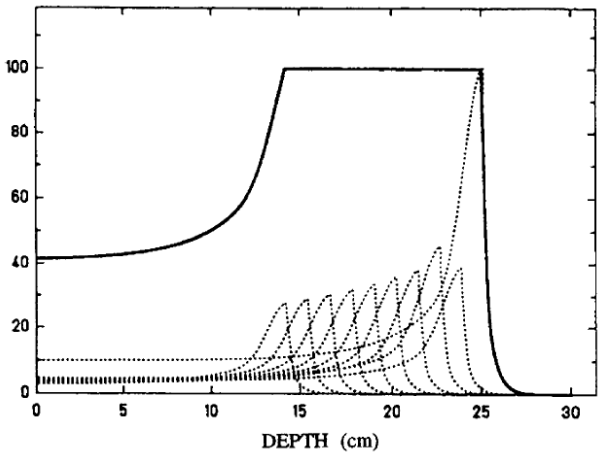

Figure 2 – Superposition of Ten Bragg Peaks forming a Spread Out Bragg Peak (SOBP) [9]

As shown in Figure 2, the total radiation exhibited by the protons is called the spread out Bragg peak (SOBP). It can be seen that at low depths the dose is much smaller, meaning lower doses are received in surrounding tissues.

For X-ray photons, the total dose is much higher than that of protons before and after the cancerous region occurs. This is shown in Figure 3 and means that a higher amount of radiation is exposed to the surrounding healthy tissue.

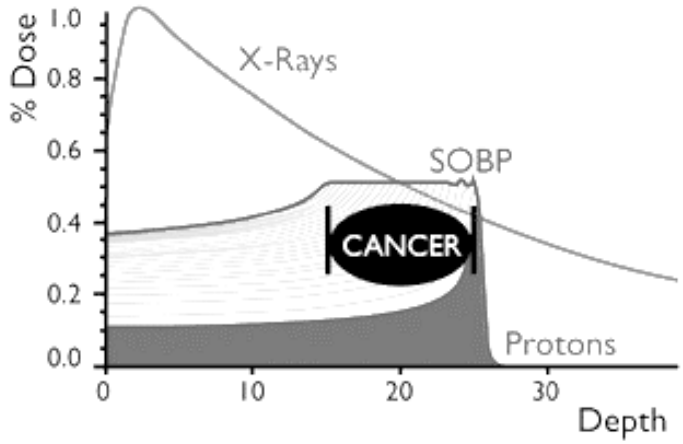

Figure 3 – Dose-Depth Characteristics of X-ray Photons Compared to Protons [10]

This concept is also displayed in Figure 4. It is clear that X-ray photons have a much more detrimental effect on the surrounding tissue and that a more localised form of treatment is possible using protons.

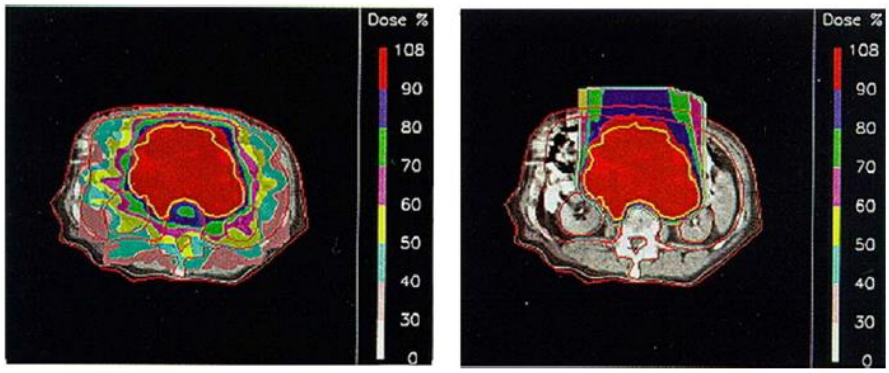

Figure 4 – Comparison of Dose Localisation

***LEFT**: X-ray Photons* ***RIGHT:** Protons*

5 RF Cavities

Following on from the basics of proton RF linear accelerators, the accelerating structures within the linacs, known as cavities, need to be investigated as they are the main concern of this project. Cavities, as mentioned before, are areas of empty space designed to transfer electromagnetic energy to the particles to be accelerated. The process by which energy is transferred to a beam of charged particles is as follows: a resonant field grows in each cavity transforming the low level fields which propagated through the waveguide, into high level fields in the cavity itself; in order to accelerate the particles, the electric field must be aligned with the path of the beam [3].

5.1 Parameters Used for RF Cavity Analysis

When designing RF cavities there are a multitude of parameters used in order to decide upon the best physical attributes for a defined task. These parameters are often phrased 'figures of merit' and the most important of these is generally regarded to be a factor known as the shunt impedance [4].

The shunt impedance (R_S) describes the resistance of the cavity [5]. Using Ohm's law, resistance is equal to the voltage squared divided by the resistance. If this equation is rearranged for resistance, it defines the RF cavity's efficiency in converting RF power into voltage across a gap. This efficiency is the ratio of useful work observed to the input energy required. The useful work is represented by the voltage to

the beam, squared in order to take account of cavity dimensions, as this parameter is proportional to the energy gain of the particle and the energy required is the power input [3], [4]:

$$R_S = \frac{V_0^2}{P} \tag{1}$$

Where: V_0 = Peak RF Voltage Across the Gap / V

P = RF Power Dissipated to the Cavity Walls / W

When investigating the effective voltage seen by the particle, the velocity can be represented as βc. This is because beta (β) is equal to the velocity of the particle (v) divided by the speed of light (c) and if this is rearranged for velocity, the result is βc [4]. In the case of effective voltage an effective shunt impedance (R) can be defined. This value represents the cavity's effectiveness of delivering energy to a charged particle per unit power loss [3]:

$$R = R_S T^2 = \frac{(V_0 T)^2}{P} \tag{2}$$

Where: T = Transit Time Factor of the Particle across the Gap

ϕ = 0

(Where ϕ is the synchronous phase)

$\Delta W_{\phi=0} = qV_0T$

(Where $\Delta W_{\phi=0}$ is the change in work at zero synchronous phase)

Both of the parameters described above, the shunt impedance and the effective shunt impedance, are often described per unit length. The shunt impedance per unit length (Z) is denoted:

$$Z = \frac{R_S}{l} = \frac{V_0^{\,2}}{Pl} \tag{3}$$

From Equation (1) and (2), it is clear that the effective shunt impedance is simply the shunt impedance multiplied by the square of the transit time factor. Therefore the effective shunt impedance per unit length is simply (ZT^2) and is defined:

$$ZT^2 = \frac{R}{l} = \frac{(V_0 T)^2}{Pl} \tag{4}$$

Where: l = Length / m

Another parameter used for cavity analysis is the quality factor or Q-factor. The quality factor gives the bandwidth of a resonator, in this case the cavity, relative to its center frequency. It is defined:

$$Q_0 = \frac{\omega_0 U}{P} \tag{5}$$

It is clear, from the fundamental principle that power is the rate of doing work, that when there is a quantity of energy being divided by an amount of power it can be represented by a time. For this reason Q_0 can also be expressed [3]:

$$Q_0 = \omega_0 \tau_0 = \frac{\omega_0}{\Delta\omega_0} \tag{6}$$

Where: U = Energy Stored $= \frac{1}{2}\mu_0 \int |H|^2 dV$

ω_0 = Angular Frequency / Hz

$\Delta\omega_0$ = FWHM (Full Width at Half Maximum) Bandwidth

Another way to represent the Q-factor is to consider its definition. It is the number of RF cycles it takes in order for all the energy from the cavity to be dissipated, multiplied by 2π. From this it can be represented as [11], [12]:

$$Q_0 = \frac{2\pi P_{tot}}{\Delta P/cycle} = \omega_{cavity} r_s C \tag{7}$$

Where: C = Capacitance / m

By then taking the ratio of the previously discussed effective shunt impedance (R_s) to the Q-factor (Q_0) a value for r over Q or the geometric shunt impedance is arrived upon. This value, at a specific frequency, gives the efficiency of the acceleration per unit of energy stored:

$$\frac{R}{Q} = \frac{(V_0 T)^2}{\omega U} \tag{8}$$

The value of R/Q is solely a geometrical function and so is independent of the material the cavity is made from and the surface properties that govern the power losses.

Another variable that takes advantage of comparing cavities independent of material and frequency is the geometric constant (G) [11]:

$$G = R_{surface} Q_0 \tag{9}$$

The geometric constant and the R/Q value are parameters which only dependent on the shape of the cavity and so are a useful tool in cavity optimisation [3].

5.2 Accelerating Modes for Cavities

One application of the figures of merit is to eradicate unwanted accelerating modes. In order to analyse the concept of accelerating modes, initially the concept of a pillbox cavity will be used. In this case a cylindrical coordinate system (r, ϕ and z) is adopted. Figure 5 shows the required electric and magnetic field propagation inside a pillbox cavity in order for charged particle acceleration to take place.

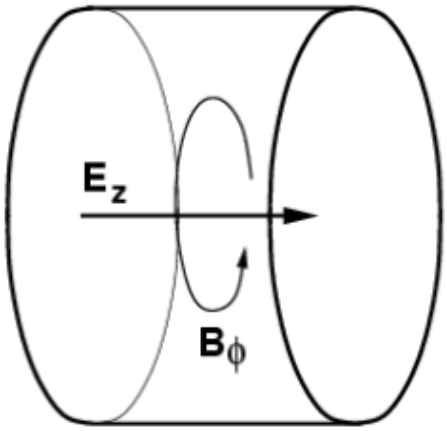

Figure 5 – Electric and Magnetic Field Vectors within a Pillbox Cavity [13]

In this case the only electric field component is E_z and its direction is always perpendicular to the cavity walls. The magnetic field vector, B_ϕ, is not perpendicular to the walls at any point.

For cylindrical coordinate systems, an equation which describes a wave within the cavity is denoted as follows:

$$\frac{\partial^2 E_z}{\partial z^2} + \frac{1}{r}\frac{\partial E_z}{\partial r} + \frac{\partial^2 E_z}{\partial r^2} - \frac{1}{c^2}\frac{\partial^2 E_z}{\partial t^2} = 0 \tag{10}$$

The solutions of this equation are Bessel functions, displayed in Figure 6.

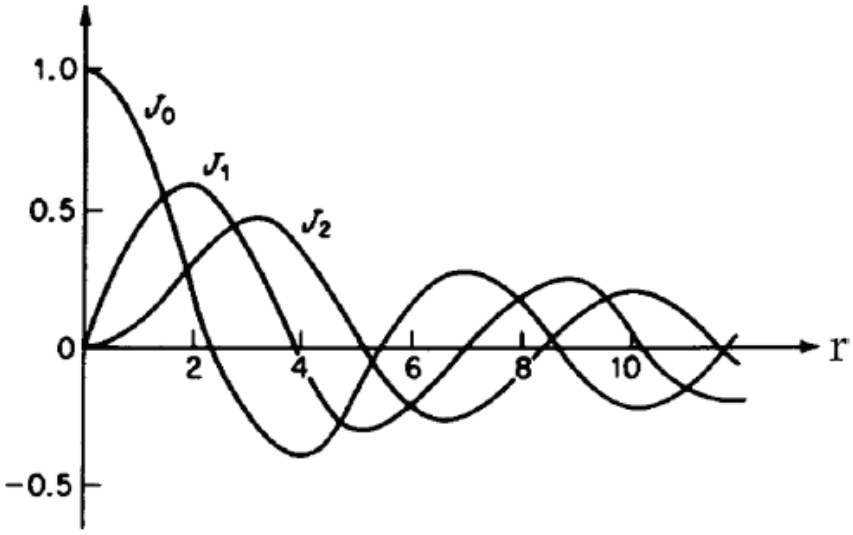

Figure 6 – Low Order Bessel Functions [14]

In order to accelerate charged particles the pillbox cavity uses a transverse magnetic (TM) field where magnetic field components only exist in the transverse direction and an electric field is observed longitudinally which corresponds with the direction of particle propagation. As mentioned previously, this electric field causes the acceleration of the particles [15], [16], [17]. The TM field is denoted TM_{mnp} where:

Table 1 – Transverse Magnetic Field Subscript Descriptions

Subscript	Description
m	The number of full period variations of the field components in the azimuthal direction (about ϕ).
n	The number of zero point crossings of the longitudinal field along the radial direction.
p	The number of half period variations of the field components in the longitudinal direction (the number of nodes on the z-axis) [13], [15].

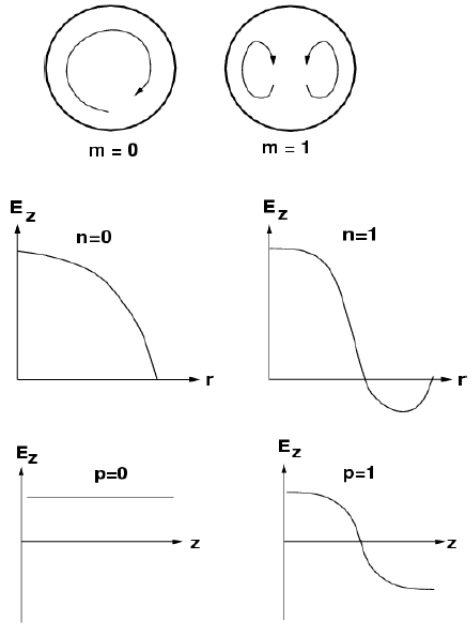

Figure 7 – TM Mode Indices [13]

The values of m and p can exist as integer values including zero whereas the value of n can be any integer value apart from zero. The permutations of m, n and p give rise to different radial and azimuthal solutions with represent an array of varying TM modes. The field components can be represented as sinusoidal expressions [3], [13]:

Electric Field Components:

$$E_r = -\frac{p\pi}{l}\frac{a}{x_{mn}} E_0 J'_m(k_{mn}r)\cos(m\theta)\sin(k_z z)e^{j\omega t} \tag{11}$$

$$E_\theta = -\frac{p\pi}{l}\frac{ma^2}{x^2_{mn}r} E_0 J_m(k_{mn}r)\sin(m\theta)\sin(k_z z)\, e^{j\omega t} \tag{12}$$

$$E_z = E_0 J_m(k_{mn}r)\cos(k_z z)e^{j\omega t} \tag{13}$$

Magnetic Field Components:

$$B_r = -j\omega \frac{ma^2}{x^2{}_{mn} r c^2} E_0 J_m(k_{mn} r) \sin(m\theta) \cos(k_z z)\, e^{j\omega t} \tag{14}$$

$$B_\theta = -j\omega \frac{a}{x_{mn} c^2} E_0 J'_m(k_{mn} r) \cos(m\theta)\, cos(k_z z) e^{j\omega t} \tag{15}$$

$$B_z = 0 \tag{16}$$

Where: $k_z = \frac{\pi p}{l}$

K = The coupling coefficient, Section 5.5.2.2

r = Radius

A = Radius of the Inner Conductor

E_0 = Peak Electric Pield

J_m refers to a Bessel function of order 'm'. The first three of these Bessel functions are clearly displayed in Figure 6. The presence of 'j' in each of the magnetic field components signifies that the fields are in quadrature and thus are 90° out of phase with one another.

The pillbox cavity normally uses the TM_{010} mode for acceleration. This means that the values for m and p are equal to zero and n is equal to one. When substituted into Equations (11) – (45), the following field components are observed [3], [13]:

Electric Field Components:

$$E_r = 0 \tag{17}$$

$$E_\theta = 0 \tag{18}$$

$$E_z = E_0 J_0(k_{01} r) \cos(0) e^{j\omega t} = E_0 J_0(2.045 r) \cos \omega t \tag{19}$$

Magnetic Field Components:

$$B_r = 0 \tag{20}$$

$$B_\theta = -j\omega \frac{a}{x_{01}c^2} E_0 J'_0(k_{01}r)\cos(0)\, cos(0) e^{j\omega t}$$

$$B_\theta = -\frac{E_0}{c} J_1(2.045r)\sin\omega t \tag{21}$$

$$B_z = 0 \tag{22}$$

The resonant frequency of the pillbox cavity can be defined from this. This is an important parameter in cavity design as at resonance an accelerator can be driven much more efficiently. At resonance the radius is set to 'a' and for '$E_z(a) = 0$', '$k_{01}a$' must be equal to the point that the first Bessel function (J_0) crosses the horizontal axis. This value is 2.405 and can be verified by referring to the graph shown in Figure 6.

$$k_{01}a = 2.405 \tag{23}$$

$$k_{01} = \frac{2.405}{a} \tag{24}$$

as: $k_{01} = \frac{\omega}{c}$

$$\frac{\omega}{c} = \frac{2.405}{a} \tag{25}$$

as: $\omega = 2\pi f$

$$f = \frac{2.405c}{2\pi a} \tag{26}$$

If for example, the cavity had a radius of 0.5 meters, a = 0.5, then the resonant frequency of the pillbox cavity would be [13]:

$$f = 230\ MHz\ (3SF) \tag{27}$$

As well as transverse magnetic fields there also exist transverse electric (TE) and transverse electromagnetic (TEM) fields, both of which are also used for particle acceleration. Conversely to TM fields, TE fields have electric components in the transverse direction and the magnetic component propagates longitudinally. TE modes are good for applications at low energies where a high shunt impedance is necessary. They achieve this due to the fact that there are less magnetic fields on the inside surface, meaning system losses are reduced and a higher shunt impedance is achievable.

In a TEM mode structure, the field along the axis consists of electric and magnetic components. TEM mode cavities are used when the frequency is much lower than the frequency used in TE and TM modes, which are both of order 10^8 Hz. At low frequencies, i.e. in the MHz range, the dimensions of the TE and TM assemblies become far too large for realistic manufacture. In order to accelerate charged particles in TEM mode the electric field component is bent on the axis. In terms of frequency tuning, the longitudinal dimensions are now responsible, rather that the transverse ones [15].

5.3 Resonant Frequency of a Pillbox Cavity using Equivalent Circuit Analysis

Referring back to the derivation of the resonant frequency of a pillbox cavity, an alternative method for this, and for many instances of cavity analysis, is to use equivalent circuits [18]. The pillbox cavity can be analysed as a cylinder where the outer surface is a conductor, Figure 8. Due to this an equivalent circuit can be used and the cavity is compared to an electrical circuit containing lumped elements, Figure 8 [13].

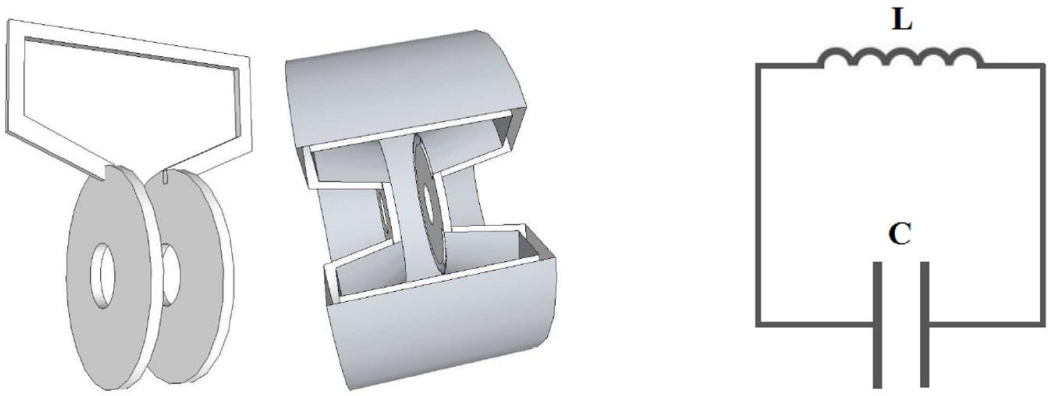

Figure 8 – Pillbox Cavity [13] and its Equivalent Circuit

Using basic ciruit analysis the resonant frequency of the cavity can easily be calculated:

$$\omega_{res} = 2\pi f_{res} = \frac{1}{\sqrt{LC}} \tag{28}$$

Where: ω_{res} = Resoant Angular Frequency / Hz

f_{res} = Resoant Frequency / Hz

L = Inductance / H

C = Capacitance / F

The resistance of the cavity can also be found by using equivalent circuits and this variable can be used to calculate figures of merit such as the Q-factor [11]:

$$Q_0 = \frac{\omega_0 U}{P} = \sqrt{\frac{C}{L}} R \tag{29}$$

Using this method other values such as the geometric shunt impedance can be derived. Equations (28) and (29) and are examples of equations which can be used in order to optimise the cavity and relate directly to the addition of nose cones, which can be seen in Section 5.6.

5.4 Peak Fields

During the cavity design stage, surface electric and magnetic fields are important factors to consider due to the quantity of energy within the cavity being limited by their peak values [3], [11]. In the case of surface electric fields, the peak value must be limited as large values result in electric breakdown. Electric breakdown occurs when the electric field becomes large enough for an insulator, in many cases air in the cavity, to conduct electricity. It can be continuous or discontinuous, but is usually the latter for gases [19]. In order to take account of this, the ratio between the peak surface electric field (E_s) and the average axial field (E_0) is used. This is denoted [3]:

$$\frac{E_s}{E_0} \tag{30}$$

Disregarding the transit time effect, for a pillbox cavity $E_s = E_0$ and therefore this ratio is equivalent to 1.

In order to avoid breakdown, the Kilpatrick limit is used. The limit is represented as a formula which was derived from a multitude of experiments and presents a relationship between several variables that ensures no electrical breakdown will occur [3], [17].

$$f = 1.643 E_K{}^2 e^{\frac{-8.5}{E_K}} \tag{31}$$

Where: f = Frequency / Hz

E_K = Kilpatrick Limit / MVm^{-1}

Equation (31) is plotted as a graph in Figure 9.

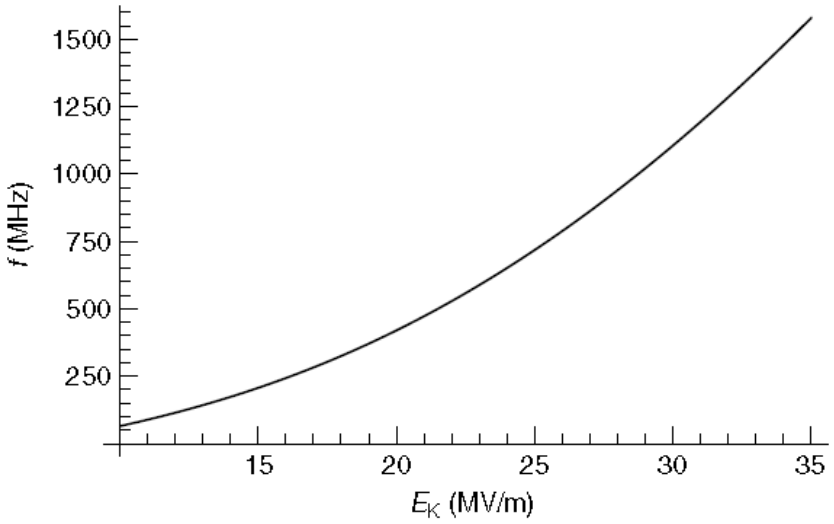

Figure 9 – Graphical Representation of Equation (41) – The Kilpatrick Formula [3]

Moving onto the surface magnetic field, a resistive heating effect is observed which results from currents on the surface created by the magnetic field. This resistive heating can cause structural deformation of the cavity and for this reason the peak magnetic field needs to be restricted. In the case of normal cavities, i.e. none superconducting, this is done using a water cooling system, refer to Figure 1. The result of this means the ratio between the peak surface magnetic field (B_s) and the average axial field (E_0) is also important for analysis [18]:

$$\frac{B_s}{E_0} \tag{32}$$

For a typical pillbox cavity, Equation (31) is equal to 19 $GMV^{-1}m^{-1}$ and this value can increase by 2 or even 3 times the amount for other structures [3].

5.5 Types of Cavities

Thus far the pillbox cavity has been analysed and used as an example in order to illustrate several concepts that surround cavity classification. There is however, an array of different operational cavity types which exist in different types of linacs. In this section, different cavities will be discussed, presenting their advantages and the relevant applications of each.

5.5.1 Drift Tube Linac

Prior to assessing different accelerating structures which utilise cavities, a structure without cavities will firstly be analysed. This structure is termed the drift tube linac (DTL) and it was the first functional linear accelerator, invented by Rolf Wideröe and enhanced by Luis Alvarez.

The DTL structure consists of an array of drift tubes, coupled to one another and each separated by a gap. The concept of coupling is discussed further in Section 5.5.2.2. Each side of each drift tube is connected to opposite polarities of an RF input and as the particle propagates through the system, the polarity of each drift tube reverses in the time it takes the particle to travel the length of a tube. The drift tubes act to protect the particles whist the first half of the polarity change takes place, as this is a reduction in the electric field and hence has a decelerating effect. The acceleration occurs in the second half of the polarity chance when the particle is in the gaps. For this reason a synchronicity must be set up between particle propagation and the period of the RF input [4], [15].

The system uses electrodes in order to connect to ground and by doing so electrostatic breakdown is not a problem and thus does not limit the amount of energy that the linac can produce. The DTL was the first accelerator in which this was the case and it meant that a multitude of gaps was possible. The number of gaps is multiplied by the supplied RF voltage in order to acquire a value for the energy increase of the system [4], [15]:

$$\Delta E = qNV_{RF} \tag{33}$$

Where: ΔE = Energy Increase / J

q = Charge of the Particle Concerned / C

N = Number of Accelerating Gaps

V_{RF} = RF Voltage Input / V

As displayed in Figure 10, when operating at a specific frequency, the DTL's drift tubes must increase in length as the particle travels further along the accelerator. By doing this, the time the charged particle spends in the drift tubes is the same in each case as both the particle velocity and the length of the tube increase. The length of each drift tube is defined by the distance necessary between the centres of the accelerating gaps. As the DTL uses a TEM mode, the length of each accelerating structure must have a length equal to one quarter of the wave:

$$l_n = \frac{v}{2f} = \frac{\beta\lambda}{2} \tag{34}$$

Where: l_n = Distance between the Centre of each Accelerating Gap / m

v = Velocity of the Charged Particle / ms^{-1}

f = Operating Frequency of the System / Hz

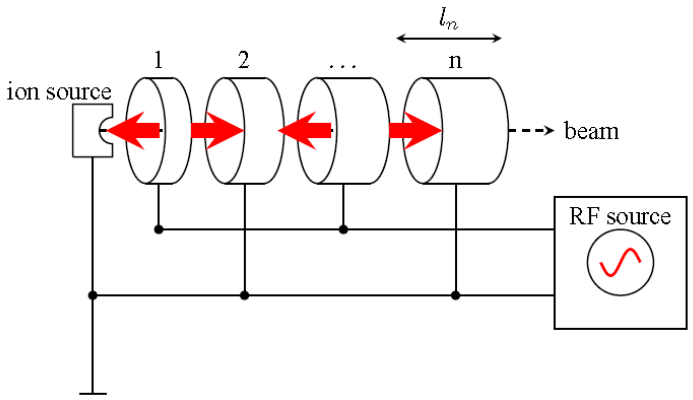

Figure 10 – Basic Design and Operation of a DTL [15]

Although an accurate value for the length of each drift tube can be defined, a limitation exists due to the fact that in order to accelerate faster, longer tubes are needed. The energy is restricted by the fact that some lengths of drift tube are simply unfeasible. Another constraint on the available energy is the fact that at high frequencies, the drift tubes act as antennas due to the vast amount of RF power present. This effect means that the efficiency of the system is compromised and thus frequencies greater than 10 MHz are generally not used.

In order to eliminate the antenna effect, the entire structure can be encased in a large cylindrical container. This method was utilised by Alvarez. Complications do arise from this however, the resonant frequency of each gap must be the same and this now depends on the radius of the drift tubes and the large cylindrical case as well as the distance between the drift tubes [15].

In the DTL, at every point the field travels in the same direction. This means that the mode of propagation is referred to as 0-mode and consequently the DTL is a '0-mode structure'. In this mode the RF phase fluctuates by 2π from gap to gap [4].

An application of drift tube linacs is in the initial stages of acceleration in a proton linac. This is because, for specified values of β, the lengths of the drift tubes can be altered. Using quadrupoles to focus the proton is also possible at this stage when using a DTL [4].

A graph showing proton energies against gap length can be seen in Figure 11. The graph reinforces the fact that, at higher energies, the length of the system becomes unfeasible.

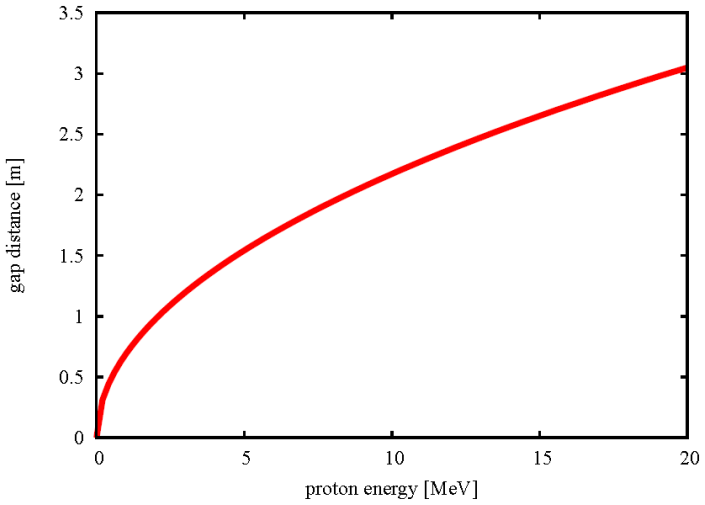

Figure 11 – Gap Distances in a DTL for Varying Proton Energies [15]

The CERN Linac4 is an example of a DTL in use today. The DTL is 19m long can use its 120 cells to accelerate H^- particles from $\beta = 0.08$ to $\beta = 0.31$ with the energy changing from 3 – 5 MeV. The length of each drift tube increases by a factor of 3.9 each time [4].

5.5.2 Standing Wave Cavities

Moving onto the analysis of different cavities, firstly a selection of standing wave cavities will be detailed. To analyse standing wave cavities it is important to firstly understand the standing wave. The superposition of two waves, which are equal in magnitude but opposite in their propagation direction, can create a wave which exists in a fixed position in space. The standing wave appears not to propagate forwards or backwards but simply oscillates around fixed nodes, which occur at half wavelength intervals [20].

When dealing with a waveguide, if it is closed off at the precise points where nodes of the standing wave occur, the reflection of the wave will create a standing wave within the wave guide structure itself. From this principle standing waves can be set up inside cavities [15].

Standing waves in cavities, due to boundary conditions, can only exist at certain frequencies and the finite amount of operational permutations is defined by modes in which the cavity will operate. The frequency of each mode is determined by:

$$\omega_q^{\,2} = \frac{\omega_0^{\,2}}{1 + k\cos\left(\frac{q\pi}{N}\right)} \tag{35}$$

Where: ω_q = Mode Frequency / Hz

ω_0 = Resonant Frequency / Hz

k = Coupling Constant

q = Mode Index (Phase Representative)

N = Maximum Mode Index

Usually k << 1; in this case ω_q can be defined as:

$$\omega_q \approx 1 - \frac{1}{2} k \cos\left(\frac{q\pi}{N}\right) \tag{36}$$

Where: q = 0, 1, 2, … , N

5.5.2.1 Operational Modes

Classifying the modes is done by using the fraction inside the cosine shown in Equations (42) and (43):

$$\varnothing_q = \frac{q\pi}{N} \tag{37}$$

When q = 0, $\phi_q = 0$ and hence the 0-mode will be observed. When q = N, the cavities will operate in π-mode. These modes represent the operational limits for all standing wave cavities and can be seen in Figure 12, the Brioullin diagram.

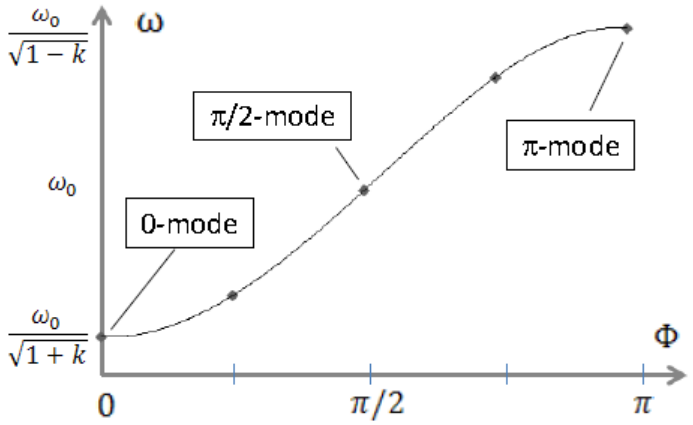

Figure 12 - Brioullin Diagram Showing how the Frequency Varies with the Phase

The diagram represents a structure consisting of 5 coupled cells and if the amount of cells were increased, more modes would exist on the graph. The standing wave amplitude is dependent on the cell concerned.

It is possible to decide on which mode is the most efficient for acceleration. The following equation is used to do this:

$$E_{i(q)} = E_0 \cos(\varnothing_q i) \cos(\omega_q t) \tag{38}$$

Using Trigonometric Identities:

$$E_{i(q)} = \frac{E_0}{2} \left[\cos(\omega_q t - \varnothing_q i) + \cos(\omega_q t + \varnothing_q i)\right] \tag{39}$$

The part of Equation (47) that exits in the brackets of the first cosine, determines whether maximum acceleration will occur. For this to happen it must be equal to 0 in order for ω_{qt} to equal ϕ_qi. When this criterion is met, the second cosine determines which accelerating modes can be used [4].

5.5.2.2 Coupling

The previous section mentioned coupling between cavities and before different types of cavity are explored, it is important to understand this concept.

Cavity coupling simply means that a proportion of the field from one structure propagates into the next one. Firstly, it needs to be determined what type of field will be moving from cavity to cavity, i.e. electric or magnetic. Once this is defined it is clear whether there will be electric or magnetic coupling.

The presence of both types of coupling are down to cavity design. Magnetic coupling is achieved by having a hole on the outer surface of the cavity and electric coupling is achieved simply by enlarging the orifice through which the charged particles travel until there is enough room for some of the electric field to dissipate into the though [4].

In Section 5.3, equivalent circuits were used to determine the resonant frequency of a pillbox cavity. Equivalent circuits can also be used in order to evaluate the coupling in an array of cavities and this is displayed in Figure 13.

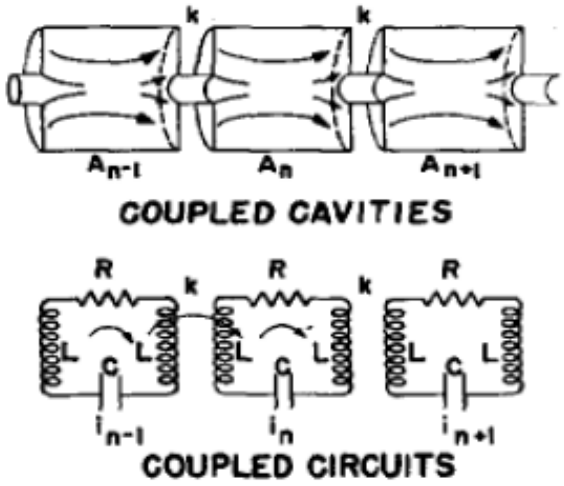

Figure 13 – Analysing Coupled Cavities using Equivalent Circuit

Each cavity is represented by an individual RLC circuit which can be analysed using conventional rules of circuit analysis. The inductance is split in order to allow the idea of mutual inductance to be used. Mutual inductance occurs when there are two coils of wire in close proximity to one another. A magnetic flux density in one, originating from moving charge in electrical circuits, induces a magnetic flux linkage in both the first and second coil. This concept is directly translatable to the operation of coupled cavities [21].

The concept of coupling leads to coupled cavity linacs (CCLs). These linacs house several accelerating cavities which are each followed by a coupling cell or cells. Unlike the DTL, the velocity variation between cavities is much smaller meaning that coupled cavity linacs are used at high energies and the cavities are set to be the same length. When the required energy of a linac system to be designed is low, a DTL is used and when the specified energy is increased above a certain threshold value, a CCL is generally implemented instead.

A CCL has fuel cells on each end cavity of the accelerating section and these, unlike the other cavities, only need coupling in one direction. In addition to this, the array of cavities as a unit, known as a tank, can also be coupled to another array of cavities using a bridge coupler.

5.5.2.3 Side Coupled Structure

The applications of standing wave structures with coupled cavities give rise to several cavity designs that utilise both of these concepts. Three cavity designs will be evaluated, the first of which is known as the side coupled structure (SCS) and shown in Figure 14.

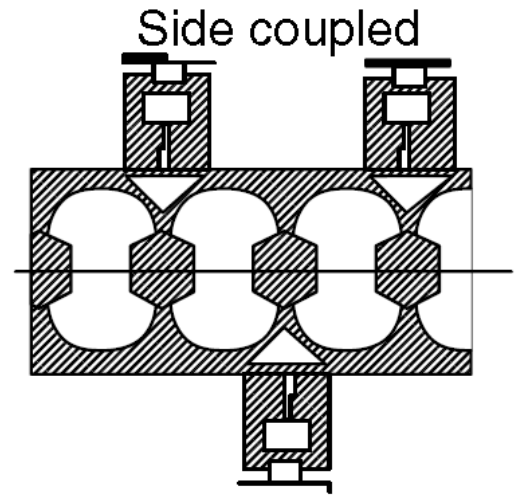

Figure 14 – Side Coupled Structure [3]

The SCS is a magnetically coupled structure that operates in π/2-mode where the coupled cells do not lie on the beam axis. Due to its mode of operation there is no field in the coupling cells. The π/2-mode stabilises the accelerating field for the system as a whole but, due to the independence of the coupled cells, π-mode operation is observed on the beam axis itself ensuring maximum acceleration [4], .

Side coupled linacs (SCLs) usually operate with very high energy and frequency. Power to the cavities is provided by klystrons, the device responsible for providing the RF power, which is why the structure must operate in the π/2-mode as their sensitivity means 0 or π-mode is unachievable [4].

A 3 dimensional representation of an SCS is displayed in Figure 14.

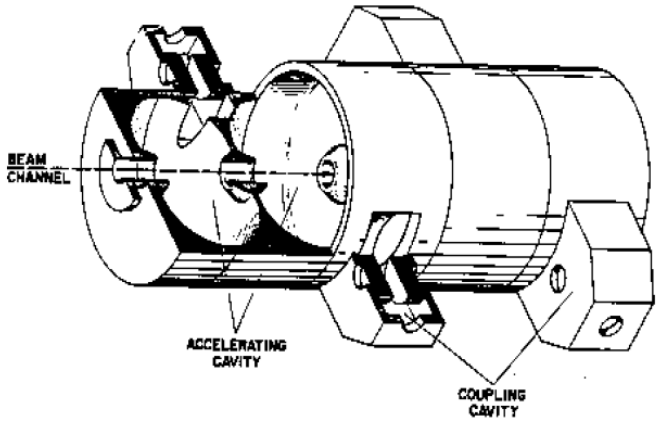

Figure 15 – 3-Dimensional Representation of a Side Coupled Structure [4]

An example of a side coupled structure for accelerating protons is the Linac Booster (LIBO) structure. This linac is detailed in Section 5.7.

5.5.2.4 Annular Coupled Structure

Similarly to the SCS, the annular coupled structure (ACS) also operates in π/2-mode. Linacs that use annular coupled structures include several accelerating cavities which are each followed by an annular coupling cell. This arrangement is shown in Figure 16.

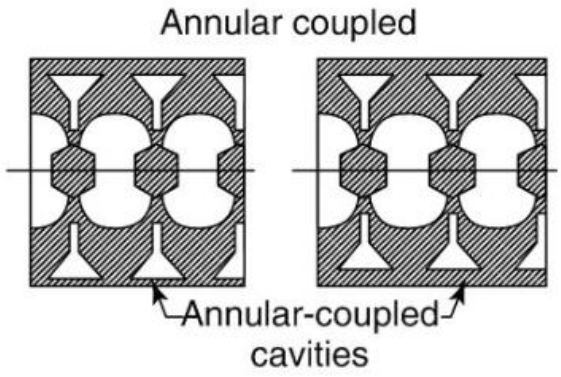

Figure 16 – Annular Coupled Structure [3]

Side coupled structures generally have a higher shunt impedance, Section 5.1, than annular coupled structures by around 5%. This makes using an ACS seem disadvantageous. However the location of the coupling slots in side coupled structures can incur dipole addition which can mean slight distortion of

the transverse magnetic field away from the beam axis. The result of this is a transverse field component at the beam axis which has a negative effect on the quality of the charged particle beam over time.

For this reason the ACS is used in applications where maximum beam quality throughout the acceleration is necessary. When implementing the ACS however, there are operational problems that need to be overcome [22], [23].

Annular coupled structures use the TM_{010} accelerating mode in order to accelerate the charged particle beam. However, in the annular coupling cells, there exist higher order modes (HOMs) such as TM_{110} and TM_{201}. Due to the close proximity between the accelerating field and the field in the annular coupling cell, mode mixing can occur leading to breakdown of the axial symmetry.

For this reason the Japanese Hadron Project (JHP) investigated the ACS in order to eliminate mode mixing. The number of coupling slots, Figure 17, was firstly set to two. Uniform slot orientation meant that the modes in the accelerating cavities (TM_{010}) and the annular coupled cells (TM_{110}) existed closer together as the coupling coefficient increased until the modes entered the same cavity and mixed. In the case of an offset slot orientation, a TM_{210} accelerating mode is observed in the annular coupled cell which decreases the shunt impedance. These problems exist due to a change in axial symmetry that occurs in two slot annular coupled structures and in order to eradicate this symmetry, the number of slots can be increased or the size of each slot must be decreased [22].

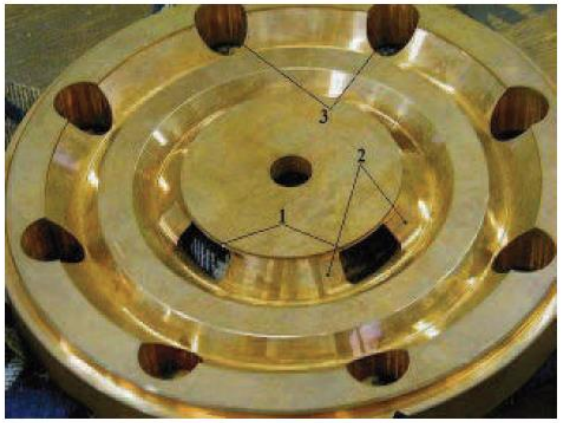

Figure 17 – JPS Annular Coupled Structure (ACS) [23]

1. *The Coupling Slots*
2. *Tapering*
3. *Vacuum Ports*

By increasing the number of slots to four, the required axial symmetry is observed and hence the decoupling of the two modes TM_{010} and TM_{110}. An eight slot system was also explored but there were no significant results that suggested this was advantageous when comparing it to a four slot system [22], [23].

A relevant application of the ACS is the Japanese Proton Accelerator Research project (J-PARC) linac. The purpose of the 400 MeV linear accelerator at this complex is to accelerate protons for research purposes.

5.5.2.5 On-Axis Coupled Structure and Bi-Periodic Chains

Similarly to the 2 previous coupled cavities discussed, the on-axis coupled structure (OCS) operates in $\pi/2$-mode and magnetic cell coupling is observed. Like the SCS and the ACS, the OCS consists of accelerating cavities which have coupling cells in-between. In the case of the OCS however, these coupling cells exist on the beam axis itself [24], Figure 18.

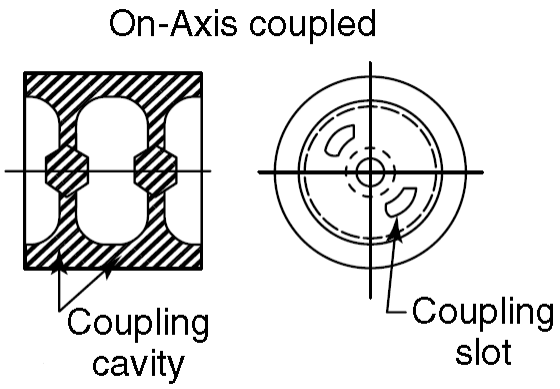

Figure 18 – On-Axis Coupled Structure [3]

One reason an OCS may be chosen is due its small diameter. This means that its overall size and weight are, especially when compared to the SCS, much smaller. Another advantage is that, due to the OCS's simplistic design and cross sectional symmetry, manufacture is much simpler than that of other coupled cavity structures [24], [25].

Without cooling structures in place, the OCS also has a high coupling coefficient (K_c). It is possible to change the value of this constant by altering the orientation of the coupling slots. To increase the value of K_c the mutual influence of the coupling slots on one another needs to be lost. In order to do this the orientation of the slots are altered by a right angle inside the webs of the coupling cells. This idea gives two variations; slot-to-slot and rotated. The new rotated state of the coupling slots can give a value of K_c as much as 2.5 times as large as in the initial position. In normal operation however slot-to-slot orientation is usually chosen as this does not cause quadrupole distortion.

For the on-axis coupled structure, it is often advantageous to use what is known as a bi-periodic chain rather than the periodic layout that has been described thus far. The reason for this is that a bi-periodic structure allows a higher shunt impedance when operating in $\pi/2$-mode. To operate using a bi-periodic chain, the coupling cells are designed in order to take up a lesser amount of axial space and their resonant frequency is made to match that of the accelerating cavities. A typical periodic and bi-periodic structure for the case of an OCS is displayed in Figure 19 [3].

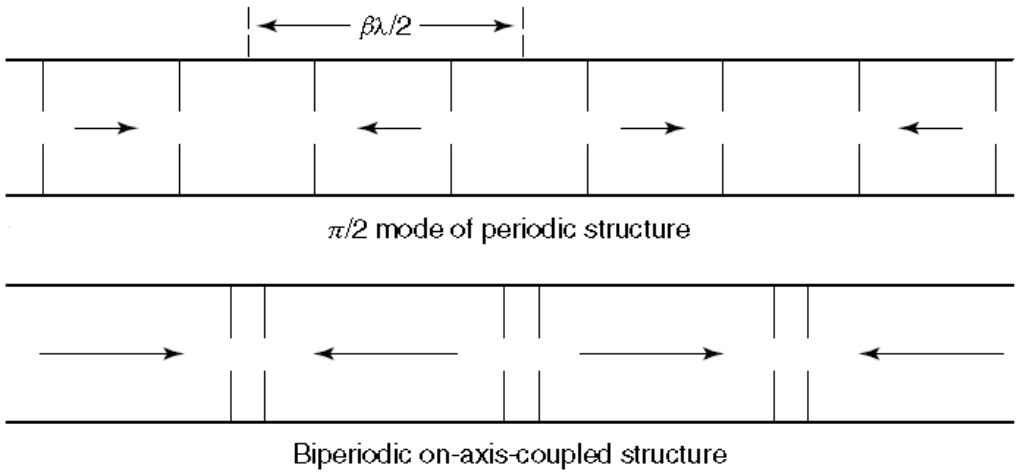

Figure 19 – Available Modes for the On-Axis Coupled Structure [3]

5.5.3 Traveling Wave Cavities

Similarly to Section 5.5.2, travelling wave cavities can only be detailed once the concept of a travelling wave has been investigated.

Travelling wave accelerating structures are similar to that of standing wave apart from the properties at the boundary. In order to achieve a travelling wave structure, an impedance matched boundary ensures no reflections and, as a result of this, the wave equation contains no solutions which represent a standing wave.

Although travelling wave structures exhibit larger losses than standing wave ones, an application for travelling wave cavities is for when a quick fill time is necessary [26].

5.5.3.1 Spoke Cavity

An example of a travelling wave structure is the spoke cavity. An accelerating structure that uses spoke cavities consists of an array of half-wave TEM cells. Each cell has a conductor, called a spoke, residing within it and the orientation of this conductor is changed by 90° from cavity to cavity [15], [18].

Compared with other cavities discussed, the spoke cavity has smaller dimensions and, due to the presence of the spokes, a robust structure. The structure also demonstrates high geometric shunt impedances [27].

Spoke cavities are similar in design to H-mode cavities [15]. The difference being that, for a H-mode structure, the inner conductors are much thinner and the H-mode of operation is determined by the radius of the cavity. In a spoke cavity, it is the spokes themselves that determine field parameters. Another difference between these two cavities is that, for H-mode structures the end cells have to be a specific shape to ensure that the intended mode is used. However, the end cells in spoke cavities can be altered in shape whilst keeping the desired field, meaning geometrical changes can be applied which optimise operational characteristics. In the case of the spoke cavity, the addition and modification of nose cones allows improvement of the transit time factor (T) [15]. A simulated image of a spoke cavity, from CST Microwave Studio, is displayed in Figure 20.

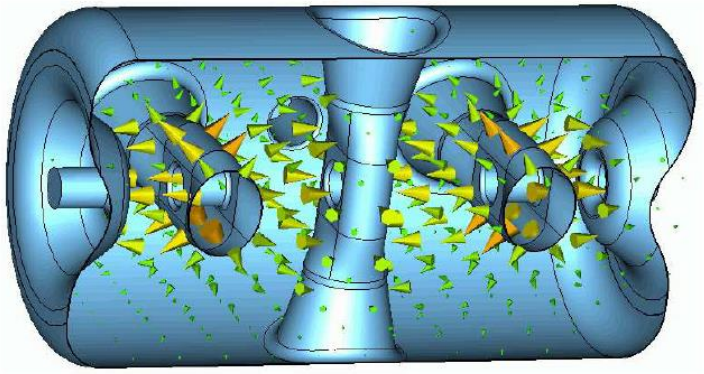

Figure 20 – Spoke Cavity

Project-X, developed by Fermilab, includes a 3 GeV proton linac which uses several single spoke cavities. Although this application is an example of a superconducting linac, which are not of interest during this project, it displays the existing relationship between proton acceleration and spoke cavities [28].

5.6 Optimisation of Standing Wave Linacs

The first and longest section of this project will consist of virtually designing an RF cavity to meet a given specification. In this stage an iterative approach to optimisation will be carried out in order to meet certain criterion.

Several methods and alterations can be applied to cavity structures to change their parameters in order to achieve required operational characteristics. Firstly, as detailed in Section 5.1, the figure of merit known as the shunt impedance needs to be as high as possible. Operational requirements must be known in order to achieve this. A graph of shunt impedance per unit length against energy for different accelerators is displayed in Figure 21.

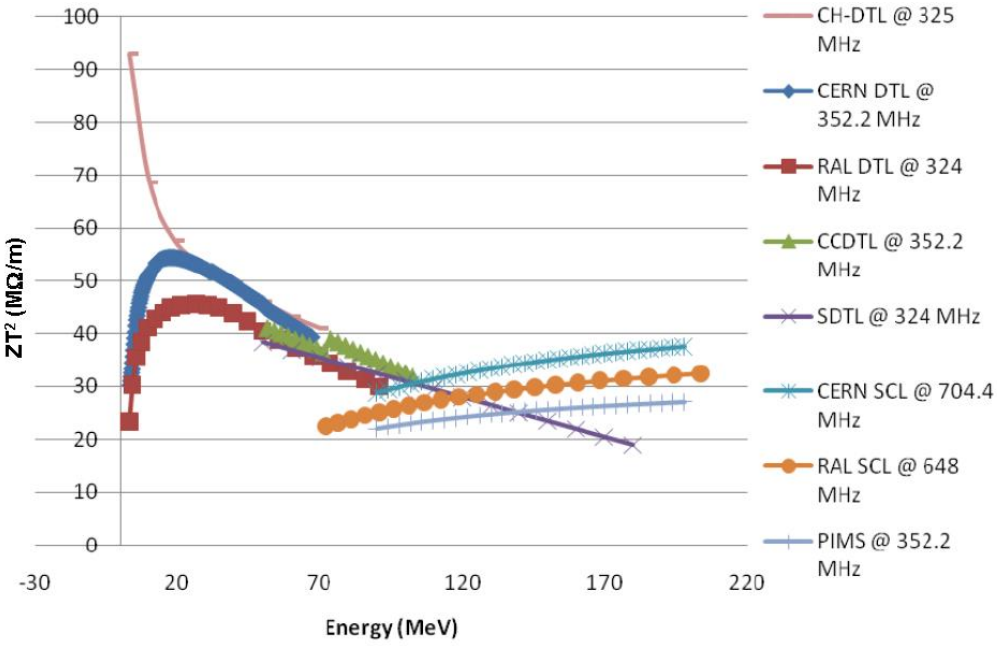

Figure 21 – Shunt Impedance per Unit Length against Energy for Different Reactors [1]

It is clear from Figure 21 that, for structures which operate in 0-mode, the peak shunt impedances exist at beam energies of 20-30 MeV. The π-mode structures start from lower shunt impedances, when compared to 0-mode, which increase with beam energy. These relationships are one factor that allow an educated choice to be made towards the initial design concept of a cavity [1].

Many geometric alterations allow cavity parameters and operational characteristics to be optimised in order to meet specifications. One such alteration is the addition of nose cones to the structure, Figure 22.

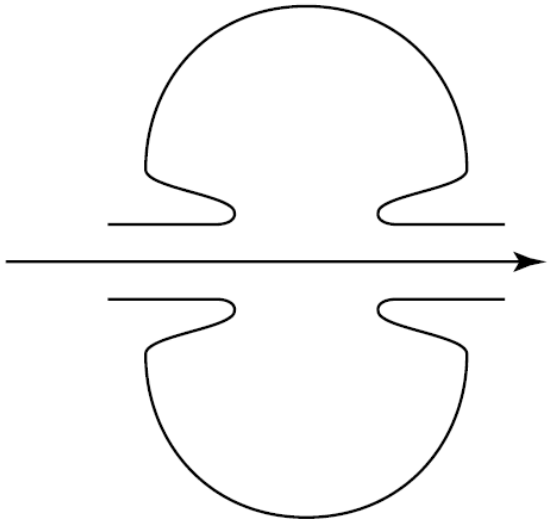

Figure 22 – Schematic Representing the Addition of Nose Cones to a Spherical Cavity [3]

The nose cones act to decrease the gap inside the cavity. Decreasing the gap brings the two conducting walls closer together which, in turn, increases the transit time factor for an area where the axial field is more concentrated than it was before.

Although these resultant effects of the nose cones seem advantageous, there are times when the gap size can reduce too much. At a given electric field that exists at the surface the gain in voltage from the smaller gap can be too large. Furthermore, there can be an increase in the ratio of current at the wall to axial voltage.

During the design stage it is often seen productive to incorporate an ordered optimisation schedule. Table 2 describes a common order of procedures and their results on cavity performance.

Table 2 - Modifications and their Resultant Effects on Various Parameters [3]

#	Geometric Modification	Optimisations from the Alterations
1	Gap Size (Nose Cones)	Maximum geometric shunt impedance
2	Gap Size (Nose Cones)	Maximum energy gain per amount of stored energy
3	Outer Walls	Maximum quality factor value
4	Outer Walls	Maximum spread of power per amount of energy stored

Other key factors to consider during optimisation are aperture radius and the presence of lumped elements attached to the cavity itself. The aperture radius is responsible for changing the beam dynamics, however increasing this parameter can lower the axial electric field and once it becomes large enough, the transit time factor will fall. Lumped elements connected to the structures act to increase the amount of localised fields. This means that the fields that existed at the outer edge, near the cavity walls, are lessened and hence the thickness of the walls can be reduced without a substantial change in operational frequency. Decreasing wall frequency can be advantageous as it make the components much simpler to construct [3].

The Project will utilise the software program CST Microwave Studio to design and optimise several cavities. A logical iterative process will enable optimisation of several of the discussed in order to meet an operational specification.

5.7 Linac Booster

In order to design and optimise an RF cavity suitable for accelerating protons, existing structures capable of doing similar tasks should be reviewed. The Linac Booster (LIBO) is as example of an existing structure capable of accelerating protons to the energies necessary for hadron therapy.

When designing the LIBO, the aim was to produce a linac that could boost protons received from a cyclotron to energies of around 200 MeV. This energy value is chosen as 190 MeV is required to accelerate a proton through 25 cm of soft tissue. A linear accelerator was chosen for a variety of distinct advantages [29], [9]:

- They allow progressive building due to their modular structure.
- Injection and extraction of the beam is simple.
- The manufacturing processes used to construct these accelerators are well known.
- Variable output energy is available.
- The linac structure lends itself to active scanning techniques.
- Low emittance of the transverse beam.

For the linac, a 3 GHz structure was proposed as this enables a high accelerating gradient to be achieved over a short physical distance [30], [9].

A prototype was designed by CERN, INFN (Milan and Naples) and TERA. The linac was constructed and tested. The LIBO prototype is a standing wave structure that uses side coupled cavities in order to accelerate protons; it consists of 4 tanks connected to one another using a bridge coupler. The coupling module is closed off with end plates. The centre bridge coupler takes RF into the system via a matched waveguide and the two couplers that exist either side of this one are attached to vacuum ports. In terms of tuning the frequency of the system, tuning rings and rods were placed onto each half cell and screw tuners were attached to the bridge couplers and end cells. In order to tune the LIBO, the frequencies of the couplers had to be adjusted. Figure 23 shows a cross section of the LIBO accelerating structure.

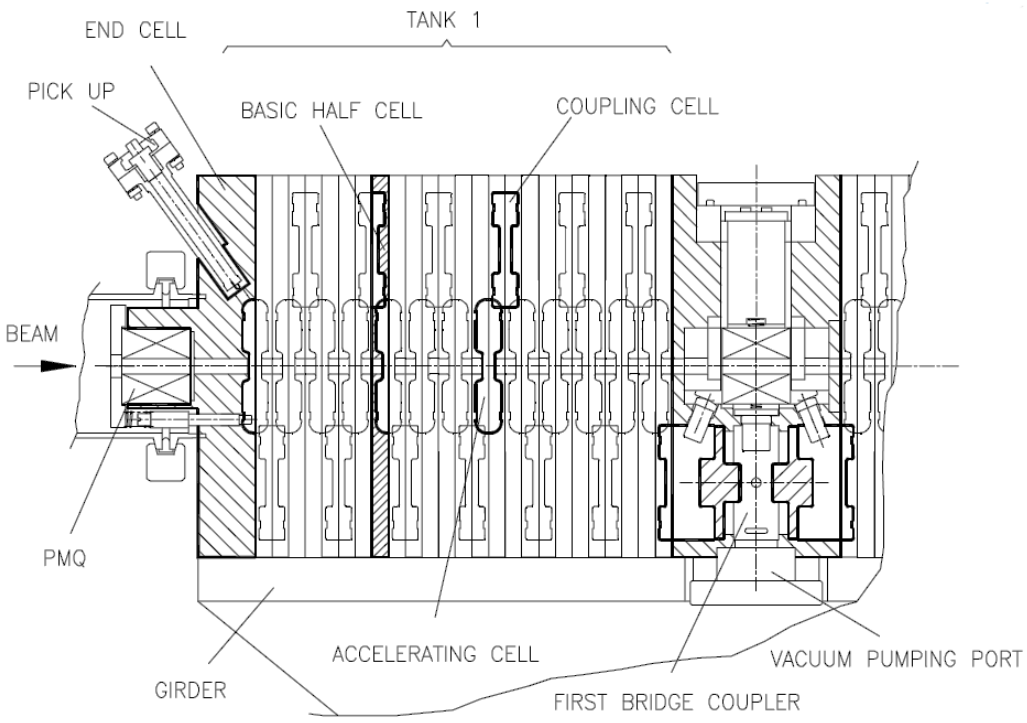

Figure 23 – Section of the LIBO Accelerating Structure [29]

In 2010, full power RF testing occurred at 100 MHz with pulses of 2μs. This achieved the nominal accelerating gradient of 15.8 MVm^{-1} in 72 hours of operation. An RF power of 4.7 MW was used at this gradient. Following this result the pulse lengths were increased to 5μs and after a period of 14 hours the gradient was seen to be 27.5 MVm^{-1} with an RF power of 14.2 MW. The RF limit for the structure was not met at this point but, due to the circuitry, the RF power could not be increased further. Lack of electrical breakdowns and small conditioning times are factors which represent the success of the LIBO [30], [29], [31].

The existing number of cyclotrons in hospitals demonstrates the LIBO's feasibility as it means there are a large number of sites where the application of these structures is possible.

6 Literature Review Conclusion

The concepts, ideas and applications presented in this literature review provide a background to the operation of RF linacs, specifically in the area of accelerating cavities. The research conducted and ideas detailed will now be applied to the design of RF cavities. The information on the operation and optimisation of different cavities provides a strong foundation which will be utilised when implementing the cavities in CST Microwave Studio, allowing the progression to be uninterrupted by basic research.

PROJECT OUTLINE

After researching and building and foundational understanding of RF linac operation, a breakdown of the main tasks necessary to successfully complete the design, build and test stages of this project had to be devised. Although the project plan, Appendix Section 1, enabled a more complex breakdown, it was seen as important to have set of definitive goals to work towards throughout the duration of this project.

Table 3 – Key Stages of the Project

Stage	Description
Implement and Optimise a Structure Using Key Features from an Existing Design.	Implement and optimise the LIBO's side coupled design for the required operational characteristics needed in this project.
Implement and Optimise a New Structure	Design, implement and optimise an annular coupled structure. Use the accelerating cavity designed in the previous stage in order to allow direct comparison of the two types of coupling mechanisms.
Compare the Optimised Structures	Compare the side coupled and annular coupled structures using simulations carried out in CST MWS and calculations using spreadsheet software.
Build	Build the annular coupled structure.
Test	Test the Annular Coupled Structure
Compare Simulated and Tested Results	Compare results gained in CST MWS and the results from the testing of the built structure.

CHAPTER 2 – CAVITY DESIGN

As stated in the project summary, the aim of this project is to produce an RF cavity for a linac which is capable of accelerating protons in order to treat cancer using hadron therapy.

Specifically the cavity will operate using protons from a 24 MeV cyclotron at a resonant frequency of 3 GHz. These conditions have been chosen to assess the operational viability and characteristics of a 24 MeV linac, and specifically to see how different cavity designs at this energy effect operational characteristics.

1 Side Coupled Structure

Before designing the cavity to be built, it was decided that an existing cavity design would firstly be virtually implemented using CST MWS. As referred to in the Literature Review, Section 5.7, the Linac Booster (LIBO) is an existing structure which uses a side coupled cavity arrangement in order to accelerate a proton beam. This design was chosen as it works under similar operating conditions to the specified ones for this project and represents the current state of the art in the field of proton linear accelerators. For this reason it would provide ballpark figures and references to the performance that should be looked for in proton linear accelerators

However, although the LIBO's side coupled designed was to be implemented, the energy of the proton beam would be changed to 24 MeV. This meant that none of the geometries from the original LIBO structure could be used and so the cavity had to be designed from scratch. It was simply the side coupled design that was used as this would act as a suitable point of reference.

1.1 Implementing in CST Microwave Studio – A New Method of Virtual Cavity Design

Rather than an array of cavities, as used in the final linac, a repeating unit that could be rotated and translated to form this array was to be designed. This not only simplified the design, but it also meant

that any simulations would take less time due to the lower amount of virtual meshing and calculations required. The smallest repeatable unit of the side coupled structure, which still enabled simulations to be carried out, was observed as a full accelerating cavity accompanied by two half coupling cells at either side. This, as well labelled accelerating cavities and coupling cells, is shown in Figure 23, page 51.

After conversing with several PhD students and professionals who use CST MWS, it was clear that a new, innovative method of implementing the cavity structures in the software was needed. This was due to the fact that, when virtually analysing the structures, 2 dimensional (2D) lines need to be drawn on the cavity surface, the shapes of which, need to change with the geometry of the cavity. This is because the program is set up to simulate several field quantities on the 2D lines which need to be representative of the location of surface fields. Rather than drawing a line every time the cavity dimensions change, a line which varies with geometrical alterations would allow simpler parametric sweeps of cavity dimensions and the resultant effect on field parameters could be plotted.

In the field, cavity systems are generally drawn as solid objects, e.g. cylinders, and the cavity's geometrical features are applied to this object, using the in-built CAD feature tools in CST MWS. The geometrical features are then parameterised in order to allow the user to alter geometries easily via iterative simulations.

The new method needed to have the cavity parameterised at every point along the surface, in order to allow lines to be drawn later on which change with changes in cavity geometry. For this reason, it was decided that a segment of the cavities cross section was to be designed, in 2 dimensions, and then swept along a perpendicular circular path, in order to form the 3D cavity.

In order to sketch the repeating unit in CST MWS, the side coupled structure's key cross-sectional features, extracted from A. Degiovanni's Thesis [32], were firstly dawn by hand and each length, coordinate and radius labelled accordingly. These labels provided a reference for each parameter, making it clear which value had to be changed later on in the optimisation stage. The sketch was then

re-drawn using the computer program SolidWorks. This provided a clear drawing which would minimise the occurrence of mistakes and allow the new method to be displayed to colleagues; the result of this is displayed in Figure 24 and Figure 25.

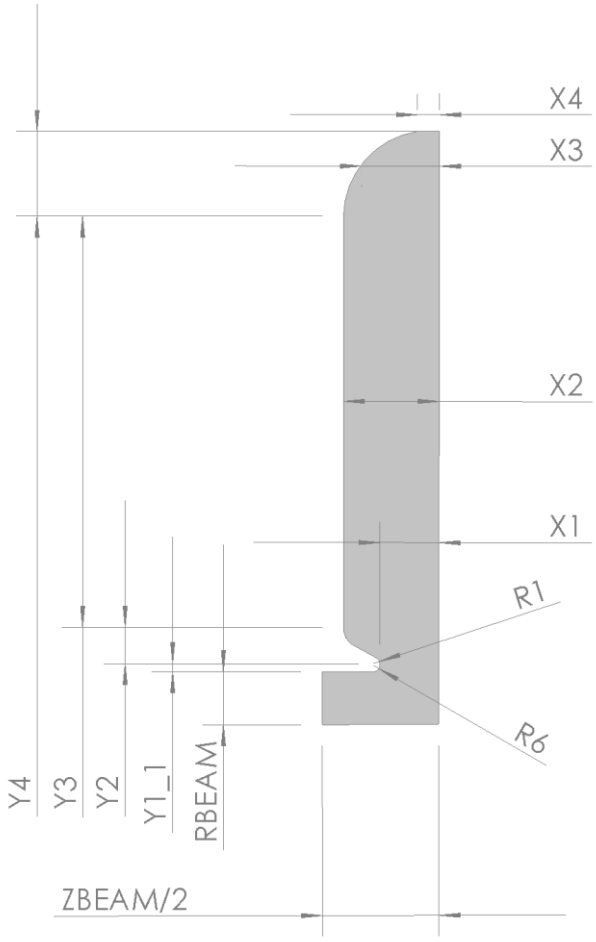

Figure 24 – LIBO Sketch Key Features - Accelerating Cavity

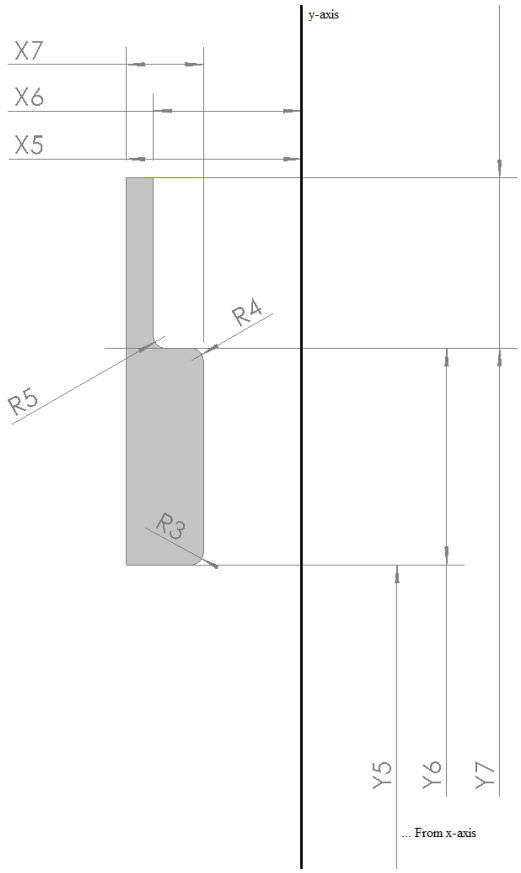

Figure 25 - LIBO Sketch Key Features – Coupling Cell

Following this, the key cross-sectional dimensions were drawn in CST MWS. The sketches were then mirrored in order to produce top-half cross sections of the 2 half coupling cells as well as the accelerating cavity. The design at this point is shown in Figure 26.

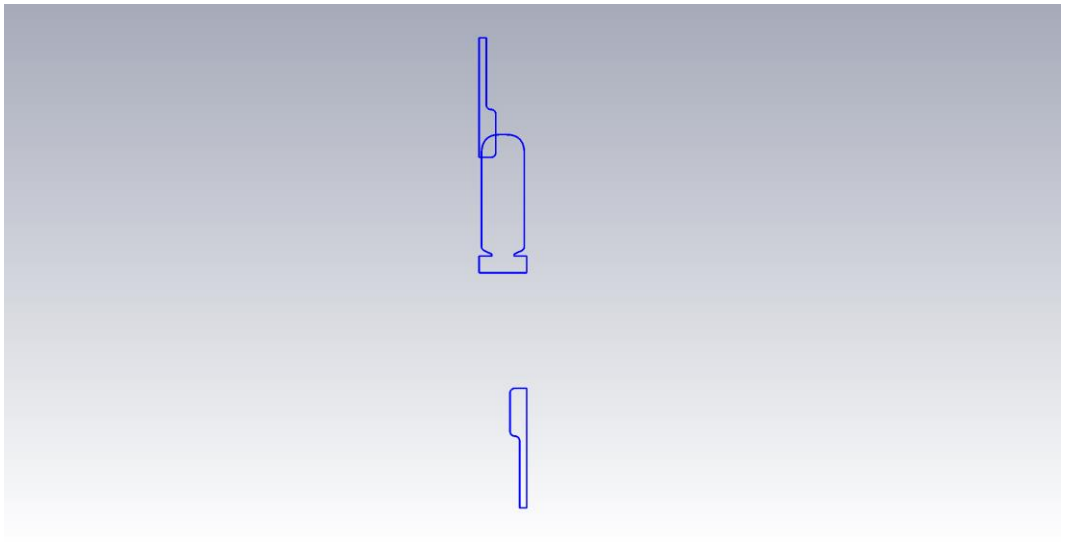

Figure 26 – Initial LIBO Half Cross Sections

After the cross sections had been designed, the two dimensional sketch could be transformed into the three dimensional repeating unit. As discussed, the outlines were swept around circular paths, with the center of each path corresponding with the center of the respective coupling cell or accelerating cavity. The result of the sweeps, and thus the first 3 dimensional side coupled cavity repeating unit, is displayed in Figure 27 as a 3D model and as well as a cross section. The material was set to vacuum and the background to a perfect electrical conductor (PEC) as the cavity is simply the empty space that will be removed a solid block of metal.

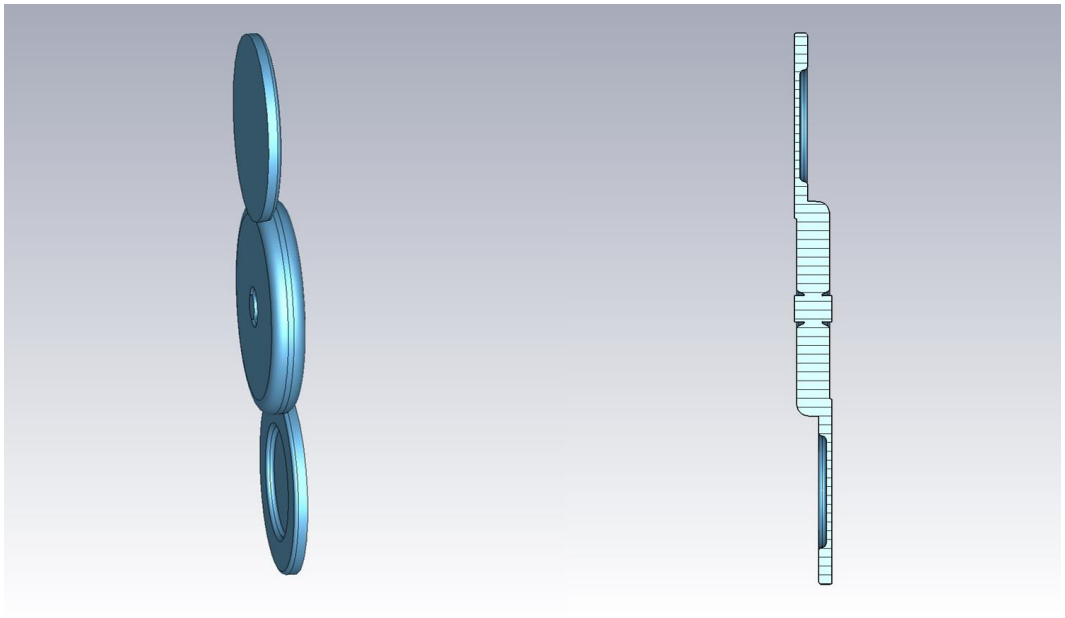

Figure 27 – Initial LIBO Cavity Repeating Unit

***LEFT:** 3D Representation* ***RIGHT:** Cross Section*

The initial parameter values at this stage are shown in Table 4. The parameters were estimated to produce a structure which resembled the LIBO, trying to make the dimensions in proportion to one another.

Table 4 – Initial LIBO Parameters

Parameter	Value
R1	0.3
R2	1
R3	1
R4	1
R5	1
R6	0.15
RBEAM	3.5
X1	4.7/2
X2	4.5
X3	X2
X4	0.75
X5	XCUT
X6	3.5
X7	ZBEAM/2-X5
XCUT	1.5
Y1	RBEAM+Y1_1
Y1_1	0.4
Y2	1
Y3	20
Y4	4
Y5	(Y1+Y2+Y3+Y4)-YCUT
Y6	10
Y7	15
YCUT	4.75
ZBEAM	10

Initially the 2D sketch of the LIBO was done in the XY plane and this is the reason why the values refer these axes. However, it is convention to simulate cavity structures with beam propagation in the Z-direction and for this reason, once the 3D structure had been defined, the whole system was mirrored in order to orientate it in the correct way.

1.1.1 Obtaining the Correct Modes of Operation

In order to get the 24 MeV LIBO to operate at the correct energy, frequency and with the desired performance characteristics, a large array of simulations had to be carried out. These simulations would allow the specifications for the LIBO structure to be met and thus a reference for future designs to be compared to.

Before these simulations, used to optimise the cavity, the correct modes of operation, Section 5.2, had to be identified. This process had to be carried out for both the accelerating cavity and the coupling cells.

In order to find the correct mode for the accelerating cavity the virtual boundary conditions had to be changed. This is because the field of the repeating unit needs to be assessed as if it were operating in the full cavity array. Firstly, the Z plane boundary conditions were set to magnetic. This only accounts for a parallel electric field meaning that the field in the accelerating cavity can be assessed individually. Following this, an Eigen mode simulation was set up in CST MWS for the first 10 modes. This simulation used tetrahedral meshing with an accuracy of 1×10^{-6}. This accuracy was chosen as it was felt that the results would provide a good representation of the characteristics and performance, without making the simulations too time consuming.

Once the simulation was completed, each field was analysed in order to find the correct accelerating mode. The correct mode was found to be mode 1, it was the only monopole mode and it exhibited the desired field which oscillated only in the accelerating cavity with the field's largest magnitude occurring along the beam axis.

The boundaries, in the Z plane, were then switched to electric. Electric field boundaries represent a perfect conductor, meaning that perpendicular electric fields are allowed but parallel ones are not. The same procedure was followed and, again, the ten resultant mode's electric fields were analysed. This time mode 2 was found to be the coupling mode for this structure. The observed fields, for both magnetic and electric boundary conditions, can be seen in Figure 28 and Figure 29 respectively.

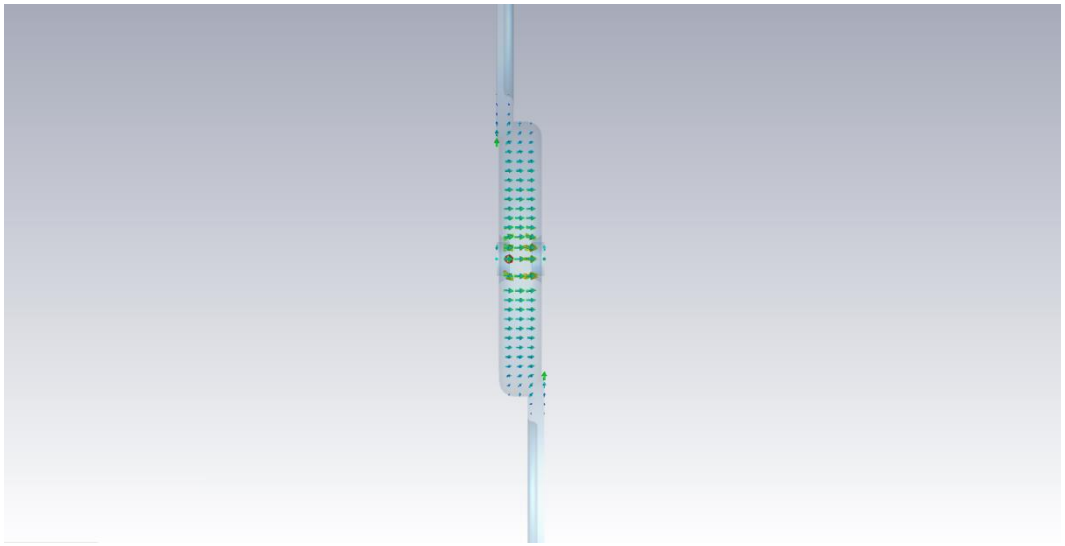

Figure 28 – Initial Field in the Accelerating Cavity (Mode 1 – Magnetic Boundaries)

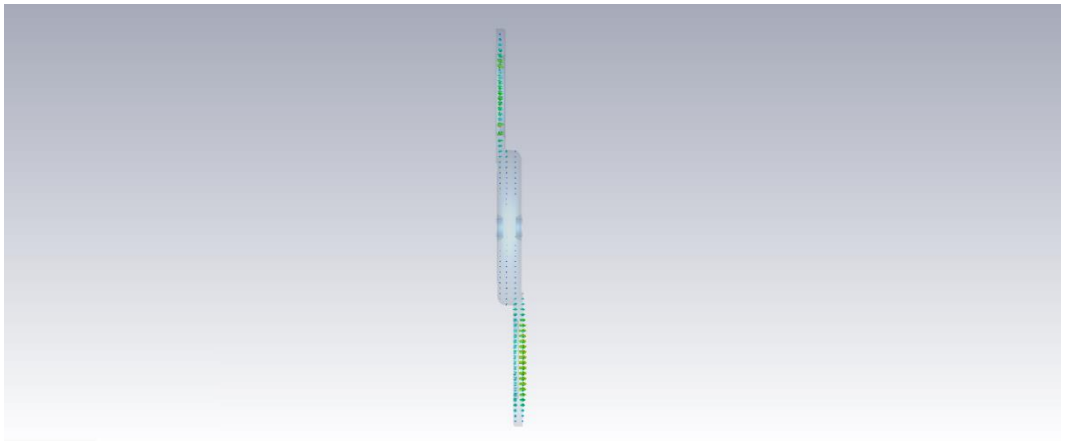

Figure 29 – Initial Field in the Coupling Cells (Mode 2 – Electric Boundaries)

1.1.2 Cavity Length

In order to take account of the proton beam's energy, the length of the cavity, in the Z direction, had to be set to an optimal value. In order to do this, the following equations were utilised [33]:

$$\beta = \frac{v}{c} \tag{40}$$

$$L = \frac{v}{2f} \tag{41}$$

$$\beta = \sqrt{1 - \left(\frac{1}{\left(1 + \frac{E}{E_0}\right)}\right)} \tag{42}$$

Where: β = Beta

v = Speed / ms^{-1}

c = Speed of Light in a Vacuum = 299792458 ms^{-1}

f = Resonant Frequency / Hz

E = Required Proton Energy = 24 MeV

E_0 = Proton Rest Energy = 938.257 MeV (3DP)

Equation (42) resulted in a beta (β) value of 0.2219474084. From this the length of the cavity was calculated as 11.08969319 mm. These two values were parameterised in the software and the value of ZBEAM was changed to the calculated length.

1.1.3 Resonant Frequency

As previously specified, the cavity was to operate at 3 GHz. To optimise the cavity to do this, the following relationship was adhered to:

$$f_{resonant} \propto d^{-1} \tag{43}$$

Where: $f_{resonant}$ = Resonant Frequency / MHz

d = Diameter / m

The process for optimising the frequency needed to be carried out for both the accelerating cavity and the coupling cells. For the accelerating cavity the optimisation process needed to be carried out using the frequency given by mode 1 with magnetic boundaries and mode 2 with electric boundaries was used for the coupling cells, as previously explained in Section 1.1.1.

Having set the boundaries to magnetic, the mode 1 frequency was seen to be much too high. From Equation (40) it is clear that in order to decrease this frequency to 3GHz, the overall diameter of the accelerating cavity had to be increased. Rather than manually changing the radius of the cavity and observing the effect on the frequency, a parameter sweep was set up which changed the radius incrementally, outputting each frequency into a table. From this, the dimension which resulted in a frequency closest to 3 GHz could be selected for use. Table 5 shows the initial parameter sweeps.

Table 5 – Initial Frequency Tuning Using Parameter Sweeps

Sweep 1	
Y3 / mm	$\mathbf{f_1}$ / GHz
20	3.770315475
21	3.656616726
22	3.5495341
23	3.448186849
24	3.35212273
25	3.261339184
26	3.174731464
27	3.092736834
28	3.014646633

Sweep 2	
Y3 / mm	$\mathbf{f_1}$ / GHz
28.1	3.007090724
28.2	2.999513304
28.3	2.992058401
28.4	2.984574261
28.5	2.977150607
28.6	2.969705937
28.7	2.962298623
28.8	2.954928689
28.9	2.94757485

Sweep 3	
Y3 / mm	$\mathbf{f_1}$ / GHz
28.11	3.006423402
28.12	3.005646132
28.13	3.004810502
28.14	3.003977137
28.15	3.00334262
28.16	3.002512148
28.17	3.001805113
28.18	3.001101503
28.19	3.000256809

Sweep 4	
Y3 / mm	$\mathbf{f_1}$ / GHz
28.191	3.000268418
28.192	3.000151867
28.193	3.000091912
28.194	3.000009342
28.195	2.999898819
28.196	2.999887777
28.197	2.999822439
28.198	2.999795325
28.199	2.999684225

It can be seen that initially the change in length of Y3 was fairly large. The gap in which the optimum dimension resided could then be optimised further by using another parameter sweep. This was done iteratively until a value of 3 GHz $\pm$ 1 MHz was reached. 3 GHz to the nearest 1 MHz was arrived at in the second sweep (2.999513304 GHz at Y3 = 28.2 mm). For further accuracy however, sweeps 3 and 4 were conducted which resulted in a frequency of 3.000009342 when Y3 was set to 28.194 mm.

The boundary conditions were changed and this process was repeated for the coupling cells, again resulting in an operational frequency of 3 GHz to the nearest 1 MHz.

1.1.4 Coupling Coefficient

In side coupled structures the field propagates through coupling slots, the size of which are determined by the intersection between the accelerating cavities and coupling cells. This concept is represented by the coupling coefficient (K). The coupling coefficient for the LIBO structure, from published literature [34], [35], is between 4.3 and 4.5%. In order to assess the value of K for the 24 MeV design, the following mathematical analysis had to be used [3]:

$$\omega^2 = \frac{\omega^2{}_{\pi/2}}{1 - K\cos\varnothing} \tag{44}$$

Where: K = Cavity Coupling Constant $= \frac{2L_2}{L_1 + L_2}$

ω = Frequency / Hz

$\omega_{\pi/2}$ = Frequency at a Phase $\frac{\pi}{2}$ / Hz

$\varnothing$ = Phase / Degrees

However, as the coupling constant is much less than 1, 0.043 to 0.045, the fractional bandwidth of the passband can be used in order to define K:

$$\frac{\omega_\pi - \omega_0}{\omega_{\pi/2}} = -K \tag{45}$$

Where: ω_π = Frequency at a Phase π / Hz

ω_0 = Frequency at a Phase 0 / Hz

In order to utilise Equation (45), the boundary conditions were changed to periodic. However, in order to apply periodic boundary conditions, each side of the repeating unit, in the Z plane, had to be the symmetric to one another. To achieve this, the repeating unit was rotated 180^0 around the Z axis, translated by the parameter ZBEAM and added single repeating unit. The result of this transformation was a cavity which had 2 repeating units, Figure 30. It is clear that both boundaries in the Z plane are exactly the same here.

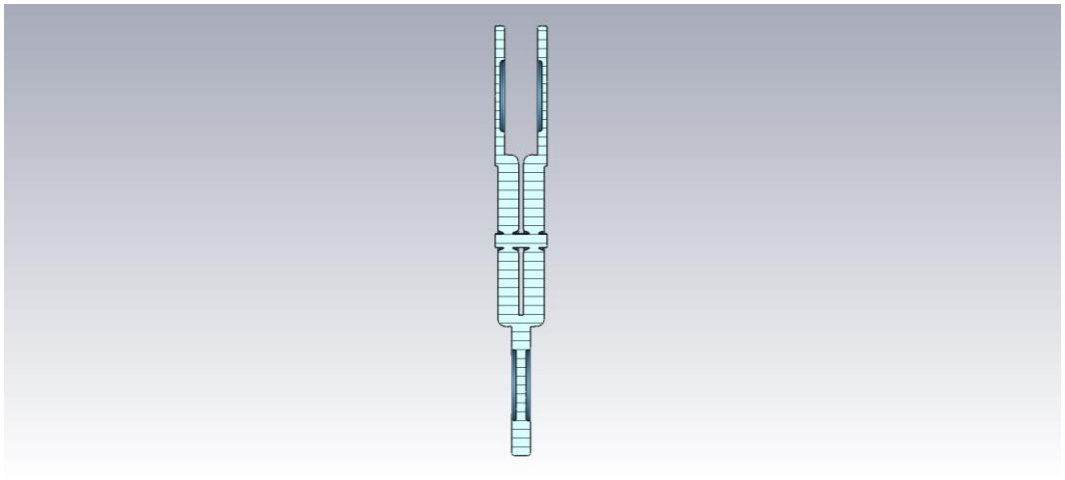

Figure 30 – Transformation of the Repeating Unit for Use with Periodic Boundary Conditions

Following the application of periodic boundaries, the structure was simulated from 0 to 360^0 in steps of 5^0 and post processing techniques were used to output the frequencies of modes 1 to 4 for each phase. The reason the first four modes were used now was because the arrangement now consisted of four whole cavities; two accelerating cavities, one full coupling cell and two half coupling cells.

Once the simulations had finished the data was inputted into a spreadsheet where it was formatted into a graph, Figure 31. In order to get the dispersion curve for the structure, the phases had to be divided by four. This is because the dispersion curve is plotted between 0 and π (0 and 180^0) and each mode represents an equal proportion of the curve. Therefore each mode represents 45^0 and needs to be scaled down from 360^0. Although it may seem like each mode should be divided by eight, as 360^0 divided by 8 equals 45^0, only half of each mode's curve is used. The resultant graph, from the phase scaling, can be seen in Figure 32.

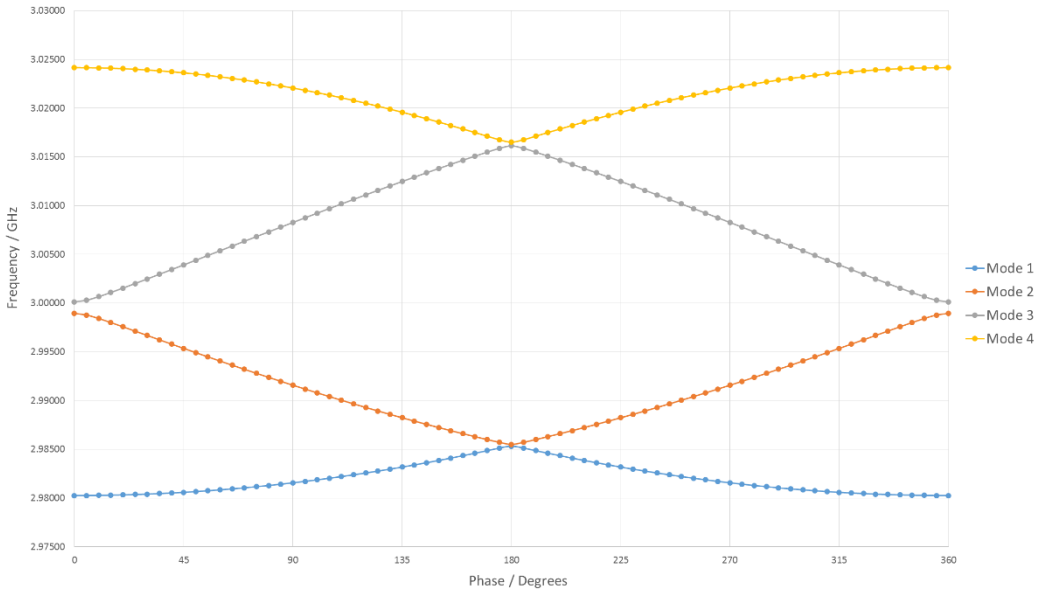

Figure 31 – Simulated Data for the Frequency against Phase for Each Mode Present

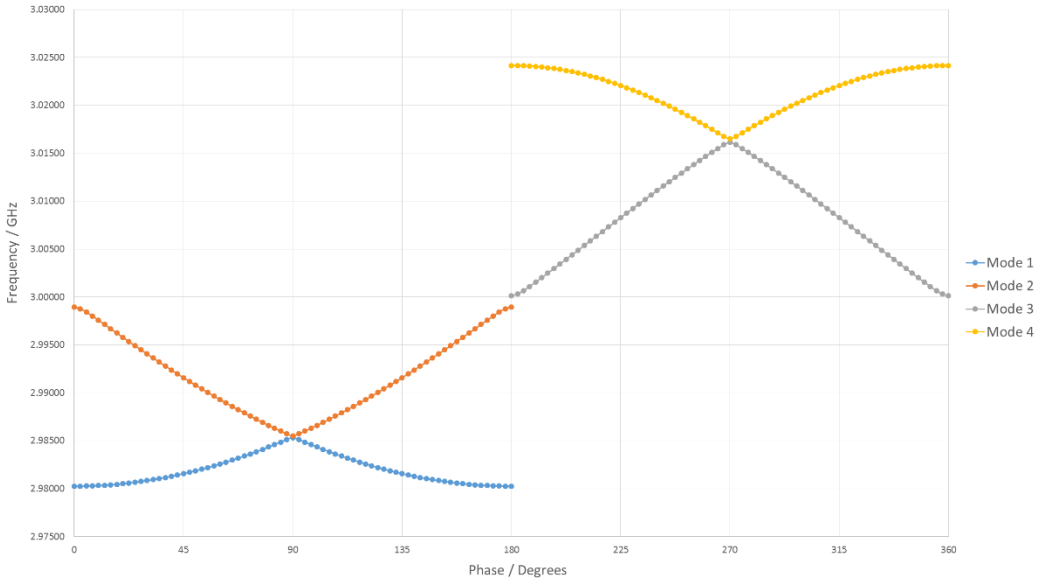

Figure 32 – Scaled Data for the Frequency against Phase for Each Mode Present

Following this, each curve was shifted to its respective quadrant of the dispersion curve. This was done by adding 0^0 to the mode one phases, 45^0 to the mode two phases, 90^0 to the mode three phases and finally, 135^0 to the mode 4 phases. As already discussed only half of each mode's curve was used in the

final graph. Figure 33 displays the resultant dispersion curve for the structure prior to any optimisation of the coupling constant.

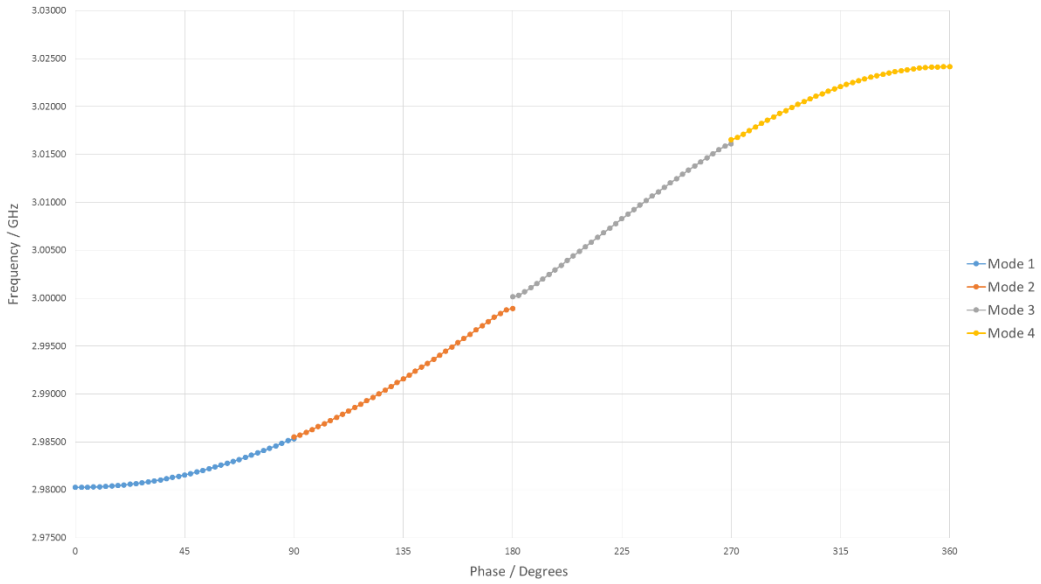

Figure 33 – Initial Dispersion Curve for the LIBO Structure

From this, the coupling constant can be calculated. Referring back to Equation (45), the following calculations were performed in order to get the initial value of 'k'.

$$\frac{2\pi(f_\pi - f_0)}{2\pi(f_{\pi/2})} = -k$$

$$\frac{(f_\pi - f_0)}{(f_{\pi/2})} = -k$$

$$\frac{(3.024158924112 - 2.9802593576835)}{(3.0001332008715)} = -k$$

$$-k = 0.0146325391205124$$

$$\therefore -k = 1.46\%\ (3SF)$$

The value of 1.46% is much lower than the required coupling coefficient of 4.4% (in-between the two published values). In order to get this value closer to the value of 4.4% the coupling slot had to be altered in order to allow more of the field to propagate from the accelerating cavities to the coupling cells. The

control parameter used to do this was 'Y_CUT'. This parameter allowed the intersection between the accelerating cavity and the coupling slots to be changed; hence changing the coupling. A parameter sweep was conducted, as shown in Section 0, which allowed a coupling coefficient of 4.4% to be returned.

However, altering the value of 'Y_CUT' until the coupling coefficient was correct, also altered the operational frequency. This meant that the radii of the accelerating and coupling cells had to be varied again in order to return a resonant frequency of 3 GHz. Following this the coupling coefficient was referred back to and returned back to 4.4%. This iterative process was carried out, becoming closer each time, until the frequency and K value were fulfilled to an appropriate degree of accuracy. This process proved to be incredibly time consuming but in order for an accurate representation of the operational characteristics and to produce a suitable reference structure, both the frequency and K value had to be correct and they both had to be altered back to their correct values after any change in parameter.

In order to check that the data returned was typical for a cavity structure, literature was referenced and Figure 34 shows a published data set. It is clear that the results returned from the LIBO structure and the published data show the same trend which strengthens the method conducted and results gained at this stage.

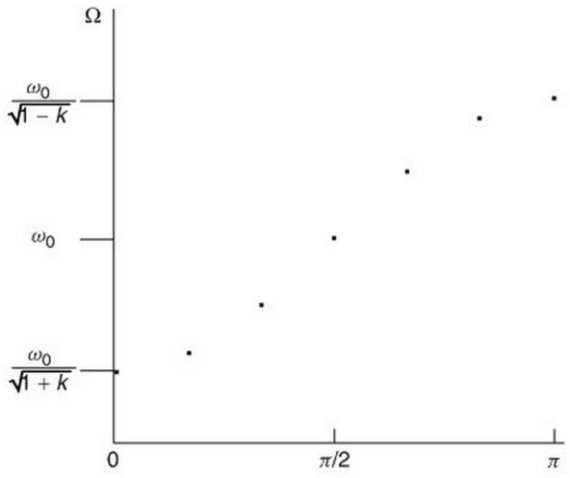

Figure 34 – Dispersion Curve from Literature [3]

1.2 Optimising in CST Microwave Studio

In order to get the cavity to operate as well as possible, the dimensions had to be altered in order to optimise the cavity with respect to various operational figures of merit.

As previously discussed, when comparing the effect of dimensional changes on operational characteristics, the value of the coupling coefficient and the resonant frequency has to be kept constant. Furthermore, Equations (43) and (45) imply that changing the dimensions of the cavity changes its coupling coefficient as well as its resonant frequency. Hence the iterative process necessary to get frequency and the K value within their respective tolerances was to be performed each time a parameter was changed; although less data points could be simulated for in order to speed up the process. This process is described in detail in the previous section.

1.2.1 Nose Cone Optimisations

The nose cones are features of the cavity that greatly influence its operational characteristics and quality of performance. The initial nose cone design of the side coupled structure, using the cavity's cross section, can be seen in Figure 35.

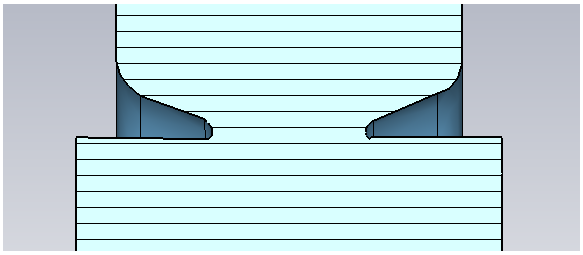

Figure 35 – Initial Shape of the Nose Cones

Due to the length of time needed to get the K value and the frequency to the correct values after each parameter change, in order to accurately analyse the effect of the change, it was decided that an alternative method of nose cone optimisation was needed to be used. Optimisation Theory was adopted in order to do this. Optimisation theory defines linear trends and relationships between specific

dimensions and operational characteristics. It is then possible to use these relationships in order to analytically create an optimal structure with respect to an array of performance requirements.

The decision to use Optimisation Theory meant that less simulations were needed in order to carry out the optimisation of the nose cones. This reduction in time meant that a wider array of values of each parameter could be assessed during the optimisation as well as a larger combination of nose cone parameters.

1.2.1.1 Quantities Used in Optimisation

It was decided that the operational characteristics for the cavity structures designed in this project will be assessed initially in terms of the shunt impedance, Section 5.1, and the modified poynting vector. It was possible to take into account more factors using the optimisation theory technique but the simulations and iterations required would be too large for a project such as this one with the time limitations that are present.

The shunt impedance is a figure of merit used in cavity design and the aim of the cavity designer is to increase this value as much as feasibly possible without sacrificing other relevant figures of merit or required performance characteristics.

The modified poynting vector (MPV) is a newer concept used for high gradient accelerating structures in order to achieve the required accelerating characteristics whilst providing a limit to reduce the chance of RF breakdown [36]. The aim during cavity optimisation was to decrease the value of this quantity as much as possible. For this reason, the variations of the shunt impedance and modified poynting vector had to be assessed and the cavity had to be designed in order to produce a structure where the shunt impedance was as high as possible and the modified poynting vector as low as possible.

An array of initial simulations showed that for most parametric alterations, both values varied proportionally, Figure 36. This meant that if the shunt impedance decreased so did the MPV; this

strengthened the need for an analytical approach to optimisation, in order to find the dimensions necessary to minimise the effect of the trade-off between these values.

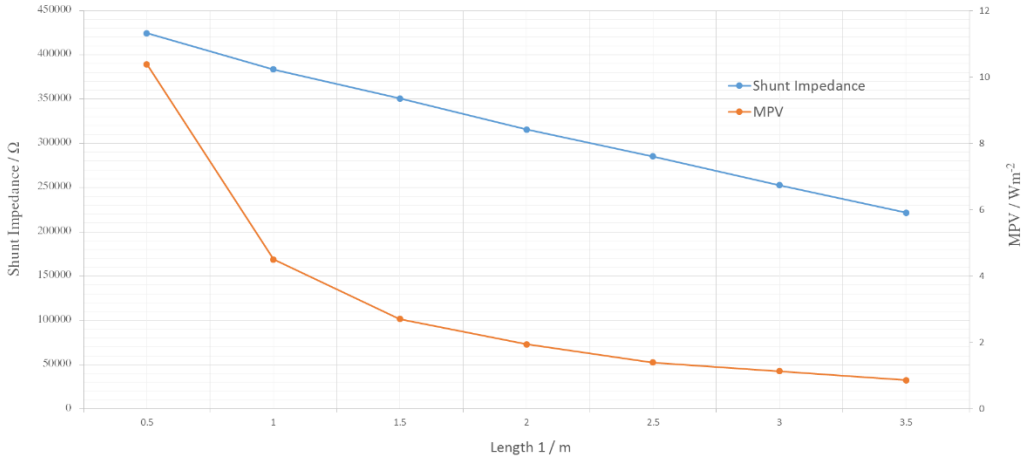

Figure 36 – Variation of Shunt Impedance and MPV with the Change of a Nose Cone Parameter Length

1.2.1.2 Goal Function

In order to produce a single value for comparison of the cavity with different shapes and sizes of nose cones, a goal function was derived. Firstly the limits of the chosen variables had to be assessed in order to evaluate how far away the simulated values were from these. The limits of each operational characteristic, denoted 'figure of merit', can be seen in Table 6.

Table 6 – Optimisation Variable Characteristics

Figure of Merit	Value	Units
Modified Poynting Vector	$\frac{\sqrt{2.4}}{35}$	$W\mu m^{-2}$
Shunt Impedance (R_s)	1.96×10^6	Ω

The limit for the MPV represented the upper limit and, conversely, the value of 1.96×10^6 was the minimum shunt impedance (R_s) value required of the cavity. The MPV limit was extracted from literature as a suitable limit for operation [36]. The limit for the shunt impedance was derived from conventional equations and known values. The derivation is represented in Equations (46) to (49).

$$R_{s\,(Needed)} = \frac{{V_T}^2}{{P_T}^2} \tag{46}$$

As the analysis is being performed on a unit cell:

$$R_{s\,(Needed)} = \frac{(V_C \times N)^2}{(P_C \times N)^2} \tag{47}$$

Using the relationship: $V = E_{acc} \times L$

$$R_{s\,(Needed)} = \frac{(E_{acc} \times L \times N)^2}{(P_C \times N)^2} \tag{48}$$

$$R_{s\,(Needed)} = \frac{(E_{acc} \times L)^2}{(P_C)^2} \tag{49}$$

From operational values given:

$$E_{acc} = 35MVm^{-1}$$

$$Pc = \frac{P_T}{N} = \frac{10 \times 10^6}{13} = 7.69 \times 10^5\ (3SF)$$

$$\therefore R_{s\,(Needed)} = 1.96 \times 10^5\ (3SF)$$

Where:

R_s	=	Shunt Impedance / Ω
V_T	=	Total Voltage / V
P_T	=	Total Power / W
V_C	=	Voltage Per Unit Cell / V
P_C	=	Power Per Unit Cell / W
E_{acc}	=	Accelerating Electric Field / Wm^2
L	=	Length of Unit Cell / m

Following the derivation of the limitation values for both the shunt impedance and for the modified poynting vector, the goal function equation could be formed.

$$Goal\ Function\ (G) = \alpha + \beta = \frac{A}{X} + \frac{B}{Y} \tag{50}$$

For the above equation, A and B are the values which represent the system, i.e. the values outputted from CST MWS, whereas X and Y represent the limits of the system. In this respect it can be seen that as the values, A and B, deviate from the limits, X and Y, the goal function increases or decreases depending on how it is set up.

For this project the goal function was set to decrease with optimisation. The resultant equation can be seen in Equation (51).

$$Goal\ Function\ (G) = \frac{\frac{\sqrt{Sc}}{E_{acc}}}{\frac{\sqrt{Sc}}{E_{acc\ (Needed)}}} + \frac{\frac{1}{R_s}}{\frac{1}{R_{s\ (Needed)}}} \tag{51}$$

It is clear that α decreases as the outputted modified pointing vector is reduced. In order to decrease the value of β in this way, the reciprocals were compared. This meant the higher the value of the shunt impedance, the lower the goal function.

Following the formation of the goal function, a linearisation technique using differential equations could be performed in order to provide the data necessary for optimisation theory.

1.2.1.3 Linearisation Using Differential Equations

The parameters to be altered, in order to optimise the nose cones, are shown in Figure 37.

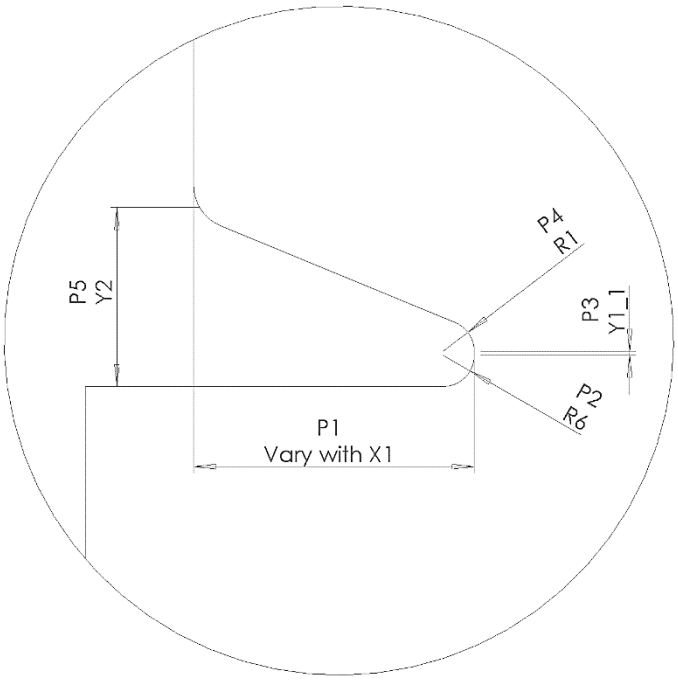

Figure 37 – Nose Cone Parameters to be Varied

In order to provide the linearisation data for the analytical optimisation, differentials needed to be calculated which dictated how a change in each parameter would affect both the modified poytning vector and the shunt impedance. In order to do this, the cavity had to be simulated 11 times in order to provide data for two variations of each parameter with respect to a base state.

1.2.1.3.1 Initial Optimisation

Each parameter was to be altered by a defined quantity and a simulation carried out to observe the effect on both the modified poynting vector and the shunt impedance. It should be noted that, although the shunt impedance is measureable as a direct output from CST MWS, the modified poynting vector is not. For this reason an array of calculations had to be conducted with data available from CST MWS.

To calculate the MPV, referring back to Section 1.1, a line needed to be placed on the surface of the cavity. This line was drawn around the nose cones of the structure. By designing the cavity using the new method of implementation devised in this project, the line could simply be parameterised using the cross section parameters used to construct the cavity initially. This meant that any parametric changes would change not only the structure's dimensions, but also the geometry of the line concordantly. This line is shown in Figure 38.

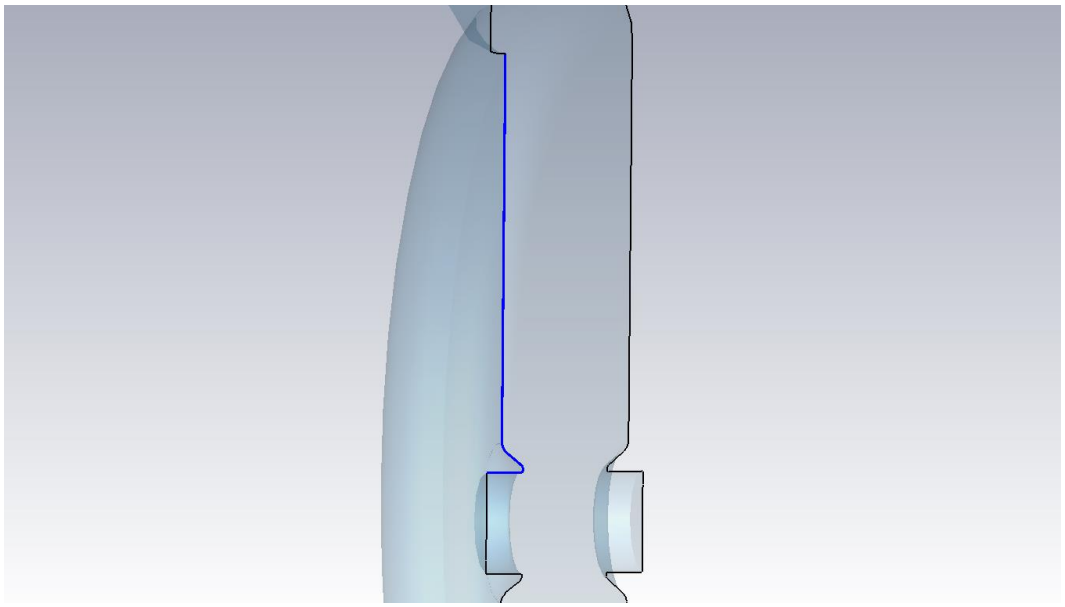

Figure 38 – 2D Parameterised Curve (in Blue) for Surface Field Analysis

Following this, a post processing step was set up to calculate the magnitude of the surface current (S_C) at each point along the line. The result of this is shown in Figure 39.

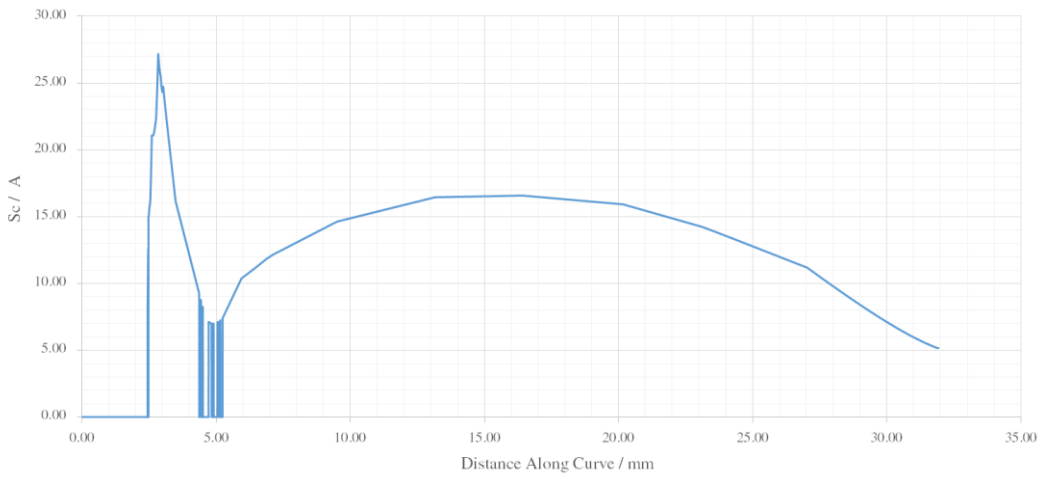

Figure 39 – Magnitude of S_C along the Length of the 2D Curve

From this, and other direct outputs from CST MWS, the modified poynting vector could be calculated. Equation (52) shows the final calculation for the modified poynting vector and Table 7 shows the simulation data outputted from CST MWS after a parameter had been changed and the frequency and K values had been reverted back to the values of 3 GHz and 4.4% respectively. The data was used in order to arrive at the components of the final equation, as well as value of the goal function for the cavity.

$$\frac{\sqrt{S_C}}{E_{acc}} \tag{52}$$

$$E_{acc} = \frac{V}{l} \tag{53}$$

Where: S_C = Curface Current / A

E_{acc} = Accelerating Electric Field / $\mathrm{Vm^{-1}}$

V = Voltage / V

l = Length / m

Table 7 – Simulated Data Needed to Calculate the Modified Poynting Vector (Extracted from Excel Spreadsheet Constructed for Optimisation Theory Analysis)

f_{M1} Corrected	R_S M1	Q-Factor	V	E_{PK}	B_{PK}	S_C
2.99945	327291	6180.89	997647	1.14E+09	1.69E+06	6.88E+13

$S_C/5$	E_{acc}	$(\sqrt{S_C})/E_{acc}$	E_{PK}/E_{acc}	B_{PK}/E_{acc}	MPV at 35MV/m	X
1.38E+13	9.00E+01	4.12E-02	1.27E+07	1.88E+04	2.08288375	0.044262667

A	Pc	Y	B	G
9.32E-01	7.69E+05	5.11E-06	5.98E-01	1.53E+00

The table shows the frequency as 'f_{M1} – Corrected', this is because it is the frequency returned after the correct dimensions, 'Y3' and 'Y_CUT', had been found which the make the frequency and the coupling coefficient conform with their required values. The iterative methods described in Section 1.1.4 were used to achieve this. Table 8 shows the final calculation of the coupling coefficient resulting in a value of 4.4% within a defined tolerance.

Table 8 – Coupling Coefficient Calculation

f_1 - 0^0	f_2 - 360^0	f_3 - 0^0	f_4 - 360^0	K	K / %	K (2SF) / %
2.95067	2.99418	3.00039	3.0825	0.043951391	4.395139109	4.4

After setting up the simulations and tables necessary to evaluate the structure, the parameter alterations were started. The simulated changes as well as the differentials for each parameter are displayed in Table 9. As discussed, after each change in cavity geometry the radius of the accelerating cavity had to be changed, by iteratively changing 'Y3', in order to keep a constant frequency. Following this, the coupling coefficient was kept at a value of 4.4% by altering the value of 'Y_CUT'.

Recapping the technique used and explained previously, optimising for the frequency effected the coupling coefficient and optimising for the coupling coefficient altered the frequency. This meant that the simulations had to be conducted until both 3 MHz and 4.4% coupling were apparent and only then could the data be used to calculate the shunt impedance (R_S) and the modified poynting vector (MPV). As expected, changes in radii had the least effect on the frequency and the coupling coefficient as they have the least effect on the overall radius of the cavity, which depicts its frequency.

Table 9 – Initial Parameter Changes to Identify their Effects on the Goal Function

X1	R_S	MPV	dX1	dR_S	dR_S /dX1	dMPV	dMPV/dX1
1.5	350859	0.047075					
2	315773	0.039898	0.5	-32810	-65620	-0.00664	-0.01328
2.5	285239	0.033791					

R6	R_S	MPV	dR6	dR_S	dR_S/dR6	dMPV	dMPV/dX1
0.13	317939	0.039653					
0.15	315773	0.039898	0.02	-2277	-113850	0.000189	0.009467
0.17	313385	0.040032					

Y1_1	R_S	MPV	dY1_1	dR_S	dR_S/dY1_1	dMPV	dMPV/dX1
0.5	317475	0.040144					
0.4	315773	0.039898	0.15	1291.5	8610	0.000319	0.002125
0.6	320058	0.040781					

R1	R_S	MPV	dR1	dR_S	dR_S/dR1	dMPV	dMPV/dX1
0.1	318274	0.045477					
0.3	315773	0.039898	0.125	-1740	-13920	-0.00319	-0.02551
0.35	314794	0.0391					

Y2	R_S	MPV	dY2	dR_S	dR_S/dY2	dMPV	dMPV/dX1
0.5	316506	0.040707					
1	315773	0.039898	0.5	-282	-564	-0.00092	-0.00183
1.5	315942	0.038875					

The differentials allowed the parameters to be altered using spreadsheet software and the resulting modified poynting vector and shunt impedance could be resulted from this. This meant that a new goal function could be calculated.

In order to do this, a differential equation had to be derived which allowed the theoretical deviation in the modified poynting vector and shunt impedance to be calculated and the effects added to the results from the base state:

$$R_s = R_s(0) + \frac{dRs}{dX1} + \frac{dRs}{dR6} + \frac{dRs}{dY1\_1} + \frac{dRs}{dR1} + \frac{dRs}{dY2} \tag{54}$$

$$\frac{\backslash \overline{Sc}}{E_{acc}} = \frac{\backslash \overline{Sc}}{E_{acc}}(0) + \frac{d\frac{\backslash \overline{Sc}}{E_{acc}}}{dX1} + \frac{d\frac{\backslash \overline{Sc}}{E_{acc}}}{dR6} + \frac{d\frac{\backslash \overline{Sc}}{E_{acc}}}{dY1\_1} + \frac{d\frac{\backslash \overline{Sc}}{E_{acc}}}{dR1} + \frac{d\frac{\backslash \overline{Sc}}{E_{acc}}}{dY2} \tag{55}$$

Iterations of different parameter combinations could then be performed using the spreadsheet in order to result in the lowest value of the goal factor.

1.2.1.3.2 Analysis

After calculating the numerical effect of changing each parameter on the shunt impedance and modified poynting vector, several trials were conducted which aimed to analytically change values, using spreadsheet software, in order to get the goal factor to its lowest possible value. A selection of these trials can be seen in Table 10.

Table 10 – Example of Initial Parameter Permutations in Order to Lower the Goal Factor

Parameter	Initial	Trial 1	Trial 2	Trial 4	Trial 7
X1	2	2.1	2.2	2.3	2.4
R6	0.15	0.15	0.15	0.15	0.15
Y1_1	0.4	0.4	0.4	0.4	0.4
R1	0.3	0.3	0.3	0.3	0.3
Y2	1	1	1	1	1
Rs	**315773**	**309211**	**302649**	**296087**	**289525**
MPV	**0.039897501**	**0.038569103**	**0.03724071**	**0.035912307**	**0.034583909**
G	**1.52E+00**	**1.50E+00**	**1.49E+00**	**1.47E+00**	**1.46E+00**

Parameter	Trial 10	Trial 15	Trial 19	Trial 23	Trial 27
X1	2.8	2.8	2.8	3	3
R6	0.15	0.15	0.15	0.15	0.05
Y1_1	0.4	0.5	0.6	1	1
R1	0.3	0.4	0.4	0.5	0.5
Y2	1	1	1	2	2
Rs	**263277**	**262746**	**263607**	**251971**	**263356**
MPV	**0.029270317**	**0.02693211**	**0.027144587**	**0.020954845**	**0.020008159**
G	**1.41E+00**	**1.35E+00**	**1.36E+00**	**1.25E+00**	**1.20E+00**

As the iterations were carried out further, Table 11, values were becoming extremely low and some were even becoming negative, which is impossible. The goal function was becoming too low to represent realistic operational characteristics for a cavity system. The reason for this was due to the linearisation of non-linear data. Although for small intervals the calculations provide accurate enough data for analytical optimisation outside CST MWS, as the parameter values deviate further from the ranges where the differentials in Table 9 were generated, the results become less accurate.

Table 11 – Parameter Permutations Showing Unfeasible Results

Parameter	Trial 31	Trial 32	Trial 35	Trial 37	Trial 38
X1	2.5	3.5	2.5	3.5	3.25
R6	0.01	0.01	0.01	0.01	0.01
Y1_1	0.5	0.5	1	0.5	0.5
R1	2	2	2.2	2	3
Y2	2	2	2	9	9
Rs	**275535**	**209915**	**277056**	**205967**	**208452**
MPV	**-0.01305**	**-0.02634**	**-0.01709**	**-0.03916**	**-0.06135**
G	**4.16E-01**	**3.38E-01**	**3.21E-01**	**6.61E-02**	**-4.46E-01**

In order to overcome this, a set of values that produced a goal factor that was low, but not low enough to be seen as unreasonable was set and a new set of differentials around these values were generated, again using CST MWS simulations. This would allow a more accurate impression of the effect of different parameters at values for which a lower goal function had been shown.

1.2.1.3.3 Second Optimisation

Trial 27 was carried forward as the goal factor was reduced sufficiently, from 1.52 to 1.20 (3SF), but was not low enough to be seen as unrealistic. The differentials, and hence another 11 simulations, were then re-calculated at the new values and these can be seen in Table 12.

.

Table 12 – Second Set of Parameter Changes to Identify their Effects on the Goal Function

X1	R_S	MPV	dX1	dR_S	dR_S/dX1	dMPV	dMPV/dX1
2.5	288887	0.032581					
2	315773	0.039898	0.5	-31617	-63234	-0.00411	-0.00822
2.5	285239	0.033791					

R6	R_S	MPV	dX1	dR_S	dR_S/dX1	dMPV	dMPV/dX1
0.01	259076	0.028781					
0.5	258176	0.039898	0.045	-4070.5	-90455.6	-9.6E-05	-0.00214
0.1	250935	0.028589					

Y1_1	R_S	MPV	dX1	dR_S	dR_S/dX1	dMPV	dMPV/dX1
0.8	256518	0.027899					
1	258176	0.039898	0.2	675	3375	0.000648	0.003239
1.2	257868	0.029195					

R1	R_S	MPV	dX1	dR_S	dR_S/dX1	dMPV	dMPV/dX1
0.3	255682	0.02973					
0.5	258176	0.039898	0.2	60.5	302.5	-0.00081	-0.00406
0.7	255803	0.028105					

Y2	R_S	MPV	dX1	dR_S	dR_S/dX1	dMPV	dMPV/dX1
1.5	260822	0.02871					
2	258176	0.039898	0.5	-332.5	-665	-0.00047	-0.00094
2.5	260157	0.02777					

Again, analytical iterations were carried out which produced a theoretical modified poynting vector, shunt impedance and goal function. A selection of results from the second set of iterations are shown in Table 13. The first trial, Trial 40, represents the values of the parameters around which the differentials were generated. Trial 40 has the same values as Trial 19 but it can be seen that the goal factor changes from 1.20 to 1.40. This shows the need for the more accurate differentials, as in the first block of iterations the goal factor was deviating massively as the parameters became further away from the points simulated.

Table 13 – Example of Parameter Permutations Using the Second Set of Differential Values

Parameter	Trial 40	Trial 41	Trial 42	Trial 45	Trial 48
X1	3	3	3	3.5	3.3
R6	0.05	0.05	0.05	0.05	0.05
Y1_1	1	1	1	1	1
R1	0.5	0.5	0.7	0.7	0.7
Y2	2	2	2	2	2
Rs	**258176**	**258176**	**258236.5**	**226619.5**	**239266.3**
MPV	**0.02859**	**0.02859**	**0.027777**	**0.023667**	**0.025311**
G	**1.404488**	**1.404488**	**1.385953**	**1.398906**	**1.390369**

Parameter	Trial 61	Trial 68	Trial 72`	Trial 78	Trial 81
X1	2.7	2.7	2.8	2.8	3
R6	0.1	0.1	0.05	0.05	0.05
Y1_1	1	1	1	1	1
R1	0.7	1	1.5	2.5	2
Y2	3	3	3.5	2	5
Rs	**272018.9**	**272109.7**	**270127.8**	**271427.8**	**256634.8**
MPV	**0.029196**	**0.027978**	**0.024761**	**0.022108**	**0.019677**
G	**1.38E+00**	**1.35E+00**	**1.28E+00**	**1.22E+00**	**1.21E+00**

Again, the goal factor was decreased throughout the iterations until a value was gained that was becoming too low to be representative of real operation.

1.2.1.3.4 Third Optimisation

A third and final set of 11 simulations to gain the differentials was then carried out around the values displayed in Trial 81. These are shown in Table 14.

Table 14 – Third Set of Parameter Changes to Identify their Effects on the Goal Function

X1	R_s	MPV	dX1	dR_s	dR_s /dX1	dMPV	dMPV/dX1
2.5	289224	0.028687					
3	259249	0.025303	0.5	-31749	-63498	-0.00184	-0.00367382
3.5	225726	0.025013					

R6	R_s	MPV	dX1	dR_s	dR_s /dX1	dMPV	dMPV/dX1
0.01	260021	0.029585					
0.5	259249	0.025303	0.045	-861	-19133.3333	-0.00194	-0.04320226
0.1	258299	0.025697					

Y1_1	R_s	MPV	dX1	dR_s	dR_s /dX1	dMPV	dMPV/dX1
0.8	256257	0.025756					
1	259249	0.025303	0.2	1554	7770	0.000439	0.002196823
1.2	259365	0.026635					

R1	R_s	MPV	dX1	dR_s	dR_s /dX1	dMPV	dMPV/dX1
1	258299	0.025814					
2	259249	0.025303	1	-1116.5	-1116.5	-7.3E-05	-7.3115E-05
3	256066	0.025667					

Y2	R_s	MPV	dX1	dR_s	dR_s /dX1	dMPV	dMPV/dX1
3	259303	0.025502					
5	259249	0.025303	2	1023.5	511.75	0.000462	0.000231195
7	257256	0.026427					

As before, these values were used to systematically to assess the best combination of parameters in order to lower the goal function. The final permutation is displayed in Table 15 and, as shown, the goal function was lowered to a value of 1.28 to 3 significant figures. This was the lowest value achievable with the data and represented the combination of parameter dimensions which best suited the desired operational characteristics of the cavity.

Table 15 – Final Combination of Parameter Values by Linearising Non-Linear Relationships

Parameter	Trial 40
X1	3
R6	0.1
Y1_1	1
R1	2
Y2	5
Rs	**258292.33**
MPV	**0.0231426**
G	**1.28**

By using CST MWS to simulate the effect of changing each parameter on both the modified poynting vector and the shunt impedance, and hence the goal function, it was possible to produce a combination of nose cone parameter values which produced a low goal function. This combination represented the values at which the trade-off between the modified poynting vector and the shunt impedance was minimised. The shape of the final nose cones are displayed in Figure 40.

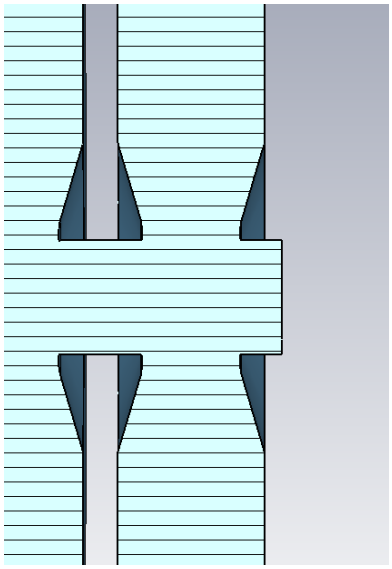

Figure 40 – Optimised Nose Cones

1.2.1.3.5 Using the Results in CST Microwave Studio

In order to check that the last combination of results was accurate, the values, shown in Table 15, were applied to the cavity in CST MWS. After carrying out the necessary simulations, the goal function was found to be 1.31. This result was as expected; it was slightly higher than the value gained using the theoretical manipulation, due to the innate errors associated with the linearisation of non-linear variables and trends, but was small and close enough to the value of 1.28, Table 15, to strengthen the fact that this was the best combination of parameter values.

The first and final values of the goal function, both calculated using results directly from CST MWS, were 1.52 and 1.31 respectively. This meant that the goal function was successfully reduced using mathematical manipulation of simulation results which depicted the effect of parameter changes on the modified poynting vector and the shunt impedance.

This approach proved to be a highly successful method of optimisation as it prevented the need to simulate the cavity structure hundreds of times. This would have been unfeasible for a project of this length as the parameters would have had to be manually altered after each simulation as the in order to continually improve the characteristics whilst keeping the frequency and K value correct.

After the simulations had been carried out in CST MS, and the goal function of 1.31 returned, it needed to be checked that this was actually the lowest value that the goal function could be. In order to do this the cavity was simulated for instances where each parameter was slightly above and slightly below its value set out in Table 15. The corresponding goal functions for each of these values are displayed in Table 16.

Table 16 – Simulated Data for Values Above and Below each Parameter

Parameter	Value	Goal Function
Initial	-	1.317870
X1	3.1	1.333306
X1	2.9	1.324102
R6	0.15	1.325988
R6	0.05	1.344716
R1	1.9	**1.317475**
R1	2.1	1.325545
Y1_1	0.9	1.334373
Y1_1	1.1	**1.30931**
Y2	4.5	1.326914
Y2	5.5	1.325970

From the table it is clear that the optimisation approach produced a combination of parameter values which gave a very low goal function. However, due to the non-linear relationship between each parameter and the goal function constituents, in two cases it was possible to make the goal function slightly lower. This was predicted to be the case as the theoretical manipulations could only predict the results based on linear trends but the relationships being simulated are not always linear at such small intervals. For this reason, the last part of the nose cone optimisation consisted of several simulations in order to make the goal function as low as possible around the ballpark figures, of which most were the optimum, gained from the previous theoretical optimisations.

After several simulations, utilising the information given by the lower goal functions from Table 16, it was seen that the best goal function occurred when Y1_1 was increased by 0.2 and all other parameters were kept constant. The final nose cone geometries are displayed in Table 17.

Table 17 – Final Nose Cone Parameter Values

Parameter	Trial 40
X1	3
R6	0.1
Y1_1	1.2
R1	2
Y2	5
Rs	**258292.33**
MPV	**0.0231426**
G	**1.30**

To confirm that Table 17 represented the best geometries, a Pereto Chart was plotted. This allowed the best combination of parameters to be visibly identified and the data range included all of the simulation results carried out after the modelling using spreadsheet software. The chart is displayed in Figure 41.

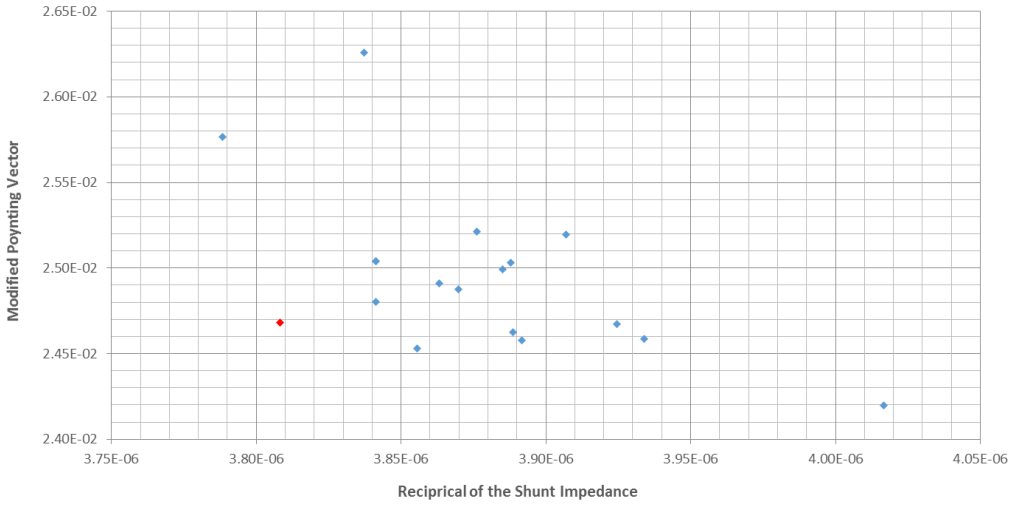

Figure 41 – Pareto Chart Comprising the Final Simulated Parameter Combinations

Each point on the chart represents a combination of parameter values. The chart has the modified poynting vector on the y-axis and the reciprocal of the shunt impedance on the x-axis. This meant that

the lower the values on each axis, the better the operational characteristics and hence goal function. For this reason the data point closest to the axis intersection represents the best combination of parameter values. As expected this point, highlighted in red, represented the data in Table 17.

1.2.1.4 Coupling Cell Optimisation and Peak Fields

Following the optimisation of the nose cones, the coupling cells had to be optimised in order to create a structure which could be used as a point of comparison for the final structure. It was found that the accelerating characteristics were not greatly affected by the geometries of the coupling cells, rather they just altered the frequency; for this reason they were kept with similar ratios to that of the LIBO structure. However, through further analysis using CST MWS, it was seen that at the point of intersection between the accelerating cavity and coupling cells, there was an area of peak magnetic field over a very small area, the presence of which contribute to field breakdown. For this reason, the cavity needed to be altered in order to spread and reduce the magnetic fields to the smallest possible value. It was seen that sharp peaks were the areas of highest field, Figure 42. Therefore, the sharp edges were reduced by adding parametrically defined blends.

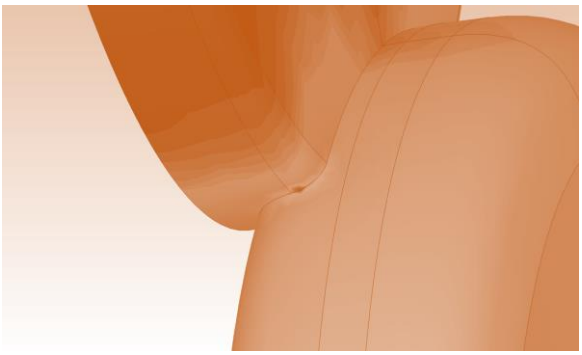

Figure 42 – Peak Magnetic Field

Without any optimisation, the peak magnetic field (H_{PK}) was outputted as 1.674 MAm^{-1}. For convention the outputted value from CST MWS was converted into $NA^{-1}m^{-1}$ by multiplying the answer by the permeability of free space ($\mu_0 = 4\pi \times 10^{-7}$). This gave an initial value (B_{PK}) of 18.073 $NA^{-1}m^{-1}$ (3DP).

In order to reduce the sharp peaks, the intersection was initially filleted, referred to as blended by the CST MWS interface, at the location of the peak magnetic field. The fillet radius was set to 0.5mm. This would assess whether the idea of eliminating the sharp section was viable. This is shown in Figure 43.

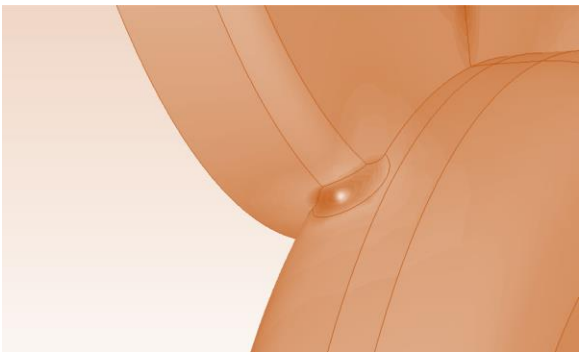

Figure 43 – Initial Reduction of the Peak Magnetic Field

It was found that the peak magnetic field spread over the filleted area, reducing the value of B_{PK} to 13.594 $NA^{-1}m^{-1}$. Following this, the radius of the fillet was swept between 0.5mm and 0.7mm. This range was chosen as above and below it, there were feature intersections creating manufacturing impossibilities and meshing errors within the software. The general trend observed was that the larger the radius, the smaller the peak magnetic field. The data from CST MWS is plotted in Figure 45, labelled 'Initial Fillet'.

After the first set of data was collected, another filleting method was analysed. This time the entire intersecting area was filleted, Figure 44. This was done, not only to reduce the peak magnetic fields, but to also create a structure that was easier to manufacture. The intersecting are shown in Figure 43 would be incredibly difficult to build and a goal during this project was to keep manufacturing possibility in mind when designing the structures.

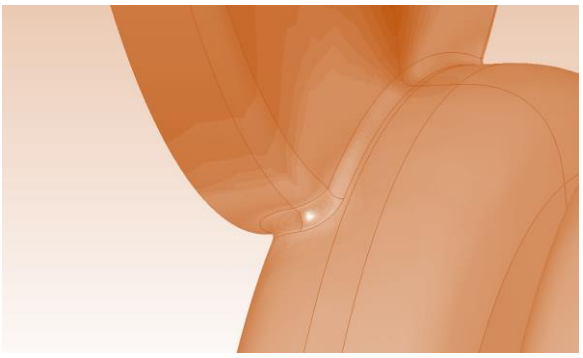

Figure 44 – Whole Intersection Fillet

The radius was again set back to 0.5mm. This time the value of B_{PK} was 13.431 $NA^{-1}m^{-1}$. In order to reduce this value further, the radius of the fillets as well as the order in which the edges were picked and filleted needed to be experimented with. Firstly, the order in which the edges were filleted was experimented with. It was found that the initial order of filleting gave the lowest peak magnetic fields and so this order was chosen. Following this, another parameter sweep was conducted through a slightly larger range than the initial trial and with smaller intervals. Figure 45 shows the results of the parametric variations.

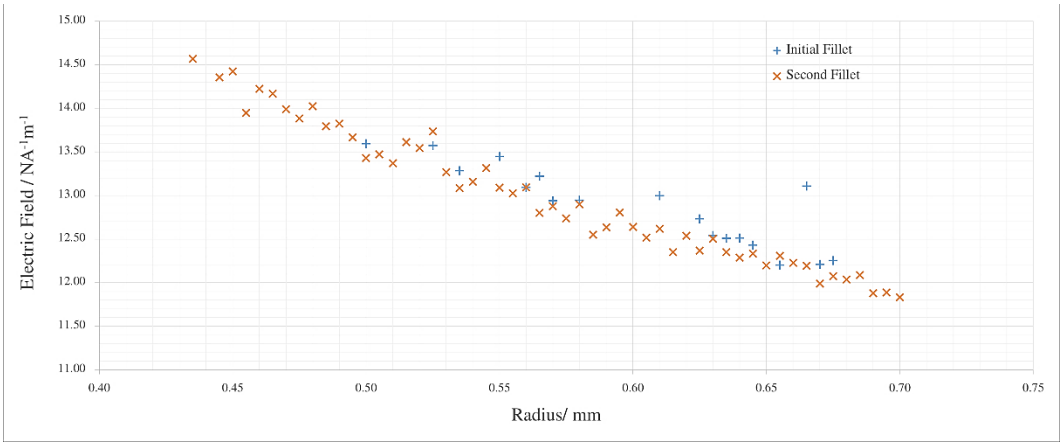

Figure 45 – Intersection Radii Parameter Sweeps

Following the sweeps it was seen that the best value for the peak magnetic field was 11.834 $NA^{-1}m^{-1}$ which corresponded to a fillet radius of 0.7 mm.

At this point the 24 MeV side coupled structure was seen as a valid reference point to compare with the structure to be designed and built. The frequencies and coupling factor were fine-tuned, as although constant throughout optimisations, there were tolerances in place to decrease the time spent optimising at each stage. These tolerances were decreased to allow a more accurate structure for reference and the side coupled structure marked as finalised.

2 Annular Coupled Structure

It was decided that the structure to be built in this project was to be an annular coupled structure (ACS), Section 5.5.2.4. In addition to the advantages discussed in the literature review, this structure was mainly chosen to assess its viability compared with the current state of the art. The ACS's coupling cell revolves completely around the accelerating cavity, adding inherent symmetry to the design. This symmetry allows for easier manufacture and also means symmetry planes can be incorporated into the simulation software, allowing for quicker simulations.

2.1 Initial Implementation in CST Microwave Studio

The accelerating cavity, and hence the nose cones, which had been extensively designed for the LIBO structure, were implemented in the annular coupled design. This was because it was the differing coupling structures which were to be compared and analysed during the course of this project. The accelerating cavity schematic, again representing one quarter of the cavity's cross section, can be seen in Figure 46. As before, the quarter cross section can be mirrored and swept around a perpendicular path in order to produce the 3D structure. Although some parameter names have changed, the features and geometries were the same. Figure 47 shows the coupling cell; note, the coupling cell now encases the entire accelerating cavity, i.e. its central axis is the x-axis.

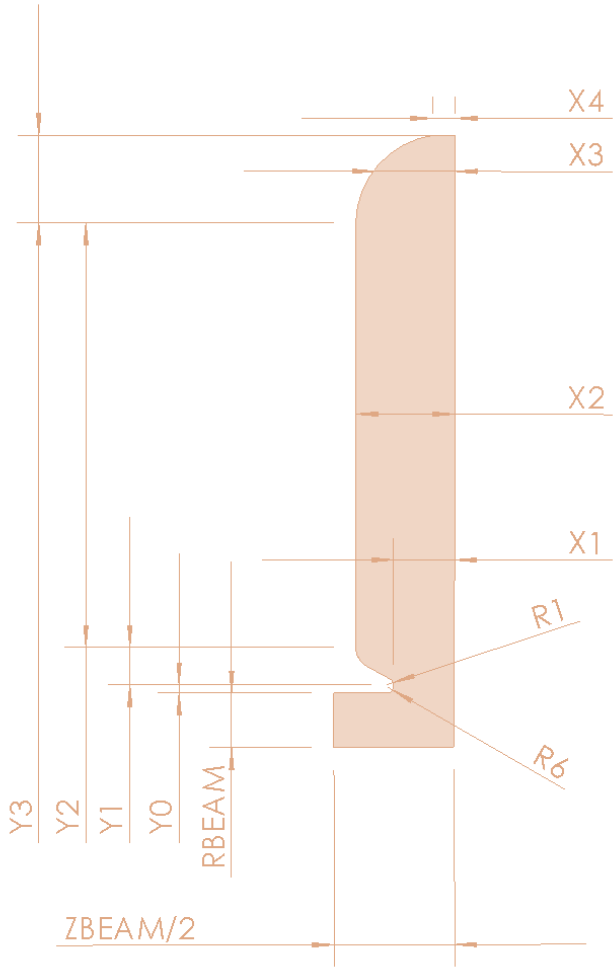

Figure 46 – ACS Sketch Features - Accelerating Cavity

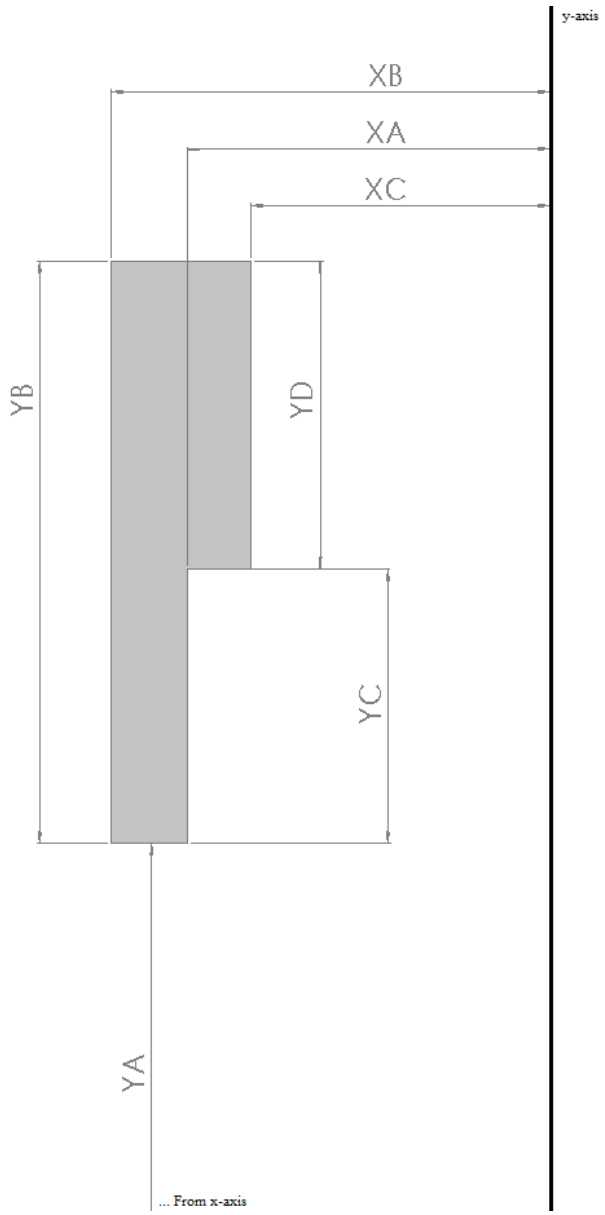

Figure 47 – ACS Sketch Features - Coupling Cell

Unlike the LIBO's side coupled structure, the accelerating cavity and coupling cells could not simply be intersected. For this reason, coupling slots had to be designed which allowed field to propagate between the cavity sections. From the research discussed in the literature review, it was decided that 4 coupling slots was the optimum amount. The initial structure is shown in Figure 48.

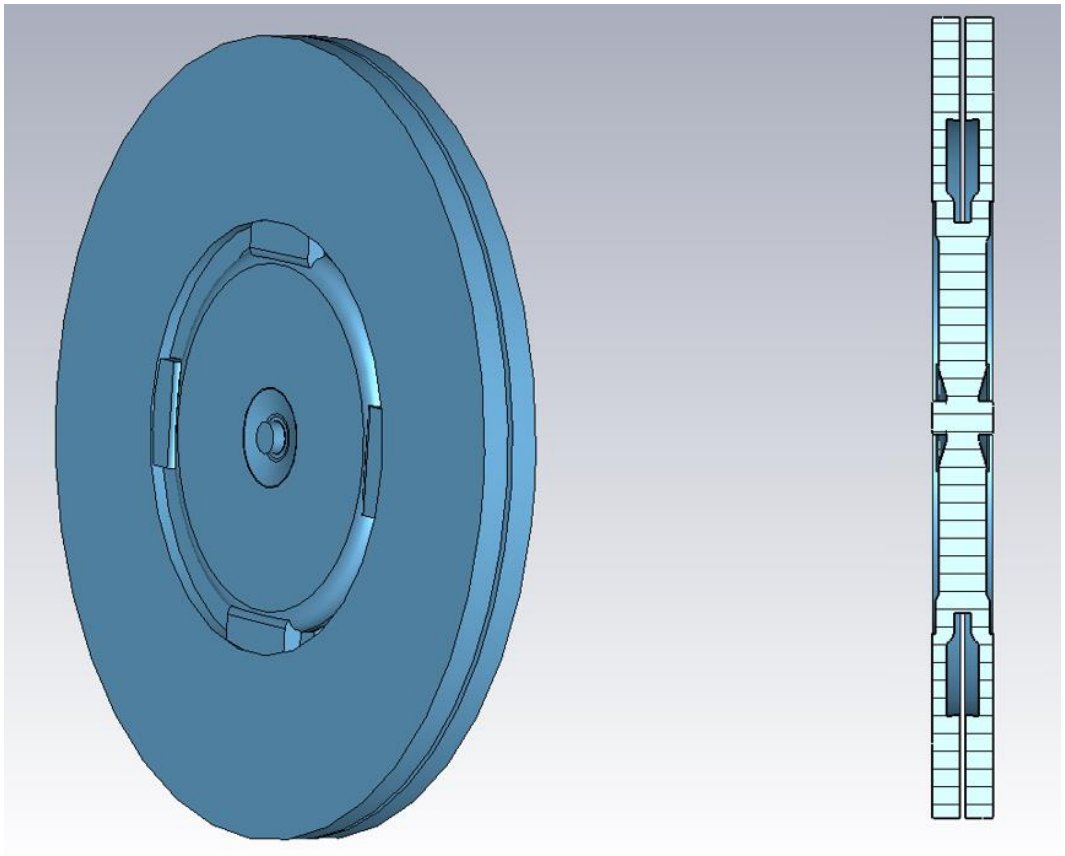

Figure 48 – Initial ACS Cavity Repeating Unit

***LEFT:** 3D Representation* ***RIGHT:** Cross Section*

The coupling slots were designed as rectangles which intersected both the coupling cells and accelerating cavities. The sharp corners of the coupling slots were rounded off in order to reduce the peak magnetic fields observed in the LIBO structure.

After the cavity was implemented in CST MWS an initial simulation was carried out to simply test the feasibility of the structure. Immediately a problem with the structure was realised. The field propagated from coupling cell to coupling cell, missing out the accelerating cavity. It was identified that the cause of this problem was that the coupling slots on the left were in very close proximity to the coupling cells on the right. The problem was solved by altering the orientation of the coupling slots on the left by 45°. The amended design is shown in Figure 49.

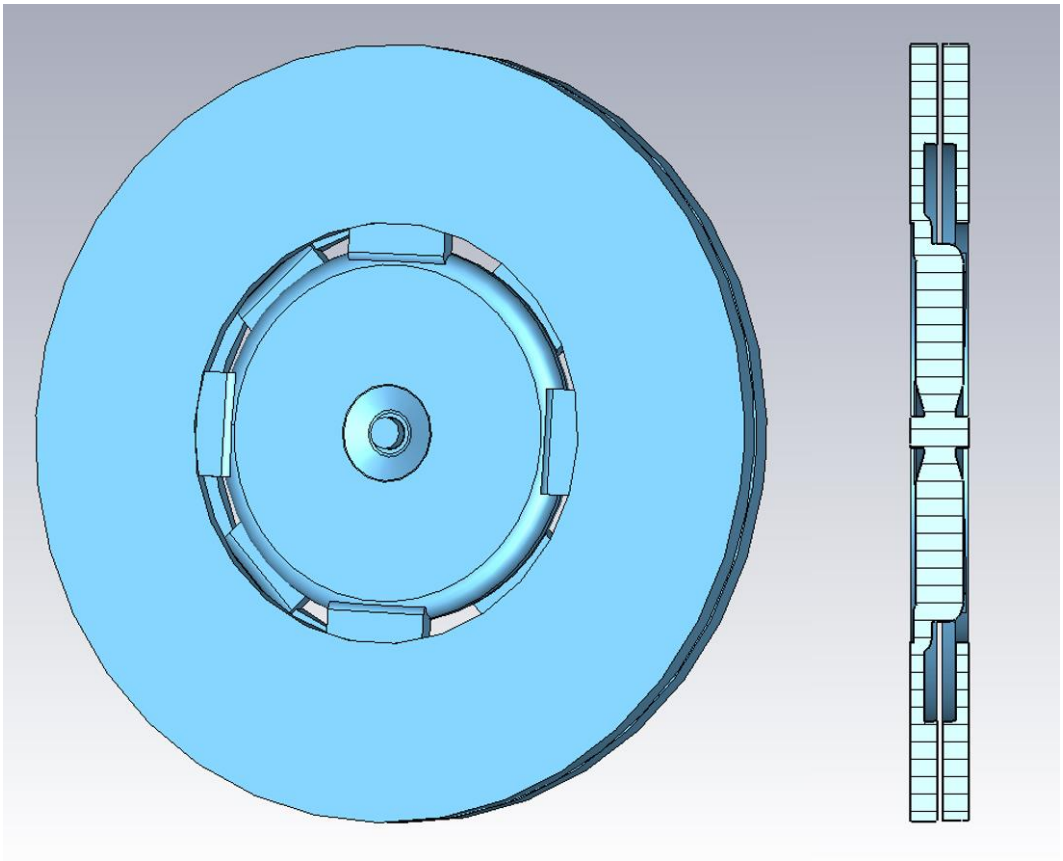

Figure 49 - Amended ACS Cavity Repeating Unit

***LEFT:** 3D Representation* ***RIGHT:** Cross Section*

2.2 Optimisation in CST Microwave Studio

As the nose cones and accelerating cavity had already been optimised, it was the coupling cells and the coupling slots that had to be altered to result in the correct and greatest operational performance. Doing this would allow a structure to be designed that could be compared with the LIBO structure.

2.2.1 Problem with Coupling Slots

After a preliminary simulation of the structure to assess its viability, it was noticed that there were many areas of intense magnetic peak fields at the coupling slot. As previously discussed, this was due to the large amount of sharp intersections. Furthermore it was decided that the cuboid coupling slot, although the easiest to implement, was not the best shape. This is because the coupling slot would exit the

accelerating cavity if lengthened during optimisation and this presented errors in terms of peak magnetic fields as well as manufacturing impossibilities.

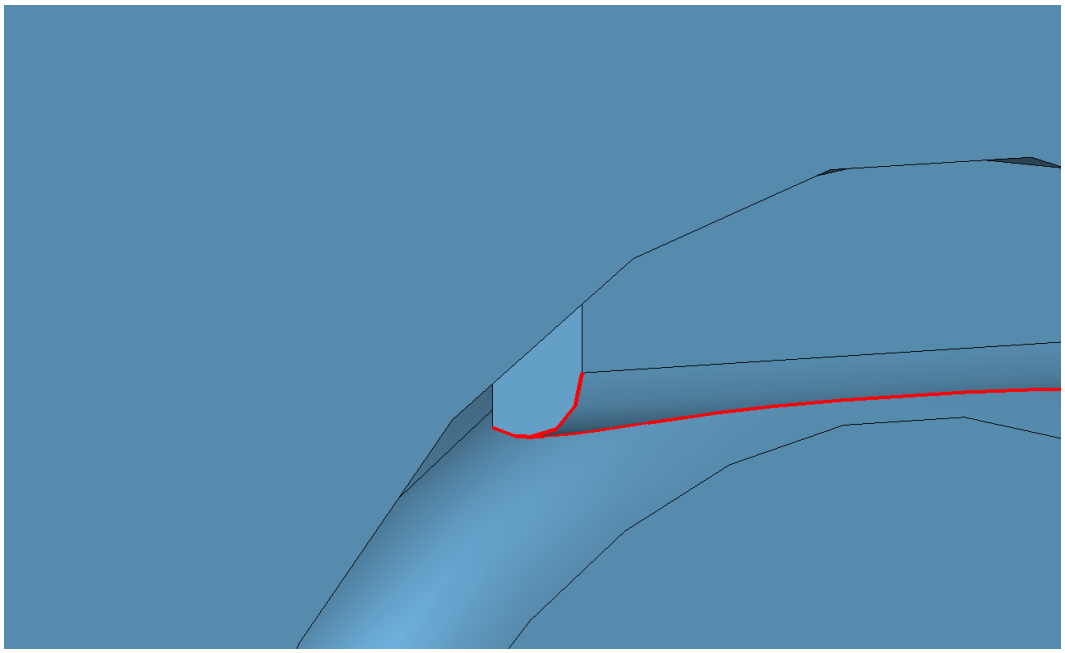

Figure 50 – Sharp Areas Incurring Large Magnetic Peak Fields and Impossible Manufacture

2.2.2 Solution to Sharp Coupling Slots

In order to reduce the sharp edges of the coupling call intersections, a rectangle was drawn, rotated and filleted, Figure 51. It was clear that this process much reduced the sharpness of the structure's coupling intersection.

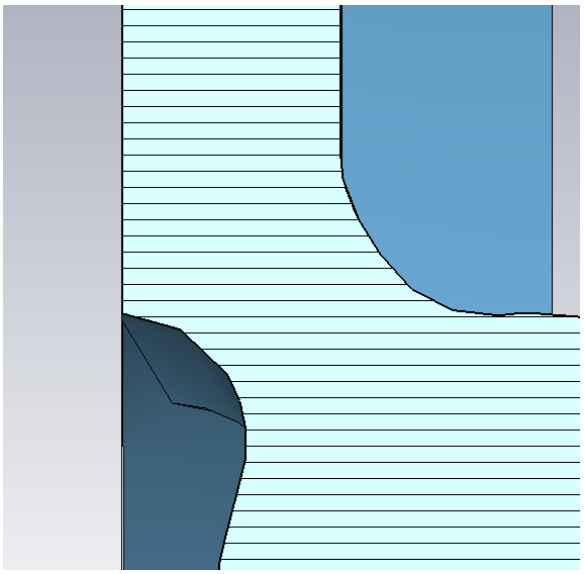

Figure 51 – Cross Section of the New Coupling Slot Orientation

However, this still left the problem that the coupling slot would leave the accelerating cavity when lengthened. In addition to this, the blends and fillets added to the structure in order to decrease the peak magnetic fields were corrupted when the coupling cell left the accelerating cavity.

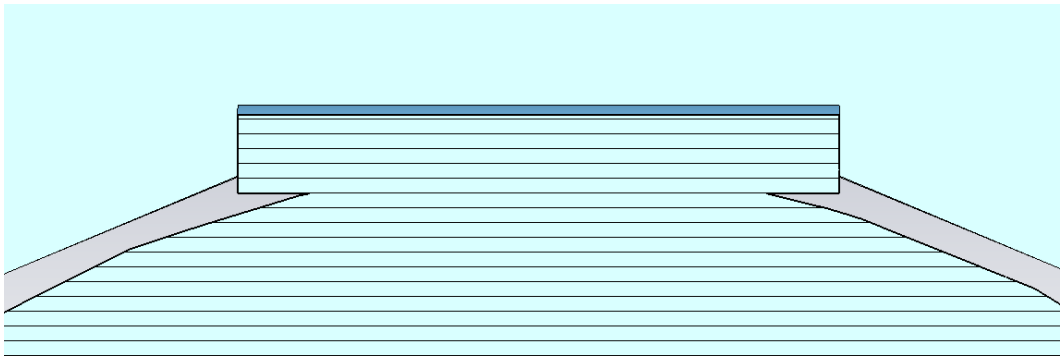

Figure 52 – Sharp Areas and Impossible Manufacture Due to Elongation of the Coupling Slot

In order to solve this problem, it was firstly decided to simply filet the corners. Although this would solve the problem, it would have meant an impossible manufacture as there would be several radii in one location which is unmanageable for a CNC lathe. Furthermore, the process would have needed to have been carried out every time the fillets corrupted with elongation. This meant re-filleting after many simulations which, in-turn, would perturb the results as the geometrical features of the coupling cell would vary with each simulation.

From this, rather than filleting the corners of the coupling cell, the cross section was extruded around a circular path which varied with the radius of the cavity. Again, this was possible due to the new method of cavity design; extruding cross sections along circular paths in order to parameterise features with respect to the cavity's geometries. This meant that, when optimising the cavity and hence changing its overall radius, the coupling slots and coupling cells would move in proportion to the changes.

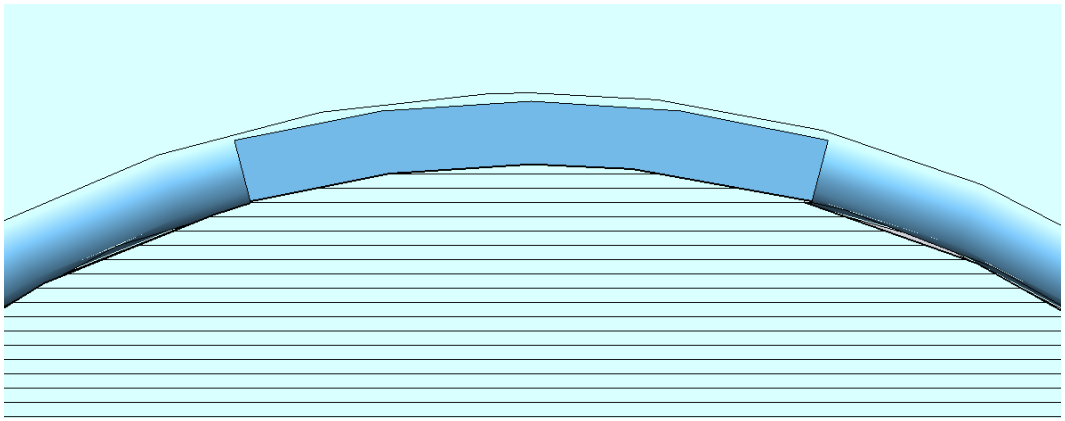

Figure 53 – Coupling Cell that has been Extruded along an Arc

After the new coupling slots had been implemented the cavity was optimised in order to result in a frequency of 3 GHz and a coupling coefficient of 4.4%. Again the iterative process of switching between optimising for the frequency and for K was performed. As before, the overall radii of the accelerating cavity and coupling cells were altered in order to gain an operational frequency of 3 GHz. In order to optimise the cavity to operate with a coupling coefficient of 4.4% a slightly different approach could be adopted when compared with the SCS.

Firstly a simulation was set up in order to assess the coupling coefficient of the annular coupled structure, this time the structure did not have to be mirrored and translated. This is because the faces at the boundaries were the same for the annular coupled structure so periodic boundaries could be applied. For this reason, only the first two modes needed to be simulated for, as the structure consisted of 1 whole accelerating cavity and 2 half coupling cells.

The simulation returned a coupling coefficient of 2.61%. To increase this, the area of the coupling slot needed to be increased. In order to increase the value of K a control parameter 'K_COUPLING' had been set up when implementing the coupling slots. This parameter was linked to the extrusion step. It allowed the angle, and thus the length, through which the coupling vacuum was extruded through, to be controlled. Initially this value was set to 80^0, which meant the coupling slot was extruded through 10^0 of the accelerating cavity from its midpoint. Thus the coupling each of the 8 slots were extruded around 20^0. After an array of simulations, adjusting the radii of both the accelerating cavity and coupling cells to maintain a 3GHz frequency, a 'K_COUPLING' value of 77.7^0 was set.

Following this, the edges could be filleted again in order to reduce magnetic peak fields. Rather than simply adding fillets, the order and size of the filleting was to be experimented with and analytically changed in order to reduce the peak magnetic fields.

2.2.3 Reducing Peak Magnetic Fields

The same procedure as applied to the SCS was applied to the ACS. An array of filleting orders were initially experimented with followed by parametric sweeps of the radii assigned to each blend. The ordering refers to the order in which the edges are selected and filleted.

After optimisation, the peak magnetic field of the operational mode was seen to be 8.307 $NA^{-1}m^{-1}$. Unlike the side coupled structure, a combination of 2 different radius sizes on the coupling slots resulted in the lowest value of the peak magnetic field. Once the magnetic field peaks had been reduced, the structure

was fine tuned and marked as optimal annular coupled structure for the acceleration of protons at 24 MeV.

2.2.4 Optimal Structure Comparison

Following the design, virtual implementation and optimisation of both the side coupled and annular coupled structures, the cavities operational characteristics were compared. The final cavities are displayed in Figure 54 and the key operational characteristics and figures of merit displayed in Table 18.

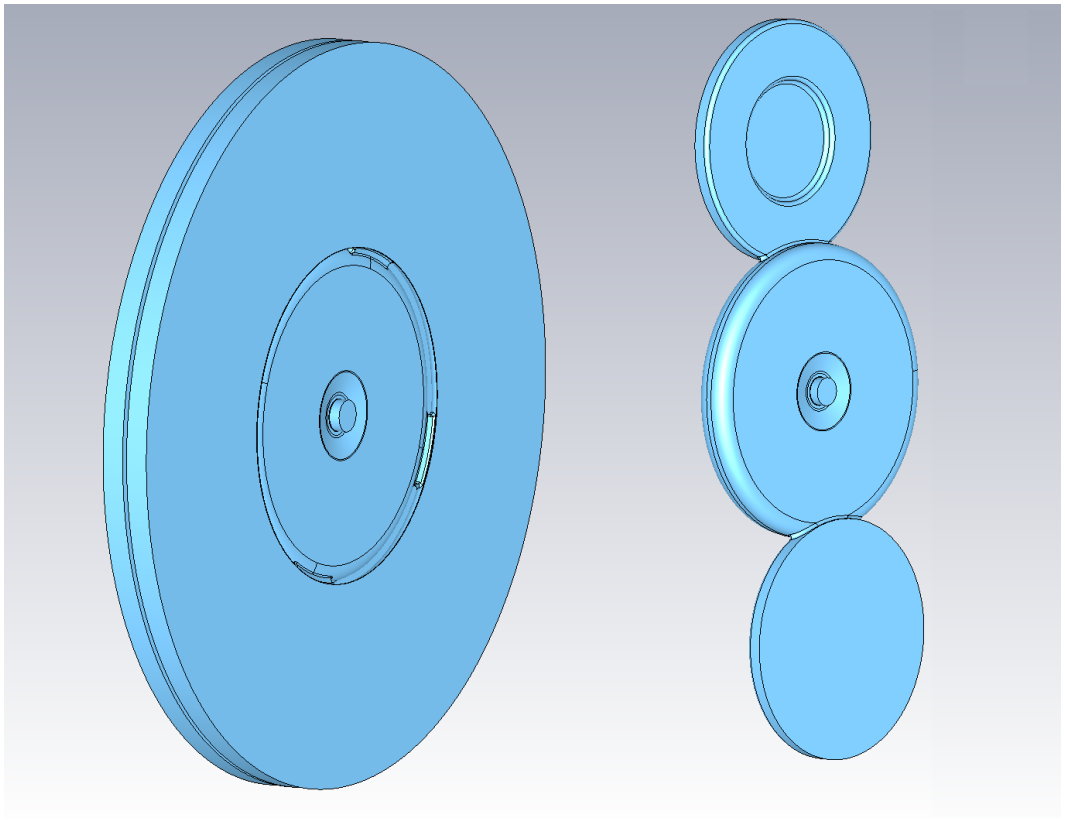

Figure 54 – Final ACS and SCS Designs (Rendered)

Table 18 – Final Comparison of the SCS and ACS Structures

Operational Characteristic	**SCS**	**ACS**
Operational Frequency / GHz	3	3
Coupling Coefficient (K) / %	4.4	4.4
Shunt Impedance / Ohms	242148	228503
Q Factor	5750.15	5489.69
Voltage / V	8.90E+05	8.85E+05
E_{PK} / Vm^{-1}	6.62E+08	6.94E+08
H_{PK} / Am^{-1}	9.42E+05	6.56E+05
MPV	2.47E-02	2.70E-02
Goal Function	1.37	1.47

Analysis of Table 18 shows that, for the operational characteristics concerned with in this project, the ACS does not perform as well as the SCS. It can be seen that the shunt impedance and MPV are worse for the ACS and therefore it possesses a higher goal function. The goal function for both structures is higher than the value of 1.30 optimised for in Section 1.2.1 and this is direct effect of the coupling slot blends. This does not mean however that the cavities are not optimum, the previous value of 1.30 referred to a point where only the nose cones were optimised.

One operational advantage of the ACS however is its lower peak magnetic fields. These peaks can contribute towards field breakdown and so a lower magnitude is preferred. In addition to this, there are also design advantages associated with the ACS structure. During optimisation it was found that the ACS took less time to get the operational frequency and coupling coefficient to the required values. This is because, altering the coupling slots on the ACS had a lesser effect on the overall radius of the cavities than that of the SCS. Furthermore, a structure with one accelerating cavity and two half coupling cells could be used in order to calculate the coupling coefficient; this meant less time simulating as less meshing was required.

To conclude on this section of the project, the ACS is does not perform as well as the SCS. The comparison supports the original research conducted in the literature review section of this project which stated that the shunt impedance is generally lower on annular coupled structures. However, a faster design process along with more control over the coupling coefficient (K) mean that there are inherent advantages of the ACS.

2.2.5 Problem with Optimal ACS Design

Throughout the design of the cavity, the feasibility and manufacturability of the design was discussed with the technicians at Lancaster University. Although the annular coupled structure was the optimal design, the facilities within the department were unable to manufacture a structure of this complexity. The main reason for this was associated with the positioning of the coupling slots. Two problems were

apparent; firstly the blends applied to the slots, although increasing the quality of operation, are difficult to machine with the accuracy required for structures like this. Secondly, it was not possible to drill slots onto the curved section of the accelerating cavity with the CNC lathes in the department. These details were known before the ACS was fully optimised due to frequent conversations held with the technicians at the university. However, it was seen as a goal to have the optimum design available in order to compare the annular coupling slots with the side coupling slots.

However, as the project specification included design, build and test components, a solution to the manufacturing issues needed to be found. Two options were considered. The structure could have been given to an external company who have the facilities in place to use electro-discharge machining (EDM) which would allow the coupling slots to be implemented with the required precision onto the curved section. Secondly, alterations to the design would allow manufacture within the department, still allowing the virtual and physical structures to be compared.

After discussing the options with staff in the department as well as professionals familiar with EDM it was decided that the structure would be altered. This was for two main reasons; firstly, quotes from external engineering companies showed that EDM was a very expensive option and, although the companies agreed to do the process within budget, it would have taken the full £200 which meant there would be a lack of funds for equipment needed in the testing stage. Secondly, as the project was a third year project at university, one of the aims was to learn about how these structures are manufactured and to observe the use of complex machinery. By sending the structure out of the premises to be manufactured, this aspect of the project would be lost.

2.2.6 Solution to the Coupling Slot Location

In order to rectify the problem with the optimal design it was decided that the coupling slots had to be moved to the flat face of the accelerating cavity. This meant that the coupling cells had to be redesigned

in order to allow a coupling slot to connect with the flat face of the accelerating cavity. The new coupling cell design can be seen in Figure 55.

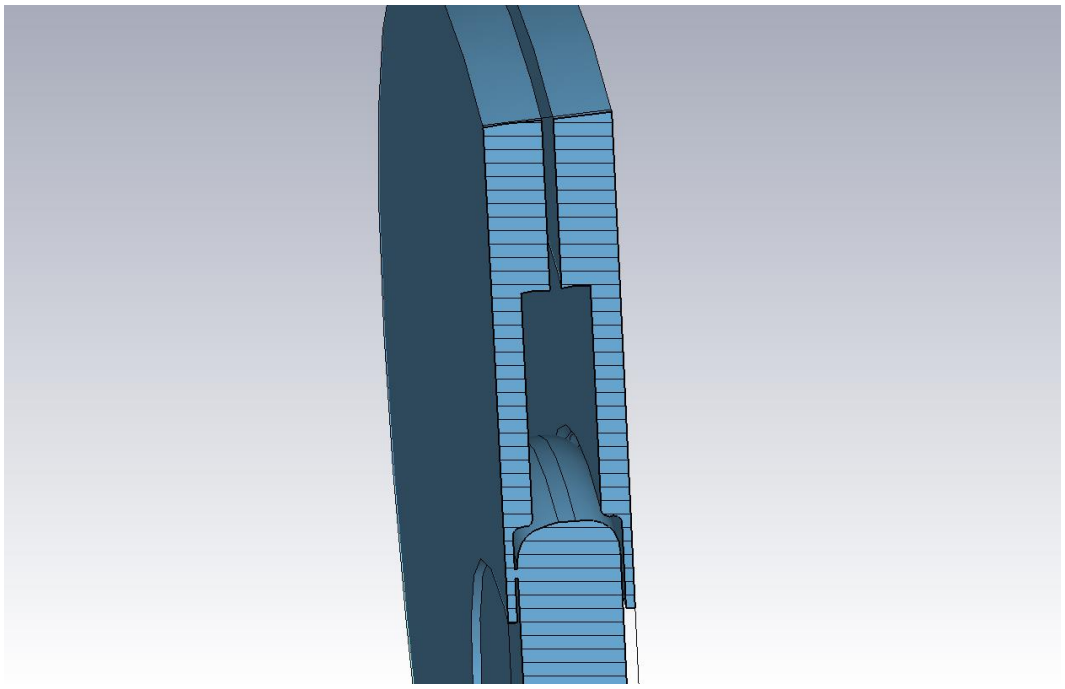

Figure 55 - New ACS Coupling Design

It can be seen that the new coupling slot was a cylinder, Figure 56. Initially this was seen as the best option as it meant that the coupling slots could simply be drilled out. However, it was then realised that in order to increase the coupling coefficient, the holes would have to be increased in diameter and this could mean, for high coupling, the cylinder diameters would leave the accelerating cavity. A similar problem to this has already been detailed in Section 2.2.1 and due to this, a similar approach was adopted in the solution. A coupling slot which was extruded through an arc was designed. Fortunately, the difficult procedure of creating an arc which varied with the cavity's radius had already been done for the last coupling slot. The arc location was altered slightly and the resulting coupling slot is shown in Figure 57.

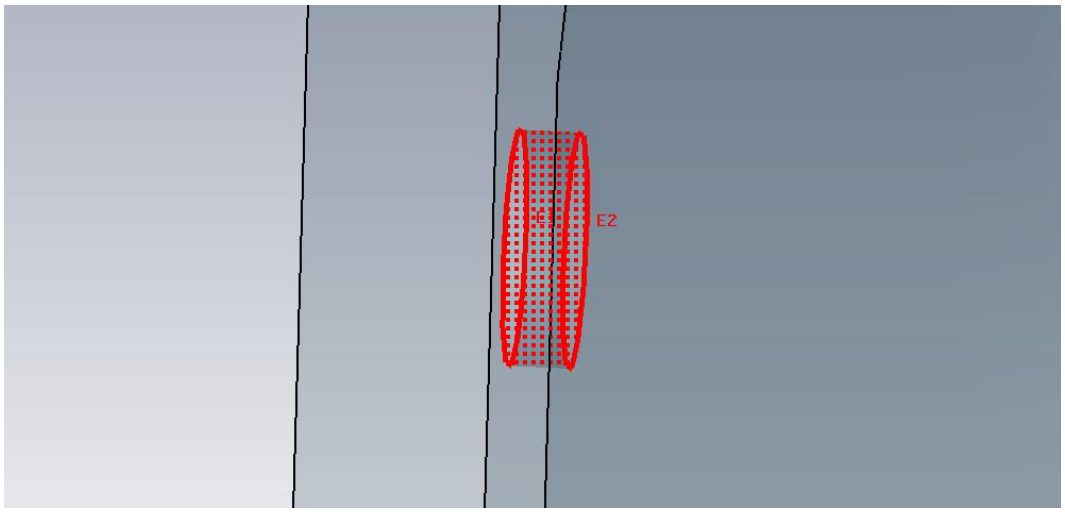

Figure 56 – Cylindrical Coupling Slot – On Flat Face of Accelerating Cavity

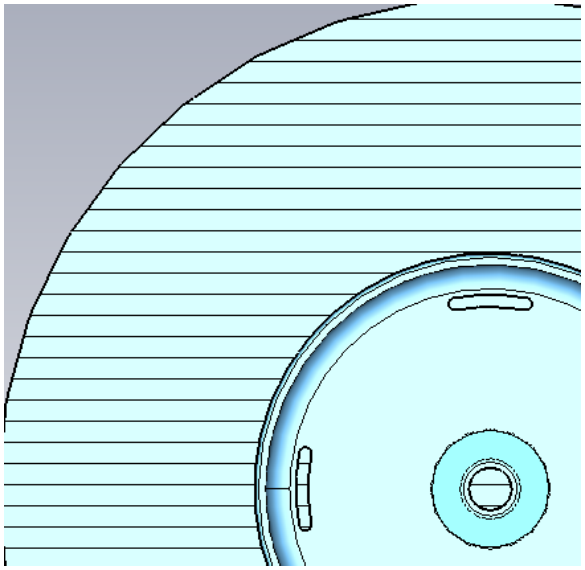

Figure 57 – Extruded Coupling Slot – On Flat Face of Accelerating Cavity

The coupling slots were rounded in order to reduce peak fields and this completed the amended design in order to allow manufacture within the department. After confirming the feasibility of the design features with CNC technicians, optimisation was needed in order to result in a final structure to be built.

As before, parameter sweeps were firstly conducted in order to get the accelerating and coupling modes to operate at 3 GHz. Following this, another parameter sweep which altered the coupling control parameter, 'K_COUPLING', was carried out until a coupling coefficient of 4.4% was arrived at. The

operational frequencies were then checked and the cavity was altered to return these to 3 GHz. The process was repeated until both accelerating and coupling modes had the correct frequency and the coupling coefficient equalled 4.4%.

2.3 Full Structure Simulations

Following the alteration of the optimal design in order to allow manufacture, a full structure simulation was required. Referring back to the idea that only part of the cavities were simulated, the smallest repeating units, the whole structure to be built would consist of an array of these structures. Ideally a large array of the designed sections would be implemented, however, due to the cost to build the large structure necessary to house this large cavity as well as the amount of time it would take a technician to build this, a smaller structure needed to be built. The array shown in Figure 58 was chosen as a large enough structure to test, but small enough to allow the material used to be within budget as well as to allow the technician enough time to build the structure.

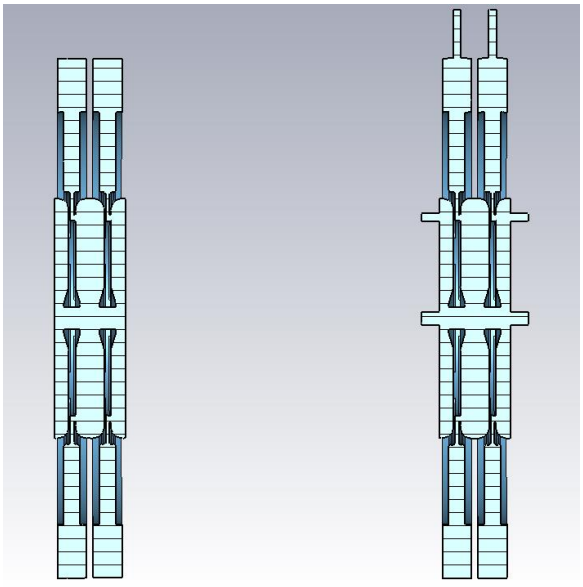

Figure 58 – Final ACS Cavity Structure to be Built and Tested

***LEFT:** Final ACS **RIGHT:** Final ACS with Coax and End Plate Holes for Testing*

Following this the coaxial inputs as well as the holes on the endplates, used to short the structure, needed to be accounted for. This is because, although not ideal, they alter the shape of the designed vacuum and so the frequency and coupling coefficient alter with their presence. In order to increase the similarity of the simulated and tested results, the cavity radius and coupling slots were altered until the frequency of the operational mode along with the coupling coefficient of the structure were at 3 GHz and 4.4% respectively.

Following these alterations, the designed structure was confirmed with the academic supervisor for this project, Dr Graeme Burt, and deemed at a stage were the build stage of this project could be started.

CHAPTER 3 – BUILD

In order to build the linear accelerator section, the metal which the cavity would be housed needed to be designed. In order to make manufacture possible, the structure needed to be made from a series of discs. The best method of doing this was seen to separate the cavity into 6 sections; 4 sections would house the cavity the other 2 represented the end plates which close the structure and house coaxial inputs into the two half accelerating cavities.

1 Design in CST MWS

The cavity was firstly split into six different sections and saved as six separate files. Following this, cylinders were drawn, one per file, which overlaid the corresponding cavity system. The cavity section could then be subtracted from the cylinders to create the metal discs, Figure 59.

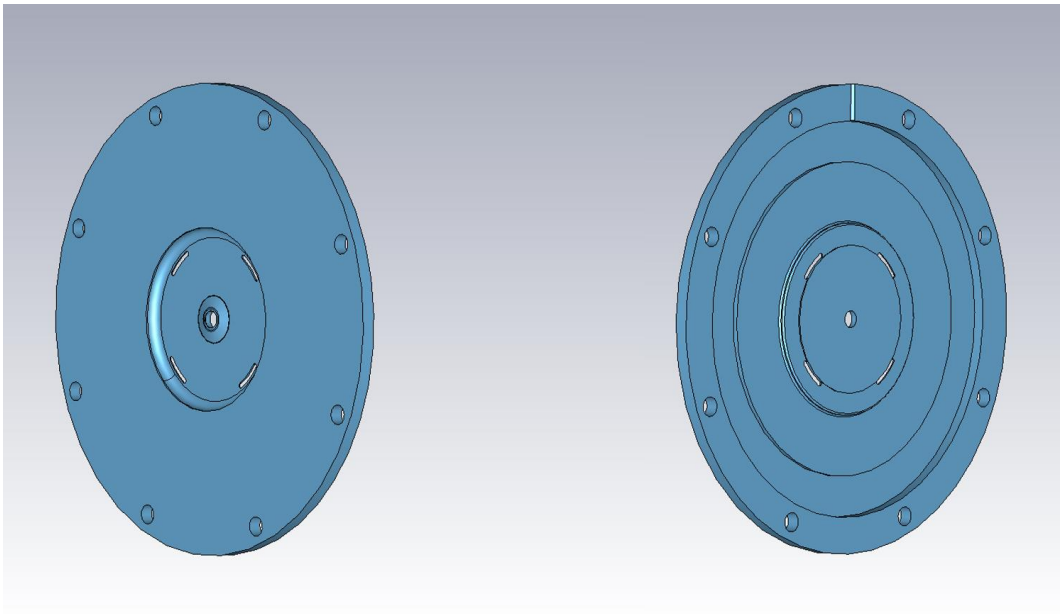

Figure 59 – One of the 4 Cavity Housing Discs (2 Views)

The figure also shows the 8 M8 holes which are necessary to clamp the discs together. These holes were not part of the simulation. This is because they do not intersect with any part of the cavity system. The reason 8 holes were chosen was to allow a tight seal to be established. However, it also had an advantage that the 4 discs could consist of 2 pairs of identical discs that could simply be rotated by the 45^0 that corresponded to the coupling slot orientation.

One of the main conclusions drawn from this project was that, for large arrays of cavities. The annular coupled structure has an inherent advantage in terms of manufacturing simplicity. Furthermore, realising that manufacture is never a perfect process, the discs can be arranged in different places to realise the best operational characteristics.

2 Design in SolidWorks

In order to present the discs to the CNC engineer, Jonathan Gates, they needed to be implemented in CAD software. The chosen CAD package to do this was SolidWorks and the disc shown in Figure 59 can be seen implemented in SolidWorks in Figure 60.

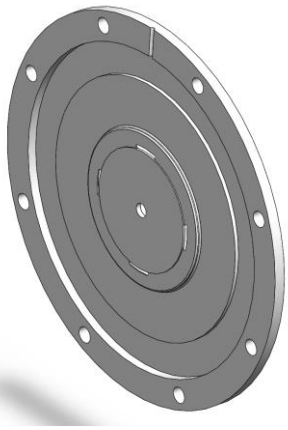

Figure 60 - One of the 4 Cavity Housing Discs

After the 6 discs had been implemented, they were saved and implemented as an assembly. The assembly as a whole and a cross section can be seen in Figure 61.

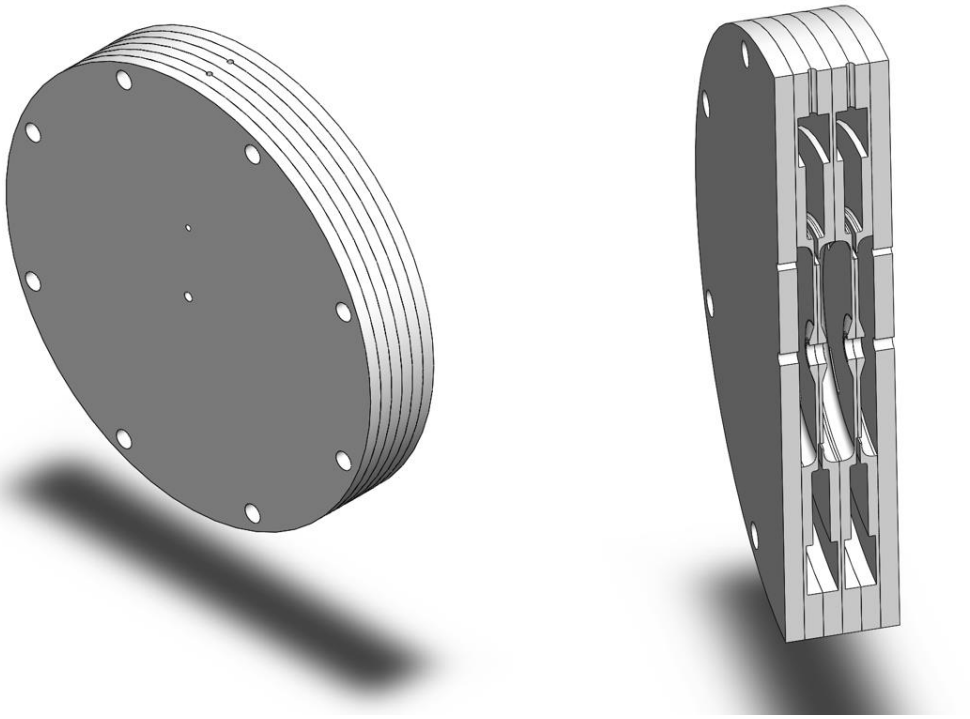

Figure 61 – Array of Metal Discs which Houses the Cavity Section

***LEFT**: Isometric View* ***RIGHT:** Cross Sectional View*

After completing the design, the need for drawing sheets was discussed with the technician. It was decided that for a build of this complexity, it was easier for the technician if the Solidworks file was sent

rather than a vast array of drawing sheets. For this reason, each disc to be constructed was sent in addition to the assembly file in order to allow the technician to fully understand how the discs are assembled in order to house the designed cavity.

3 Manufacture Materials and Method

The material used to manufacture the discs from needed to be decided upon. From literature and advise from professionals in the field, it was made clear that copper was the best choice. This is because of the materials conductive properties and ability to hold a vacuum. However it was decided that, for this project, copper was unsuitable. Firstly copper is very expensive and the £200 budget for this project made buying a suitable amount unfeasible. Secondly, the machining properties of copper are poor compared to other metals. When cutting into copper using a lathe, the metal can stick the cutting piece meaning inaccurate dimensions and poor surface quality.

After speaking to technicians, it was clear that for machining using equipment available in the department, aluminium was the best choice. The type of aluminium chosen was 6082; this was due to its high strength, good resistance to corrosion and its relative ease to machine on a CNC lathe. The elemental composition and properties of this material are displayed in Figure 62.

BS EN 573-3:2009 Alloy 6082	
Element	% Present
Silicon (Si)	0.70 - 1.30
Magnesium (Mg)	0.60 - 1.20
Manganese (Mn)	0.40 - 1.00
Iron (Fe)	0.0 - 0.50
Chromium (Cr)	0.0 - 0.25
Zinc (Zn)	0.0 - 0.20
Others (Total)	0.0 - 0.15
Titanium (Ti)	0.0 - 0.10
Copper (Cu)	0.0 - 0.10
Other (Each)	0.0 - 0.05
Aluminium (Al)	Balance

Property	Value
Density	2.70 g/cm³
Melting Point	555 °C
Thermal Expansion	24 $x10^{-6}$ /K
Modulus of Elasticity	70 GPa
Thermal Conductivity	180 W/m.K
Electrical Resistivity	0.038 $x10^{-6}$ Ω .m

Figure 62 – Elemental Composition and Properties of Al 6082

(Extracted from Aalco's Material Database)

Following the choice of material, the manufacturing method needed to be decided upon. After analysing the equipment available in the department, it was clear that the best option was to cut cylinders from aluminium bulk and use subtractive manufacture in order to create discs. The machine used for the latter was a computerised numerical control (CNC) lathe.

4 Final Structure

Timing the manufacture to coincide with exam period at Lancaster University meant no project time was wasted waiting for the discs to be manufactured. After the 5 weeks, with regular check ups and conversations with technicians about technical features, the 6 discs were manufactured and the final structure can be seen in Figure 63.

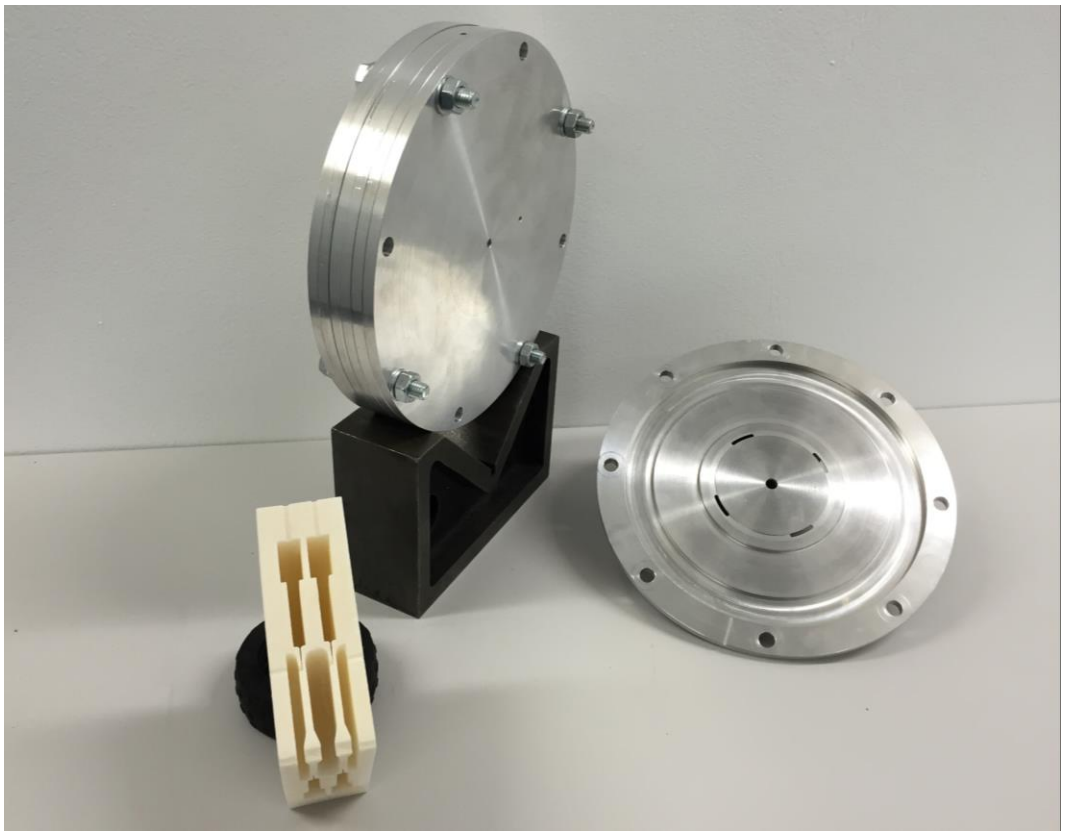

Figure 63 – Final Structure

Prototyped Cross Section, Final Structure and Example of Aluminium Disc

The photograph shows the final structure along with an example aluminium disc and a rapid prototyped quarter cross section. The example disc contained a manufacturing error but was kept in order to represent what the discs looked like inside the structure. The quarter cross section was made using additive manufacture on a selective laser melting (SLM) machine. The cross section was manufactured due to interest in the project from peers and professionals in the field; it allowed the inside geometries to be accurately displayed when describing the way in which the structure works.

CHAPTER 4 – TEST

1 Cavity Testing Theory

Although the cavity was designed to accelerate a beam of protons, obtaining and using a proton source to analyse the structure was seen to be unfeasible. Instead, the field inside the cavity was to be analysed using RF field measurements.

The technique adopted to carry out the measurements is known as the Bead-Pull [37] method and allows the field distribution within the cavity to be analysed and evaluated. To carry out the measurements using this method, a small perturbing object, i.e. a bead, is pulled through the cavity in a smooth, controlled fashion. At the same time, a vector network analyser (VNA) is required to take RF measurements.

The method utilises Slater's Theory, Equation (56). The theory allows a relationship between the perturbing object, the bead, and the resonant frequency shift to be established.

$$\frac{\omega^2 - {\omega_0}^2}{{\omega_0}^2} = k \int_{\Delta r} \frac{\mu H^2 - \epsilon E^2}{2U} dv \tag{56}$$

Where: ω = New ResonantFrequency / Hz

ω_0 = Origional Resonant Frequency / Hz

k = Constant Dependant on the Bead's Shape

μ = Pearmeability Constant / $\mathrm{NA^{-1}}$

H = Magnetic Field Amplitude / $\mathrm{Am^{-1}}$

ϵ = Permittivity Constant / $\mathrm{Fm^{-1}}$

E = Electric Field Amplitude / $\mathrm{Vm^{-1}}$

U = Energy Stored in th Cavity / J

As discussed in the literature review, the transverse magnetic mode (TM mode) of acceleration used means that a longitudinal electric field component exists along the beam axis. Here, the magnetic field has zero magnitude; hence the electric field is proportional, and controlled by, the resonant frequency. Therefore, the Bead-Pull technique uses Slater's Theory to measure the change in resonant frequency which allows the electric field long the cavity's central axis to be deduced.

2 Designing the Testing Set-Up

In order to test the structure, using the Bead-Pull theory discussed in the previous section, a testing setup had to be designed and built. As a field perturbing object was to be carried through the structure by a piece of thread, an arrangement of pulleys had to be designed which would allow the thread to be held under tension and pulled through the cavity.

Following this, a method of pulling the thread needed to be established. Although it was possible to pull the thread by hand and measure the distance pulled using precise techniques such as interferometry, it is impossible to provide smooth motion or precise small increments. A technique needed to be devised which would allow this precision and give controllable increments in the length which the perturbing object was pulled. Thus, a better method was to incorporate controlled stepper motor system.

2.1 Pulley System

Initially the structure shown in Figure 64, simply implemented in SolidWorks for reference, was considered as a housing for the pulley system. The bead holding thread would be weighted and held by the three pulleys and the stepper motor would pull the bead through, from the right, at a position in line with the beam axis.

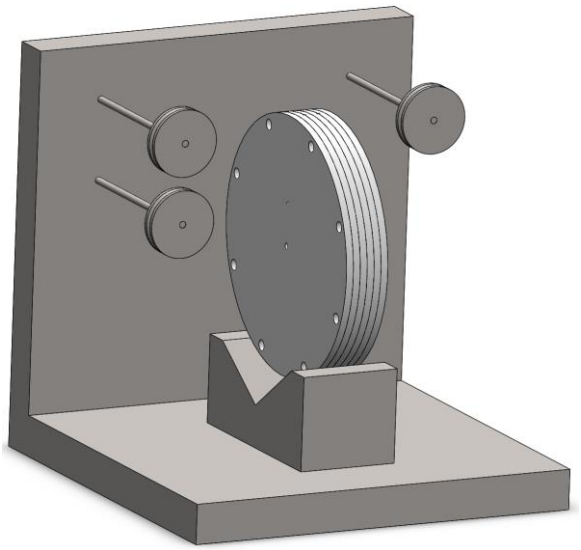

Figure 64 – Initial Pulley Design

A disadvantage of this system was the fact that the pulley arms were only fastened at one end. The pulley arms would deflect under tension, making the thread harder to align with the beam axis and could incur transverse oscillations with bead movement.

Instead a structure which used 'H-shaped' constructions made from angled sections of steel was designed and a prototyped proof-of-principle structure is displayed in Figure 65.

Note, although the discs were too complex to manufacture without the aid of the technicians, all the necessary skills were possessed which allowed every aspect of the testing setup to be built without help from technicians.

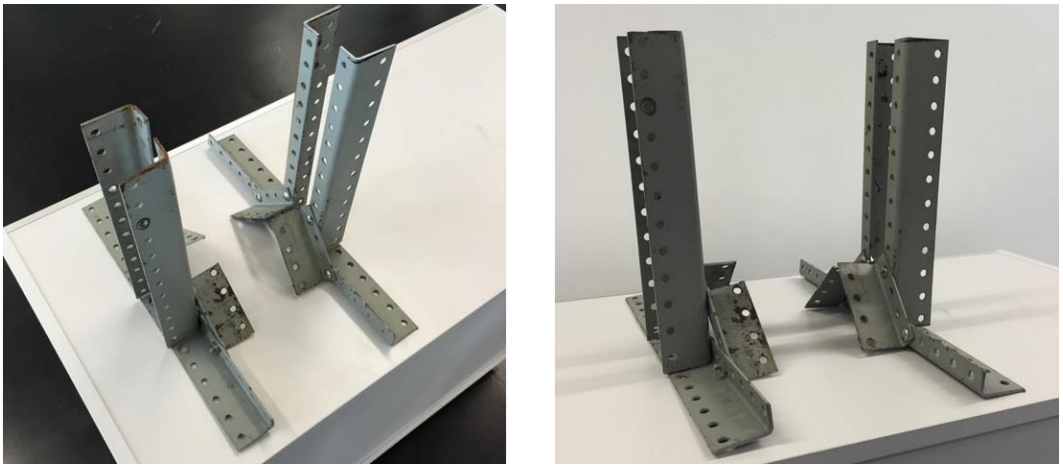

Figure 65 – Initial Pulley Frame (Prototype)

The prototype had an array of holes which would allow the height of the pulleys to be varied. However, due to the precision needed when positioning the pulleys, it was decided that for the final structure, the exact position needed would be drilled in order to align the thread exactly with the cavity's aperture.

A final structure was then made from stronger angled steel which, unlike the material used in Figure 65, was new, unbent and with no areas of corrosion. The stronger steel meant less vibrations would be observed which could distort the RF measurements. The final structure, tapped into a thick steel base, can be seen in Figure 66. Sections of threaded bar were used for the pulley arms which allowed them to be tightly secured to the structure, also allowing the variable positioning of each pulley.

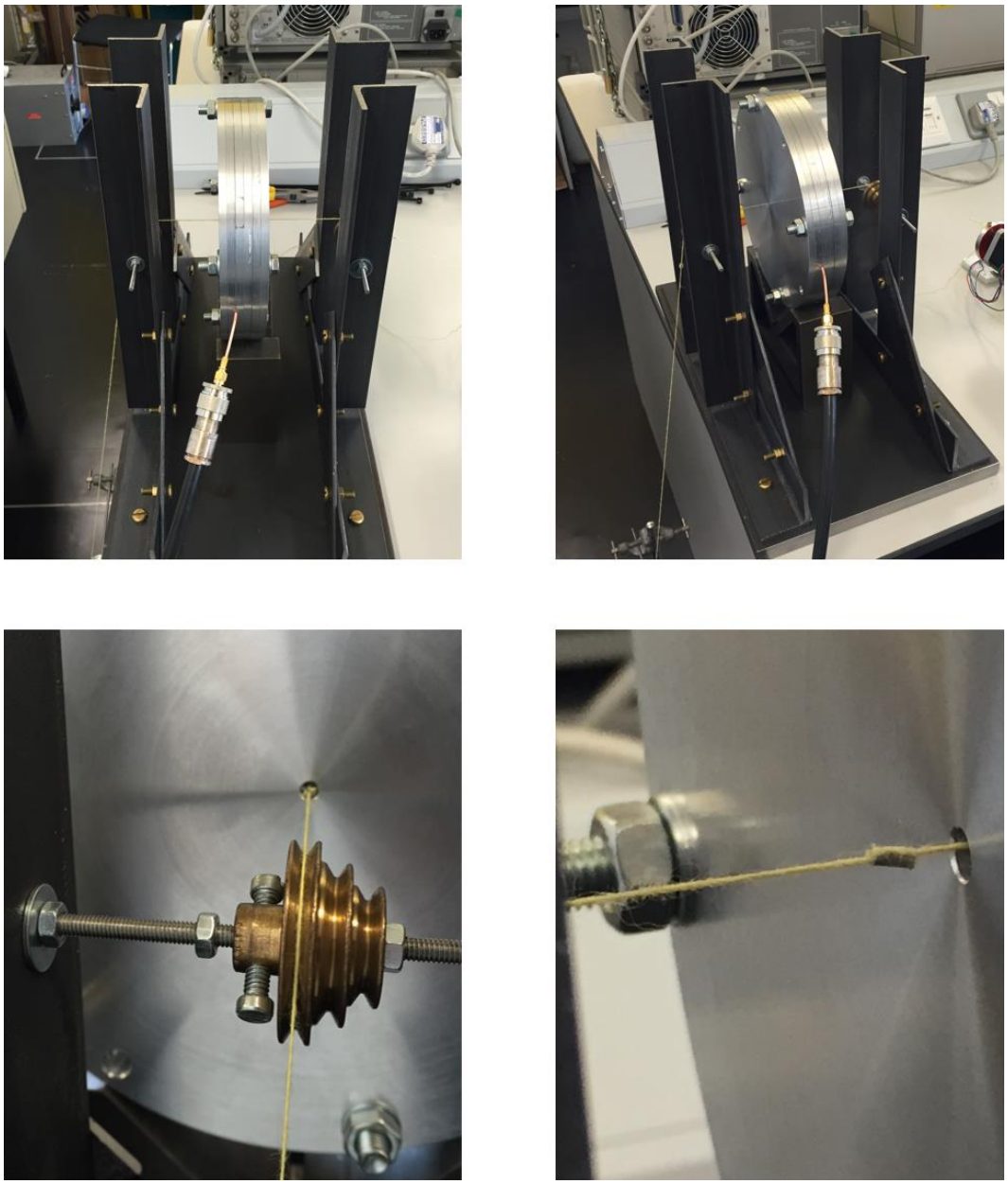

Figure 66 – Final Bead-Pull System

The 4 images show the pulley system with the thread kept under tension by attaching a weight to the end of the thread which, with the use of a third pulley, hung over the edge of the desk on which the system resided. Kevlar thread was used in order to minimise elongation effects due to the weighted end and the perturbing object used was a small section of capillary tub. This was chosen firstly because it is metallic, meaning a substantial effect on the field could be observed. Secondly, capillary tube is hollow, which allowed it to be easily threaded onto the Kevlar thread.

2.2 Stepper Motor Set-Up

In order to provide controlled propagation of the perturbing object an integrated stepper motor control system needed to be designed. In order to control the stepper motor, a microcontroller was used. The microcontroller chosen was the Arduino Uno due to previous experience with the product and its programming language.

The stepper motor chosen was a toothed pole motor. This type of motor allows for small precise increments and the particular motor used had 200 steps per revolution, meaning individual steps of 1.8^0. In order to interface this motor with the microcontroller, a stepper motor driver board was needed. The driver used was the 'Black Edition A4988 Stepper Motor Driver Carrier'. The schematic for implementation along with the actual set-up is displayed in Figure 67.

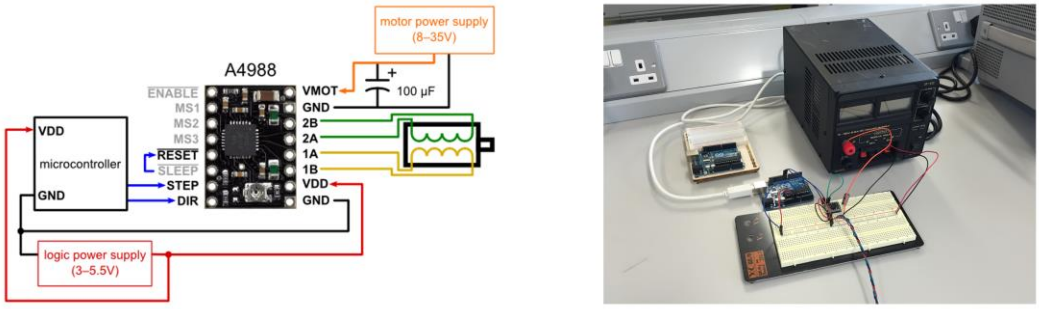

Figure 67 – Stepper Motor Control Set-Up

***LEFT**: Wiring Schematic* ***RIGHT:** Actual Set-Up*

Before writing a code which would allow control over the stepper motor, a masters (MENg) level engineering additive manufacturing group were consulted. This was because the group had a lot of experience with the large stepper motors used in the 3D printing subsection of additive manufacturing equipment. They suggested downloading a library which contained a vast array of pre-set commands specifically written to allow control over one or more stepper motors using an Arduino microcontroller. The group explained their code and specifically the commands they had used from the downloaded library.

Thus, the Arduino programming software and the stepper motor library (AccelStepper) was firstly downloaded. Then, using the commands available in the library, as they were proven to provide accurate stepper motor control, a code for the control of one motor's speed, acceleration and distance was written. This code, annotated to describe each step, can be seen in Figure 68.

```
#include <AccelStepper.h>                    //Refer to the downloaded stepper motor library

// Fast axis - Move to a set position at a set speed and acceleration

AccelStepper Fastaxis(1, 8, 9);              // Assign Arduino Pins and use of driver board via 1 input
int posl = posl;                             // Set the initial position

void setup()
{
        Fastaxis.setMaxSpeed(10);            // Set the speed
        Fastaxis.setAcceleration(10);        // Set the acceleration
        Fastaxis.moveTo(150);                // Set the number of steps
}

void loop()                                  // Run the program
{                                            // IF THE MOTOR NEEDS TO REVERSE BACK TO THE ORIGIONAL POSITION*
//      if (Fastaxis.distanceToGo() == 0)              // *Determine when fast axis has achieved its desired displacement
//              {
//              posl = -posl;                          // *Assigns the positive pos to become negative
//              Fastaxis.moveTo(posl);                 // *Makes the fast axis run in reverse
//              }
        Fastaxis.run();                      // Enables the fast axis to physically run
```

Figure 68 – Arduino Code Used to Control Stepper Motor

Once the code had been uploaded to the Arduino and the motor connected to the driver system, the stepper motor could be driven by a set amount of steps, in any direction, at the push of a button.

Finally a pulley was drilled and tapped to allow a screw to be placed on its circumference, and this pulley was attached to the motor's revolving axis. This enabled the Kevlar thread to be connected to the stepper motor. The calculations carried out to work out the distance the bead would be pulled per step are displayed below.

$$Cricumference = \pi d = \pi \times 48 = 150.796\ mm\ (3\ Decimal\ Places)$$

$$\therefore Each\ Step = \frac{150.796}{200} = 0.754\ mm\ (3\ Decimal\ Places)$$

The number of steps was set to 150. This corresponded to a length of 113 mm (3SF) and this was more than enough to ensure the bead would travel through the entirety of the cavity, but was not too long as to waste time.

3 Results and Measurement Technique

After the testing set-up was completed, the cavity was plugged into a vector network analyser (VNA) using the RG405 semi-rigid coaxial cable, soldered to SMA adapters, for which the coax slots were designed for. The end of the coaxial cable which was plugged into the cavity was stripped to the inner conductor and the inner conductor was formed into a loop for a better measurement.

Firstly the VNA was calibrated using the calibration kit. The RG405 was placed in each of the 4 coax holes and the VNA displayed the clearest output when one of the coupling cell holes was used. For this reason the coax was kept in this position throughout the system. The amplitude was then measured and several peaks were observed. The resulting graph was saved as a '.s1p' and '.csv' files. The data was formatted into a graph and this can be seen in Figure 69.

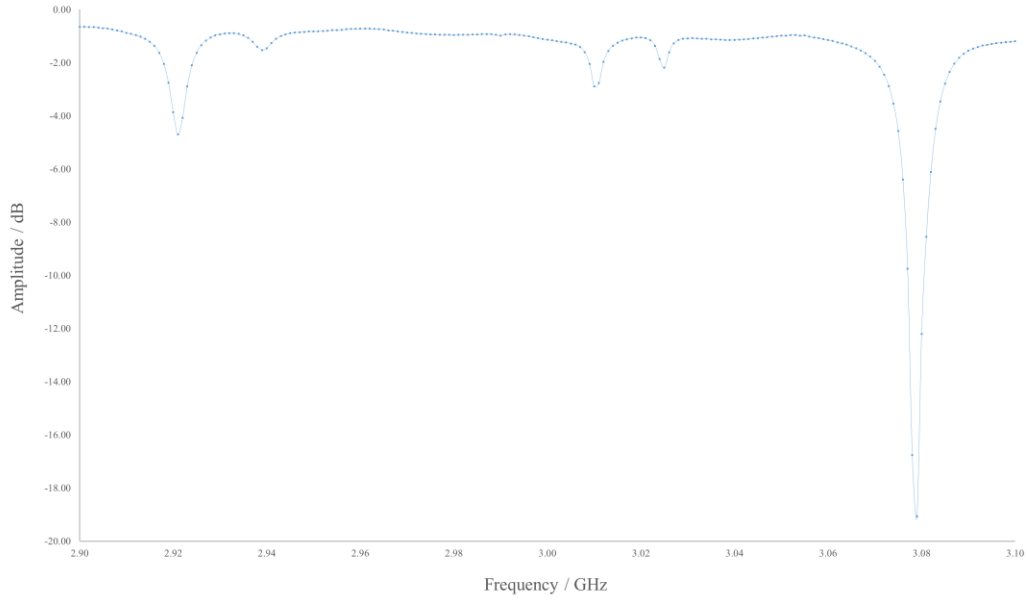

Figure 69 – Initial Magnitude against Frequency Plot

The VNA displayed 5 clear peaks which corresponded to 5 resonant modes; this was as expected as the cavity had 5 cells. The frequencies of the 5 modes are presented in Table 19.

Table 19 – Mode Frequencies

Mode Left to Right on Figure 69	Frequency / GHz (4SF)
1	2.921
2	2.939
3	3.010
4	3.025
5	3.079

The VNA was then set at the frequency of the first mode. A centre of 2.921 GHz was selected with no span; in reality the VNA had to use a 2 Hz span, but this is negligible and would still represent the correct mode. The VNA was then set to measure phase rather than amplitude and the Bead-Pull was triggered, plotting the phase variation. This was done for each of the 5 modes and the results for the mode at 2.921 GHz can be seen in Figure 70.

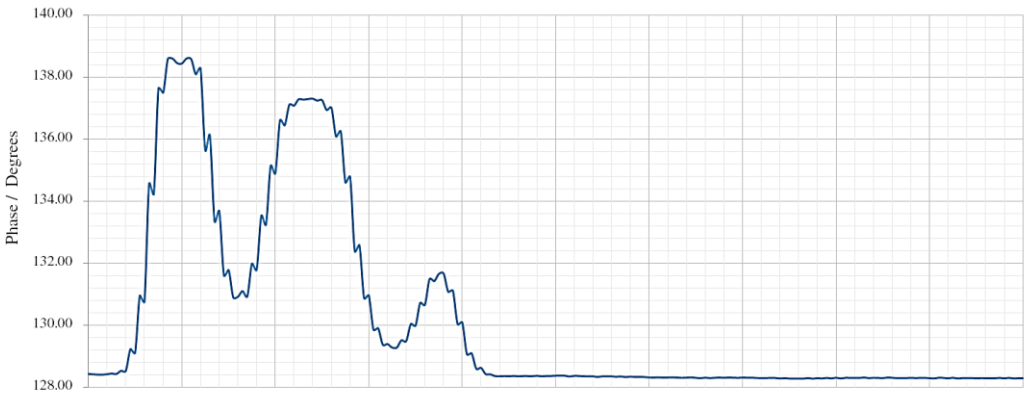

Figure 70 – Analysis of the Phase Variation with Bead Propagation (Mode 1)

From the outputted data it was clear that the Bead-Pull measurement system had been successful. This is because the phase was successfully perturbed from a constant value in the cavity and returned to its original phase after the bead had left. Not only this, but the perturbations aligned with the positions of the nose cones inside the cavity.

Bead-Pull measurements of modes 2-5 were then carried out and the graphs corresponding to these measurements are shown in Figure 71.

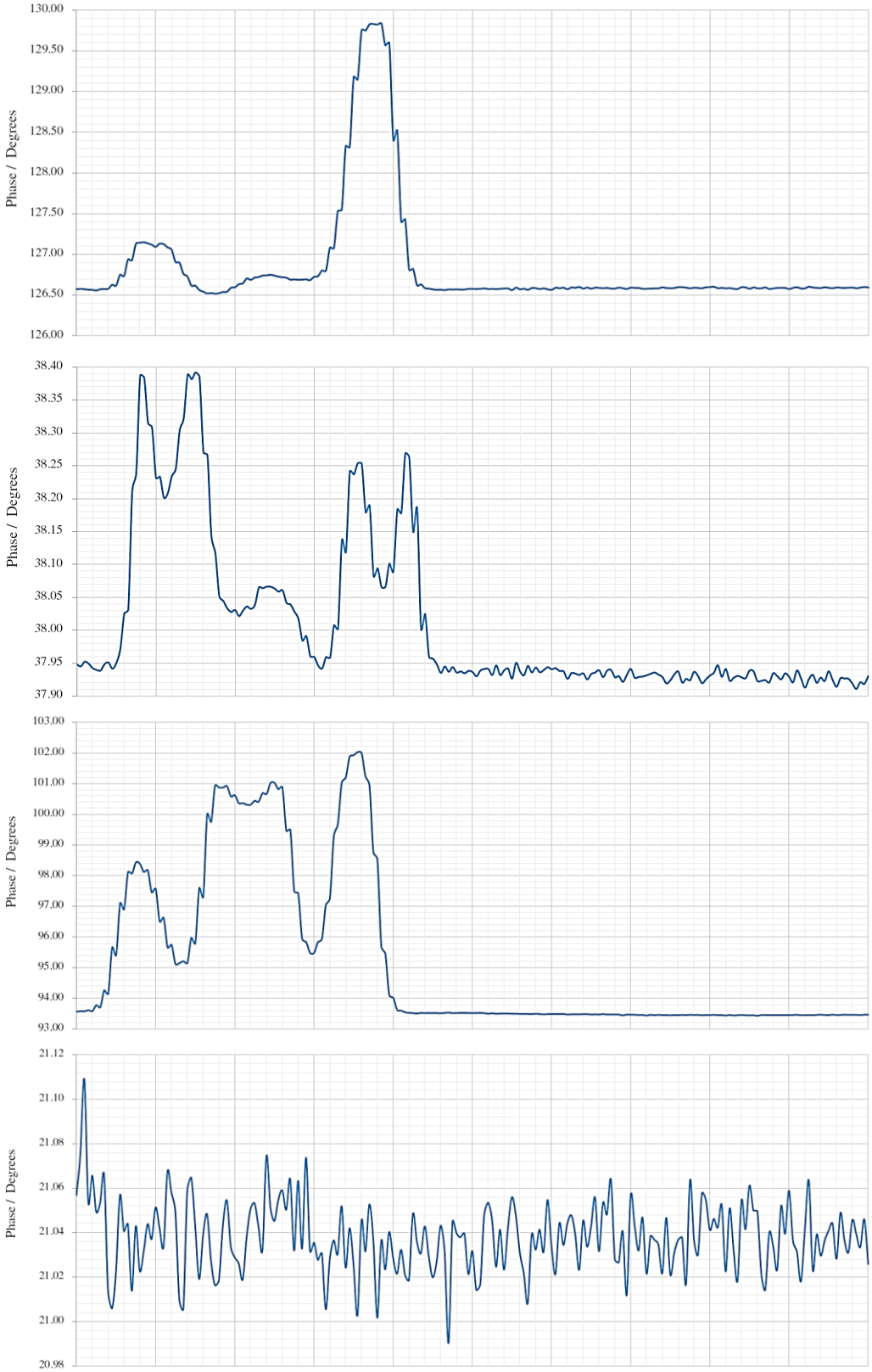

Figure 71 – Bead Pull Measurements for Modes 2-5 Respectively

The resultant graphs for modes 2-4 are similar to the one which represents mode 1; by which the phase perturbations are clear peaks which correspond to interior features of the structure. Mode 5, 3.079 GHz, shows very little phase change and only the presence of noise is visible. The graph shows that the phase varies by a maximum of 0.12° throughout the measurement.

The reason this mode undergoes no perturbation is because the mode only exits in the coupling cells. This means that, although there is a mode present, the bead has no field to perturb as the bead was pulled through the accelerating cavities.

4 Converting the Results in Order for Comparison with CST MWS

In order to compare the results with those outputted from CST MWS, the data had to be converted into field rather than phase. This involved a series of complex calculations which were applied to the experimentally gained phase data (S11 data). The equation utilised for this conversion was the Slater and Maier equation [38]:

$$\frac{\delta\omega}{\omega_0} = -\frac{3E^2\varepsilon_0 dv}{4U} \tag{57}$$

$$\frac{\delta\omega}{\omega_0} = \delta \tag{58}$$

Where: E = Electric Field / Vm^{-1}

ε_0 = Permittivity of Free Space / Fm^{-1}

dv = Relative Volume of the Purturbing Object / m^3

U = Total Energy / J

In order to calculate δ from the phase, the following equation was used [39]:

$$\angle S_{11} = \frac{\pi}{2} - \tan^{-1}(Q_L \delta) \tag{59}$$

$$\delta = \frac{\tan\left(\frac{\pi}{2} - \angle S_{11}\right)}{Q_L} \tag{60}$$

Where: $\angle S_{11}$ = Phase Measurement / Degrees

Q_L = Q Factor

Before any calculations were conducted, the phase was converted to radians and normalised so the phase change rather than its magnitude was being used in the calculations. The value of Q_L then needed to be calculated, Equation (59), from the initial magnitude plot which displayed each of the 5 mode's frequencies. Finally, Equation (60) was used to calculate δ and the resultant graphs for modes 1-4, since the 5th mode had no perturbation, are displayed in Figure 72.

$$Q_L = \frac{f_1 - f_2}{f_0} \tag{61}$$

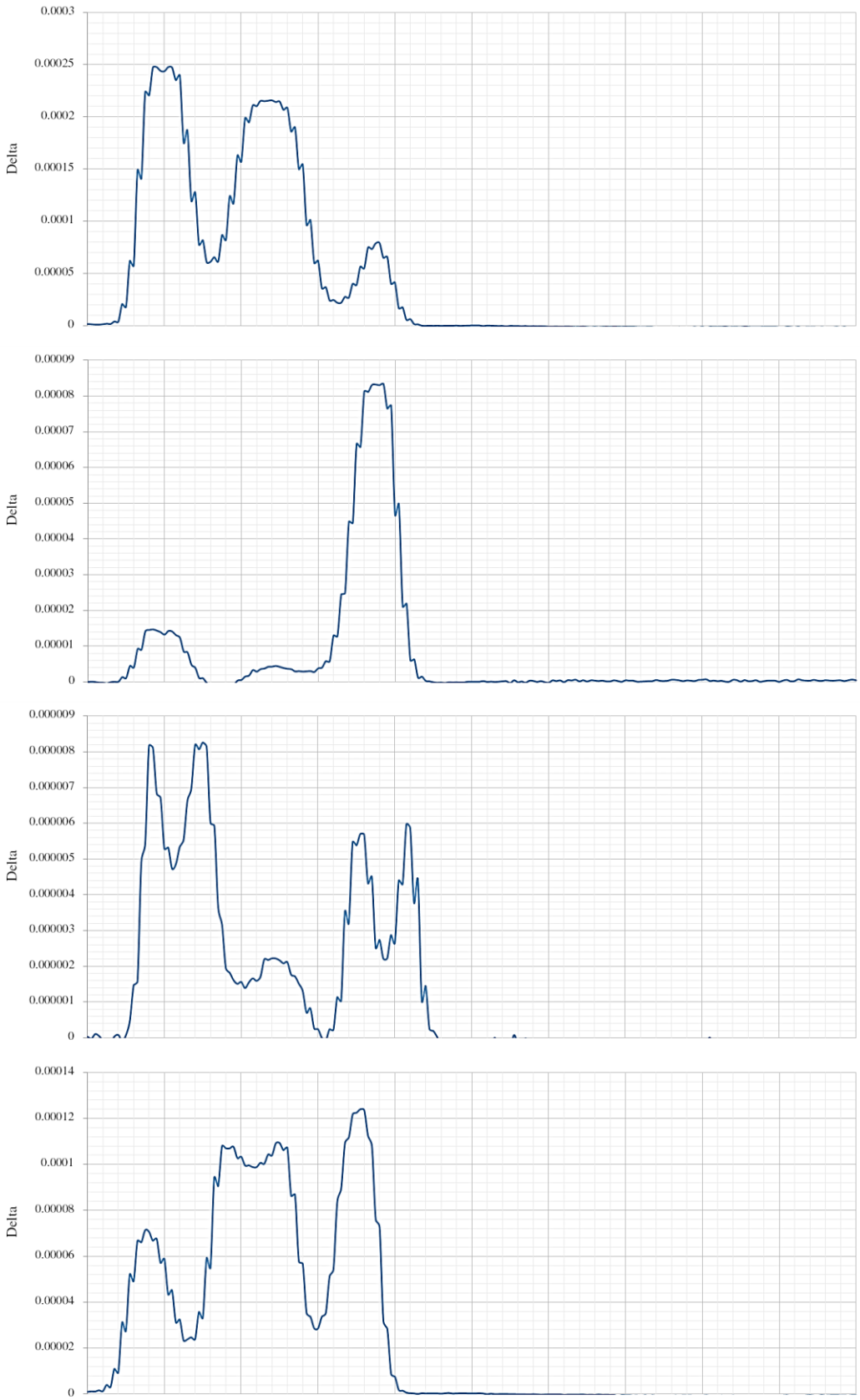

Figure 72 – Value of δ for Modes 1-4

Following the δ calculation, the electric field per unit energy needed to be calculated. Equation (57) was manipulated to give:

$$\frac{E^2}{U} = -\frac{4\delta}{3\varepsilon_0 dv} \tag{62}$$

The only variable left in order to use Equation (62) was the volume of the perturbing bead. A representation of the bead can be seen in Figure 73.

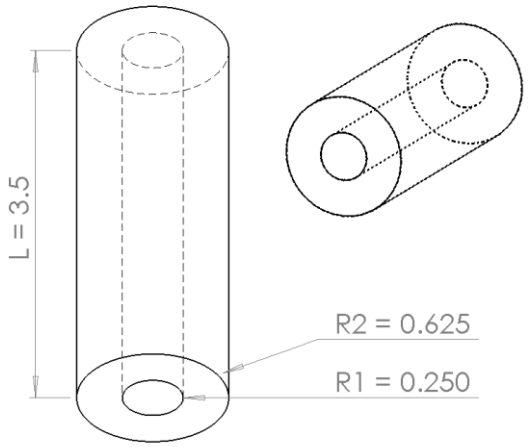

Figure 73 – Bead Dimensions (mm)

$$\pi\left(r_2{}^2 - r_1{}^2\right)l = \pi \times \left(0.625^2 - 0.250^2\right) \times 3.5 = 3.61\ mm^2 = 3.61 \times 10^{-9}\ m^2$$

Following the calculation of the bead volume, the electric field per unit energy could be calculated using Equation (62). The resultant graphs, again for modes 1-4 are displayed in Figure 74.

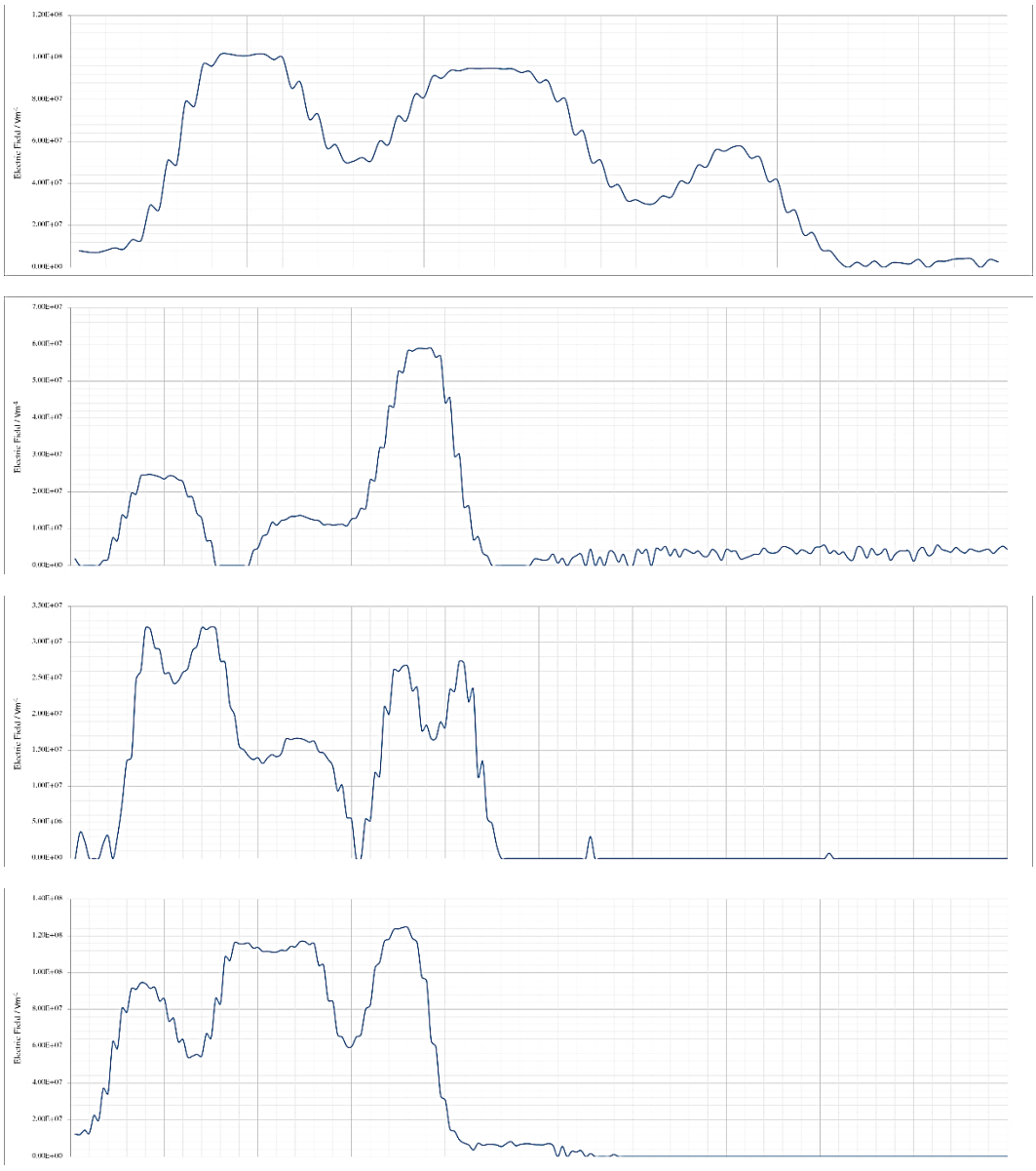

Figure 74 – Electric Field along the Beam Axis (After Converting the Measured Data)

5 Comparing the Measured and Converted Data with Data Outputted from CST MWS

The electric field along the axis of the structure needed to be simulated for in order to see whether the modes measured and displayed in Figure 74 were the same as the modes present for the virtual structure. Thus, E_z along the axis of the structure was simulated for and the resultant modes are displayed in Figure 75.

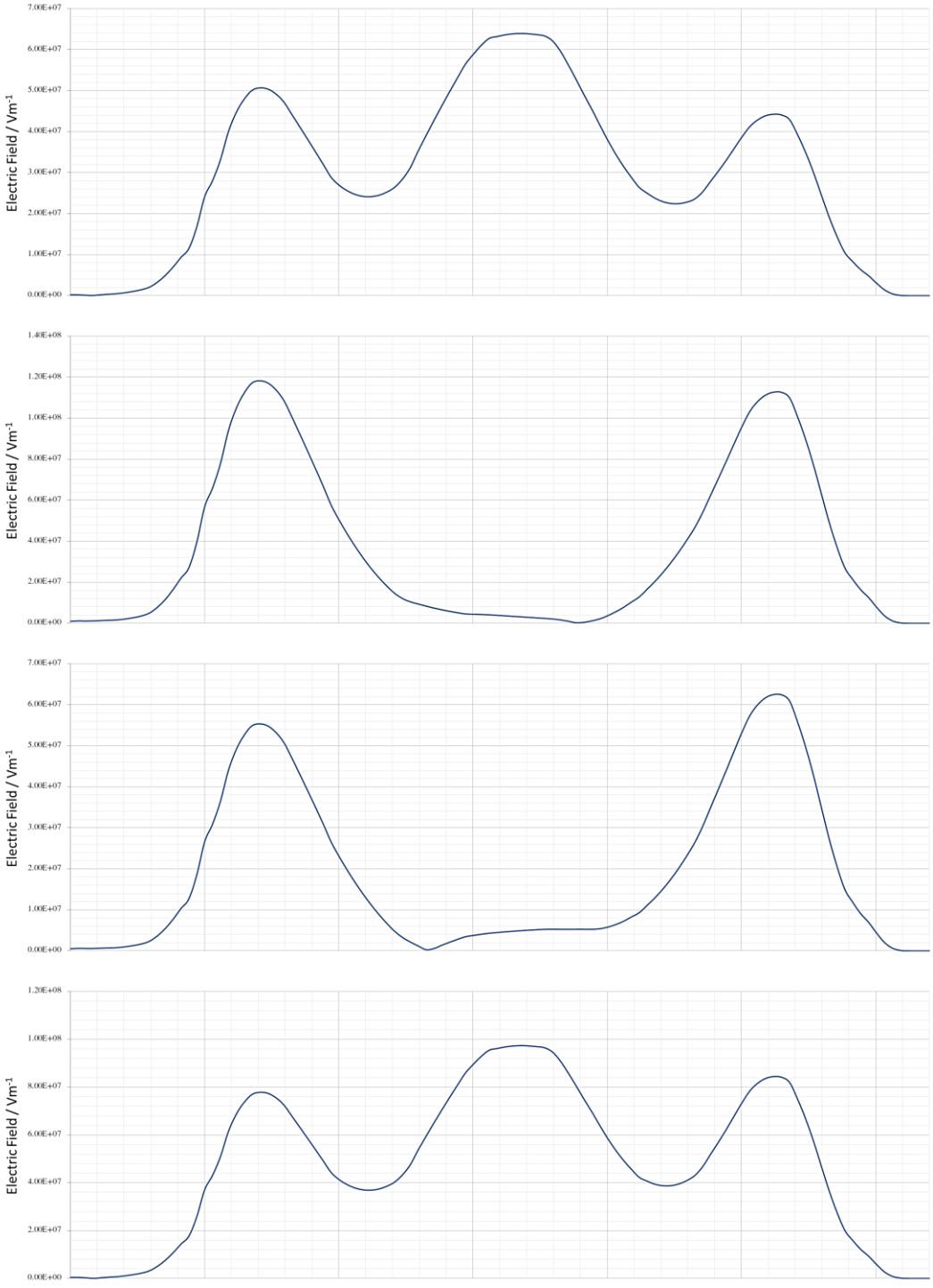

Figure 75 – Modes 1-4 from CST MWS

It was clear that the first 4 modes for the measured and simulated data were the same; the shape and magnitudes of the peaks aligned well with one another. However, although it can be said with certainty that the same modes are displayed, the two sets of data do differ in each case. This deviation is due to two main factors.

Firstly, the Bead-Pull VNA set-up could only measure the phase at finite intervals. This meant a discrete set of data was collected rather than a continuous. Furthermore, although the bead was pulled in very small increments, the small size of the structure, due to its low energy, meant that these intervals represented a significant section of the cavity's length. In addition to this, the momentum of each step combined with the elasticity of the thread meant that a small amount of jitter can be seen in the measured values. As previously discussed this was reduced by the use of Kevlar thread but, again, due to the cavity's small length, even a small amount of jitter can affect the results dramatically.

Secondly, materials used and manufacturing tolerances played a large part in the deviation between the simulated and measured data. The equipment available in the Lancaster University Engineering Department was not accurate enough to produce a structure which matched the design to the required tolerances. Furthermore, the structures could usually be made from a very high quality copper for optimum performance. However, due to budget restrictions and ease of machining, a relatively low quality aluminium was used.

However, the shapes and magnitudes of the measured data are close enough to the simulated results to confirm the possibility of constructing low cost prototypes capable of testing the feasibility of certain structures. Normally these structures have a very high cost of manufacture, in the range of tens to hundreds of thousands of pounds. If design mistakes or difficult geometries to machine are present, making a low cost prototype such as the one presented in this project allows a comparison between the desired and actual operation of the cavity as well as presenting any problems associated with manufacture.

6 Bead-Pull Measurements at the Cockcroft Institute

Due to interest in the cavity structure, following the Bead-Pull measurements taken using the constructed system, an invitation was extended to measure the cavity using a state of the art facility. The results from the measurements taken, using the same perturbing bead used at Lancaster University on the Bead-Pull built, are shown in Figure 76 and Figure 77. Again the mode at 3.079 GHz Only existed in the coupling cells and so is not included in the data set.

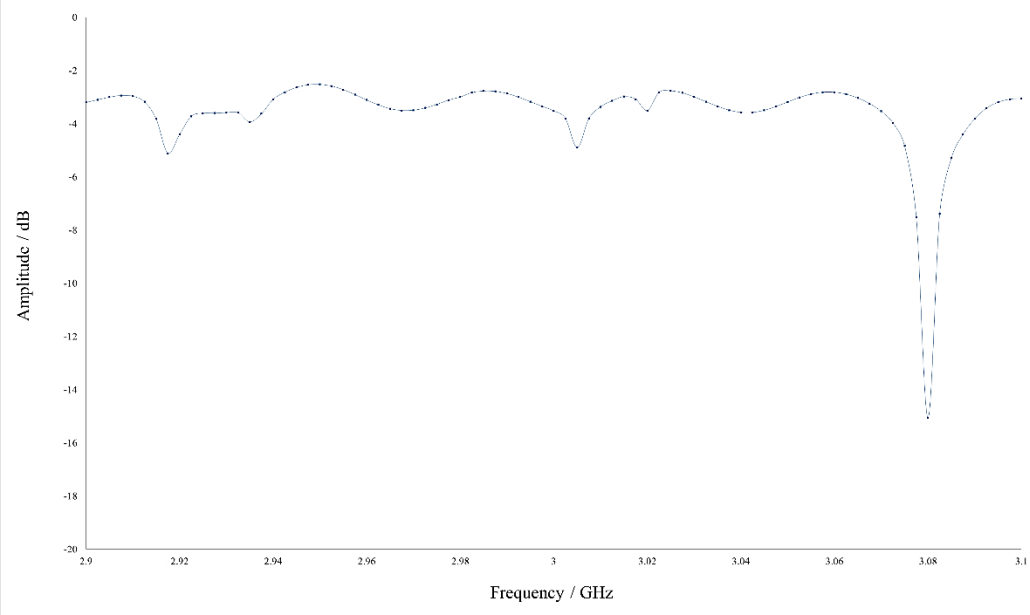

Figure 76 – Magnitude against Frequency Plot

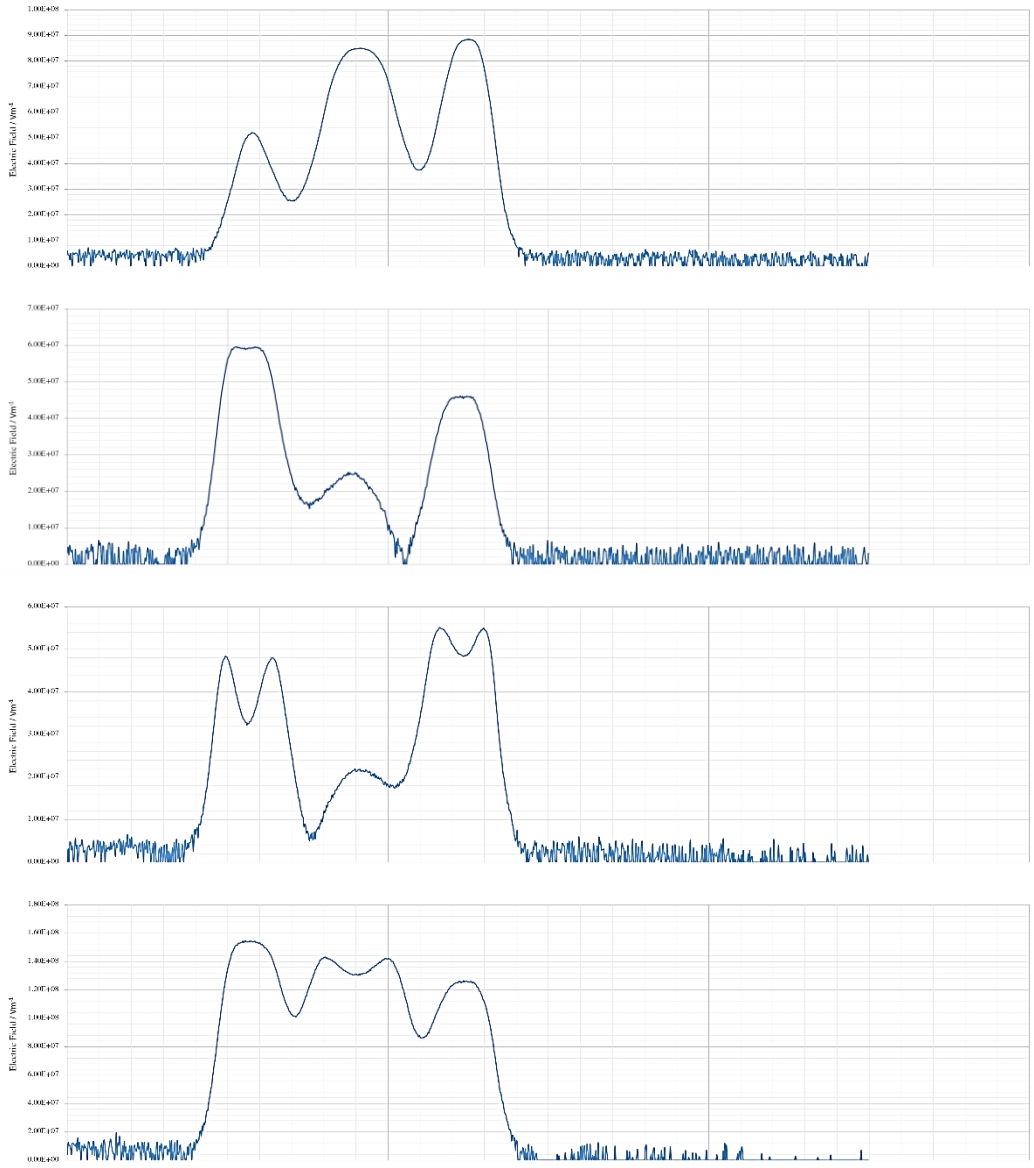

Figure 77 – Bead-Pull Measurements Taken at the Cockcroft Institute for the First 4 Modes (E_z on Axis Converted from S_{11} Phase Data)

Referring back to the data collected at Lancaster University using the Bead-Pull system built, Figure 74, the results, specifically the peak shapes, are almost identical. These results strengthen the accuracy of the Bead-Pull system designed and built for this project. Note, the Bead-Pull system used at the Cockcroft Institute was used in the opposite direction meaning the graphs are flipped in the y-plane.

Due to this accuracy, the slight difference between the measured results and the simulated results was questioned. Rather than using a metallic bead, which perturb both magnetic and electric fields, a

dielectric bead was used and the corresponding data, once converted to E_z on axis, is displayed in Figure 78.

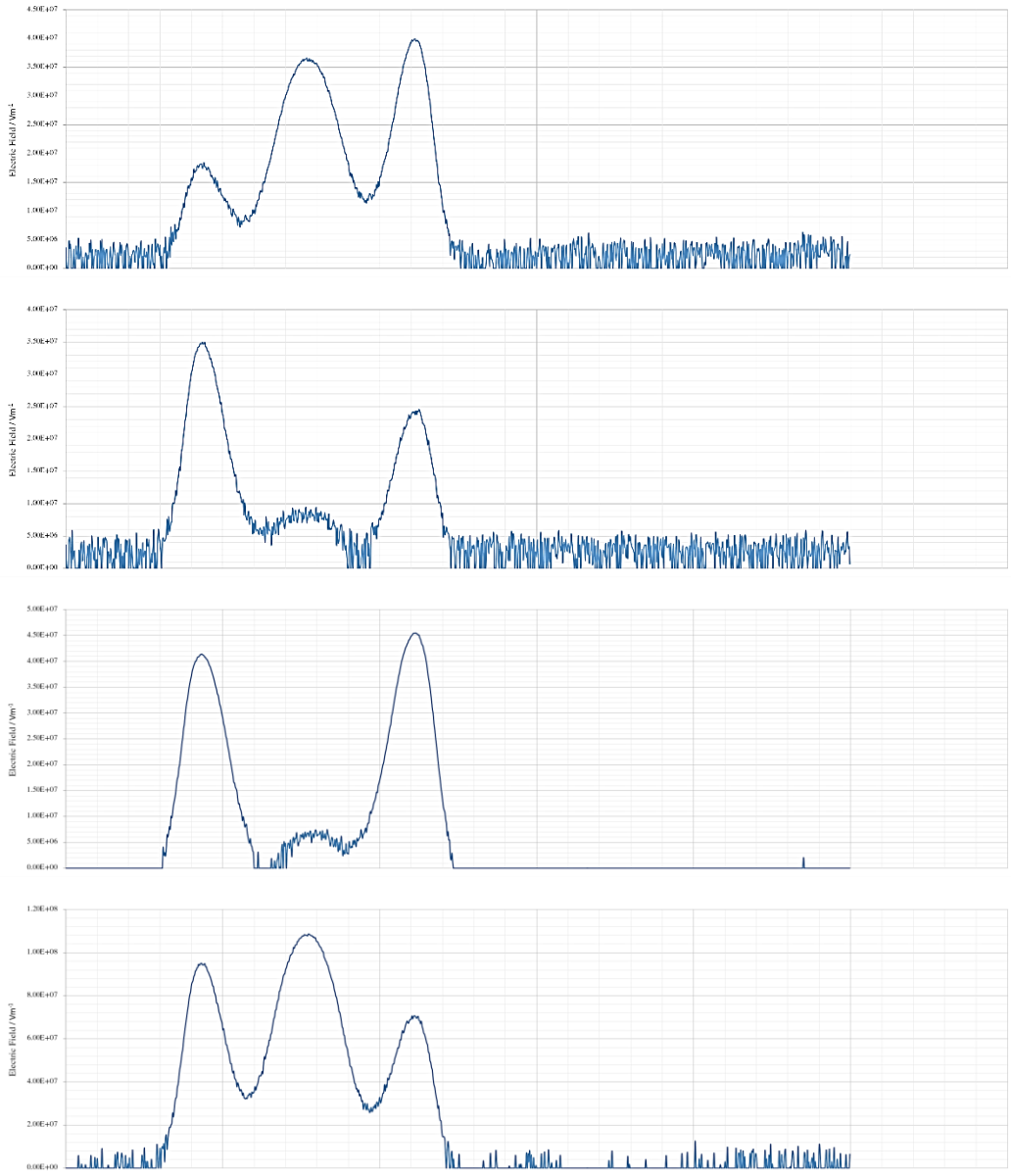

Figure 78 – Bead-Pull Measurements Taken at the Cockcroft Institute for the First 4 Modes Using a Dielectric Bead (E_z on Axis Converted from S_{11} Phase Data)

By using a dielectric bead, it was clear that the points at which the peaks inverted on the graphs gained with a metallic bead had been eradicated. This was because the dielectric bead only perturbed the electric fields within the cavity and thus the inverted peaks observed previously could conclusively be described

by areas of intense magnetic field. On further inspection these instances occurred when the metallic bead was in close proximity to the aluminium, i.e. at the nose cones. Returning back to CST, it was seen that there was a large magnetic field at the nose cones and this was due to optimising with respect to the modified poynting vector, where large surface currents are present.

CHAPTER 5 – CONCLUSION

1 Project Conclusion

Referring back to the project outline and aims:

- Both a side coupled and annular coupled structure were successfully implemented and optimised in CST Microwave Studio (CST MWS) with the same accelerating cavity and operating conditions.
- A new method of cavity implantation in CST MWS, devised for this project, allowed easier analysis and optimisation with respect to the modified poynting vector.
- Following the implementation and optimisation stage, the effect of side coupling and annular coupling was successfully compared with respect to the operational characteristics of the cavities.
- An article referencing the work on the annular coupled structure was written and included as part of the IPAC 15 proceedings [40].
- After achieving an optimised annular coupled design, alterations were made which allowed manufacture within the Lancaster University Engineering Department.
- CAD software was then used to implement the metallic housing for the cavity, in the form of aluminium discs, in order to allow the structure to be built using CNC lathes.
- Following the manufacturing stage, a Bead-Pull system, constructed as the cavity was being built to ensure no time was wasted, was designed and constructed. Measurements of the cavity's

phase were taken and converted in order to display the electric field at the beam axis for several modes.

- The Bead-Pull measurements were compared with those taken from a state of the art system, where the same modes were observed proving the success of the manufactured Bead-Pull.
- Measurement errors were then successfully solved by using a dialectic bead as well as a metallic one in order to conclusively assign the errors to the presence of large magnetic fields.

To conclude on the overall success of the project, all of the specified aims were achieved and each of the design, build and test stages were conducted creating an operational cavity. The cavity, designed to accelerate protons, was measured in terms of the electric field. The concordance of the measurements with the simulated data proved that the design, although slightly erroneous due to manufacturing tolerances and imperfect materials, would be able to do so at the specified energy and frequency.

2 Future Work

Due to the nature of optimisation theory, it is always possible to improve the performance of the structures designed. Due to this, the structures, specifically the ACS, will be further optimised by reducing the tolerances in order to provide a more efficient structure.

The possibility for inexpensive prototypes to be built for analysis will be promoted within the accelerator physics community of which this project will be used as an example. The feasibility of changing the two tiered system currently in place, where a cavity is built twice, to a three tiered one will be discussed.

Finally, the skills learnt and built upon during the course of this project will be utilised when conducting a PHD at the Cockcroft Institute and CERN.

CHAPTER 6 – FURTHER WORK CONDUCTED

1 Equivalent Circuit Design

2 Software Comparison – CST MWS and ANSYS' HFSS

CHAPTER 7 – REFERENCES

[1] M. Vretenar, "Lecture on Introductory Talk," *CAS RF School, Ebeltoft, Denmark,* 2010.

[2] P. J. Bryant, "Lectures on History and Applications of Accelerators," *CAS Introduction to Accelerator Physics, Varna, Bulgaira,* 2010.

[3] T. Wangler, RF Linear Accelerators, New York: John Wiley & Sons, 1998.

[4] M. Vretenar, "Linear Accelerators," *CERN, Geneva, Switzerland.*

[5] W. W. M. M. M. Conte, An Introduction to the Physics of Particle Accelerators, Singapore/New Jersey/London/Hong Kong: World Scientific Publishing, 2008.

[6] A. Sidorin, "Linear Accelerators," *Joint Institute for Nuclear Research, Joliot-Curie 6, Dubna, Russia.*

[7] M. Joyce, "Lecture on External Beam Therapy," *ENGR 361: Nuclear Medicine, Engineering Department, Lancaster University,* 2015.

[8] R. M. K. P. S. S. H. Owen, "Hadron Accelerators for Radio Therapy, Contemporary Physics," *Contemporary Physics, 55:2, 55-74, DOI: 10.1080/00107514.2014.891313,* 2014.

[9] P. B. K. C. D. T. M. W. R. Z. E. R. B. S. M. V. C. C. C. D. M. D. D. D. M. R. M. V. V. U. Amaldi, "LIBO - A Linac-booster for Protontherapy: Construction and Tests of a Prototype," *Nuclear Instruments and Methods in Physics Research Section A: Accelerators, Spectrometers, Detectors and Associated Equipment, 521(2), 512-529,* 2004.

[10] D. A. B. J. S. A. J. Wroe, "Immobilization Considerations for Proton Radiation Therapy," *Technol Cancer Res Treat, 13, 217-226, 2014, DOI: 10.7785/tcrt.2012.500376.*

[11] G. Burt, "Lecture on Introduction to RF Cavities for Accelerators," *The Cockroft Institute for Accelerator Science and Technology, Engineering Department, Lancaster University.*

[12] A. Gamp, "Lecture on Beam Cavity Interaction I," *CAS RF School 2010, Ebeltoft, Denmark.*

[13] J. Byrd, “Lecture on Resonant Cavities 1,” *U.S. Particle Accelerator School (USPAS).*

[14] J. Byrd, “ Lecture on Resonant Cavities, U.S. Particle Accelerator School (USPAS),” *2009.*

[15] F. Gerigk, “Cavity Types,” *CERN, Geneva, Switzerland,* 2011.

[16] G. Burt, “Lecture on Waveguides,” *ENGR 227: Electromagnetics and RF Engineering, Engineering Department, Lancaster University,* 2014.

[17] M. T. A. W. Chao, Handbook of Accelerator Physics and Engineering 2nd Printing, Singapore: World Scientific Publishing, 2002.

[18] F. Gerigk, “Lecture on Cavity Types,” *CAS RF School, Ebeltoft, Denmark,* 2010.

[19] G. Burt, “Lecture on Conductors, Dielectrics and Capacitance,” *ENGR 227: Electromagnetics and RF Engineering, Engineering Department, Lancaster University,* 2014.

[20] H. Wiedemann, Particle Accelerator Physics Third Edition, New York, USA: Springer Berlin Heidelberg, 2007.

[21] G. Burt, “Lecture on Striplines and Microstrip,” *ENGR 227: Electromagnetics and RF Engineering, Engineering Department, Lancaster University,* 2014.

[22] Y. M. K. Y. Y. Y. T. Kageyama, “Development of Annular Coupled Structure,” *KEK, National Laboratory for High Energy Physics, Japan, Proceedings of the 1992 Linear Accelerator Conference, Ottawa, Ontario, Canada,* 1992.

[23] V. V. Paramonov, “The Summary for Optimization of the Annular Coupled Structure Accelerating Module Physical Design for High Intensity Hadron Linac,” *KEK, Tsukuba,* 2013.

[24] T. D. J. Q. L. Y. S. J. H. S. D. T. D. X. C. B. L. Y. Z. Y. H. W. S. Xiang, “A portable X-band on-axis standing wave linac structure, Department of Engineering Physics, Tsinghua University, Beijing 100084, PRChina, In Particle Accelerator Confe”.

[25] L. K. a. V. Paramonov, “The On-Axis Accelerating Structure for Application in Proton Linacs with Moderate Heat Loading,” *Institute for Nuclear Research of the RAS, 117312, Moscow, Russia, In Proceedings of the 1996 Linac Conference, Geneva.*

[26] K. Wille, The Physics of Particle Accelerators, New York: Oxford University Press, 2000.

[27] J. D. P. S. H. H. Q. W. Z. Y. &. X. L. H. Li, “Design of a 325MHz Beta = 0.12 Superconducting Single Spoke Cavity for China-ADS,” *Chinese Physics C,* 2013.

[28] S. N. V. L. J.-F. O. N. P. E. G.-W. I. G. G. R. S. K. V. Y. N. Solyak, “The Concept Design of the CW Linac of the Project-X,” *Fermilab, Batavia, IL 60510, USA, Proceedings of IPAC’10, Kyoto, Japan,* 2010.

[29] C. P. Berra, “Construction et essai d'un accélérateur linéaire à protons impulsé à 3 GHz (LIBO) pour la thérapie du cancer,” *Doctoral Dissertation, Lyon, IPN,* 2005.

[30] P. B. E. R. M. V. U. A. K. C. D. T. M. W. R. Z. C. C. D. G. C. D. M. D. D. M. M. V. V. B. Szeless, “Sucessful High Power Test of a Proton Linac Booster (LIBO) Prototype for Hadrontherapy,” *A Collaboration of CERN, TERA & INFN, In Particle Accelerator Conference 2001, Proceedings of the 2001 (Vol. 1, pp. 642-644) IEEE.*

[31] A. D. M. R. M. S. T. C. A. C. R. V. V. C. D. M. D. G. M. M. R. J. R. V. G. Vaccaro, “Optimisation Design of a Side Coupled Linac (SLC) for Proton Therapy: A New Feeding Solution,” *A Collaboration of INFN, CERN & e2v, Proceedings of EPAC 2006, Edinburgh, Scotland,* 2006.

[32] A. Degiovanni, “HIGH GRADIENT PROTON LINACS,” École Polytechnique Fédérale de Lausanne, Lausanne, 2013.

[33] G. Burt, “Lecture on RF Linear Accelerators L1&2: Introduction: DC and Coupled Cavity Linacs,” Postgraduate Lecture Programme, The Cockroft Institute for Accelerator Science and Technology.

[34] S. M. E. R. B. S. M. V. U. A. K. C. D. T. M. R. Z. C. C. D. G. C. D. M. D. D. M. R. M. V. G. V. P. Berra, “STUDY, CONSTRUCTION AND TEST OF A 3 GHZ PROTON LINAC-BOOSTER (LIBO) FOR CANCER THERAPY,” *Proceedings of the European Particle Acceleration Conference on EPAC,* vol. 2495, no. 2497, p. 2495, 2000.

[35] C. B. D. G. L. S. P. B. E. R. B. S. U. A. K. C. M. M. D. T. M. R. Z. M. R. M. V. G. V. L. C. A. R. C. De Martinis, “BEAM TESTS ON A PROTON LINAC BOOSTER FOR HADRONTHERAPY,” *Proceedings of EPAC 2002, Paris, France,* pp. 2727-2729, 2002.

[36] S. C. W. W. A. Grudiev, “New local field quantity describing the high gradient limit of accelerating structures,” *PHYSICAL REVIEW SPECIAL TOPICS - ACCELERATORS AND BEAMS,* pp. 102001-1 - 102001-9, 26 October 2009.

[37] J. Koech, “Bead-Pull RF Measurement System,” *Summer Internships in Science and Technology (SIST),* 2011.

[38] T. G. Jurgens, “Equations for Bead Pull Cavity Measurements,” *FERMILAB-LU-159,* 1990.

[39] L. P. D. A. L. F. B. S. A. Mostacci, “ABOUT NON RESONANT PERTURBATION FIELD MEASUREMENT IN STANDING WAVE CAVITIES,” *Proceedings of PAC09, Vancouver, BC, Canada.*

[40] G. B. J. M. S. P. H. O. A. D. R. Apsimon, "ProTec - A NORMAL-CONDUCTING CYCLINAC FOR PROTON," *IPAC'15,* 2015.

[41] M. Vretenar, "Lecture on Low-Beta Structures," *CAS RF School, Ebeltoft, Denmark,* 2010.

[42] P. B. K. C. D. T. M. W. R. Z. E. R. B. S. M. V. C. C. C. D. M. D. G. D. D. M. M. V. V. U. Amaldi.

CHAPTER 7 – APPENDIX

1 Project Plan

The project plan was written in December 2014, it has been place in the appendix as a reference for not only the stages necessary to complete the aims of the project, but also to compare the progress made with the stages planned and the deadlines set.

1.1 Project Outline

An application of particle accelerators, and therefore an area of interest for the accelerator engineer, is cancer therapy. By directing a charged particle at cancerous tissue, it is possible to damage the cells and remove the cancer.

Specifically, it is possible to use a radio frequency (RF) linear accelerator (linac) in order to accelerate the charged particle to a specific energy. There are an array of particles available for acceleration, but a particle of much interest in the area of cancer therapy is the proton. The proton possesses characteristics which made it ideal for irradiating cancers without harming surrounding tissues and with a much lower likelihood of a secondary cancer arising when compared with other charged particles. For these reasons therapy using protons, or hadron therapy, has applications in treating cancers near vital organs and as a treatment for children.

Due to the applications of RF linear accelerators for hadron therapy, this project will consist of the design, build and test of an RF linac cavity. The cavity is the structure responsible for accelerating the charged

particles, in this case protons, and specifically, an RF cavity uses radio frequencies to transfer electromagnetic energy to the particle beam.

The cavity will firstly be virtually designed on CST Microwave Studio. At this stage the cavity will be optimised iteratively in order to produce a structure which is capable of efficiently accelerating a beam of protons at the required energy. Several figures of merit will be calculated throughout the optimisation stage and these values will be developed, allowing them to act as assessments of the cavity's performance in order for comparison with existing structures.

Following the design stage, the cavity will be implemented using the computer aided design (CAD) program Solidworks and built from aluminium using a lathe. This physical structure will then be tested in the RF laboratory and the results from the tests will be compared to the values returned virtually from simulations in CST Microwave Studio.

1.2 Aims of the Project

To increase productivity and to successfully meet the criterion set by the project supervisor, Dr G. Burt, a definitive list of aims were established. These aims represented key points to be met in order for the project to be deemed successful. They consisted of:

1. Become competent with the software program CST Microwave Studio.
2. Reproduce an existing RF cavity virtually; optimising for new performance criterion.
3. Virtually design a new RF cavity to meet specified performance criterion.
4. Implement the designed RF cavity in CAD software.
5. Build the designed RF cavity.
6. Design and build the testing setup.
7. Test the built RF cavity.

Analyse the performance of the RF cavity; comparing the built cavities operation to the virtual version simulated using CST Microwave studio.

These aims were accepted by Dr G. Burt, eliminating any possible lack of understanding regarding the required goals and outcomes of the project.

1.3 Project Breakdown

After defining the aims of the project, a step by step task breakdown was constructed. The tasks were designed to ensure completion of each aim, allowing the specific objectives that determine project success to be completed. As well as processes for the design, build and test of the RF cavity, tasks for the project write-up, presentations and deadlines were included in order to minimise the risk of late submission and to manage time efficiently throughout the project.

Conversing with Dr G. Burt and referring to the aims set out with him, a definitive list of all the tasks necessary to complete the design, build and test of the cavity were set out in a spreadsheet. Using the Lancaster University Engineering Third Year Project Handbook, the necessary tasks for the project write-up and student presentations were collated and entered into the same spreadsheet.

In terms of time management, deliverables in the form of deadlines were inputted into the spreadsheet and the tasks needed to meet these targets were scheduled to be completed before the deadline to act as a contingency in case more time than anticipated was needed. Following this, the processes for the design, build and test of the cavity were scheduled, taking into account the key deadlines set out by the Lancaster University Engineering Department and their associated tasks.

Following the completion of the list of tasks and the dates they were to be carried out over, the spreadsheet was copied into Microsoft Project and formatted into a Gantt Chart.

1.3.1 Gantt Chart

1.3.2 Difficulties and Responsibilities

When planning the project, several problems had to be overcome in order to have all of the tasks shown on the Gantt Chart completed by the set dates.

The first problem encountered when scheduling tasks was the timing of third year exams. Not only did the dates of these exams have to be taken into account, but the time necessary for revision prior to these dates also needed to be thought about. The Gantt Chart shows a very limited amount of work in April and May 2015, not only this but the only work scheduled for the Easter break, a key time for revision, is formatting the report, preparing for the Viva (interview) and constructing the poster. These are all processes that can be carried out around revision, at any time of any day.

Another foreseeable problem was the fact that, in January 2015, there would be a transition from one Engineering Building to another. As this project consists of virtual simulations, the mechanical labs would not be required until after these dates. However, many students would experience a delay and for this reason it was thought that the technicians would have an excess amount of work. Therefore, conversations and meetings with technicians were planned to be scheduled much earlier than the build and test dates to ensure that the correct expertise and help is received before construction.

Finally, holidays had to be taken into account. During the holidays there would be a lack of staff in the department and it would prove more difficult to access the mechanical labs. For this reason any mechanical work has been planned around holiday times and the dates for holidays are clearly marked on the Gantt Chart.

1.3.3 Further Breakdown

After the completion of the Gantt chart the deliverables were separated from the other tasks. The deliverables were compiled into tabular form allowing a definitive list of all deadlines. Following this, another table was constructed, displaying the key milestones which signified the completion of various

stages. The tasks were broken down into subtasks and, for the more complex ones, described to detail the methods used to undertake them. Each task has also been associated with a time in order to assess whether the work is enough to fulfil the 300 hour project criterion set by Lancaster University.

1.3.3.1 Key Milestones and Deliverables

Table 1 and 2 display the project deliverables and milestones respectively.

Table 20 – Key Deliverables

Deliverable	Date Due
Literature Review	31/10/2014
Risk Assessment List	07/11/2014
Full Risk Assessment	12/01/2015
Project Plan	16/01/2015
Presentation	16/01/2015
Final Report	29/05/2015
Viva	04/06/2015
Poster	05/06/2015
Poster Presentation	25/06/2015

Table 21 - Milestones

Milestone	Date
Complete Design Stage	13/02/2015
Produce Physical Structure	20/03/2015

1.3.3.2 Task Breakdown and Description

1 Preliminary Reading – 5 Hours

1.1 Collate relevant articles, scientific paper and other literature to research the field

2 Compose Literature Review – 35 Hours

2.1 Use relevant collated literature to create a document which outlines key concepts related to the project and which covers all of the necessary topics in order to gain a sufficient understanding of the field.

2.2 Ensure the marking scheme found in the Lancaster University Engineering Third Year Project Handbook is fulfilled.

3 Compose Risk Assessment List – 1 Hour

3.1 Copy the risk assessment list form from Moodle.

3.2 List the necessary risk assessments that will need to be carried out in order to safely undertake each project task.

3.3 Confirm with Dr G. Burt.

4 Full Risk Assessment – 2 Hours

4.1 Complete the risk assessments listed in the risk assessment list.

4.2 Confirm with Dr G. Burt.

5 Construct Project Plan – 20 Hours

5.1 Create Gantt Chart

5.1.1 Collate each major task, deadline and any relevant dates into a spreadsheet.

5.1.2 Plan start and end dates for each task, bearing in mind any deadlines, time for other work and holiday time.

5.1.3 Copy the spreadsheet into Microsoft Project and format as a Gantt Chart.

5.2 Create risk Register

5.2.1 Make a list of events that could occur which would act as a risk to project success.

5.2.2 For each risk assign a number from 1 to 3 for probability and a number from 1 to 3 for the potential impact on project success.

5.2.3 By multiplying the two numbers assigned to each event assign a number from 1 to 9 to each event to represent the weight of each risk.

5.2.4 Compose mitigations and contingencies for each risk. A mitigation is a procedure that prevents the risk from effecting the project and a contingency is the process necessary if the mitigation is not successful.

5.3 Edit the Gantt Chart and Risk Register into a document fulfilling all other criterion set out in the Project Plan marking scheme located in the Lancaster University Engineering Third Year Project Handbook.

6 Build Skills Using CST Microwave Studio – 5 Hours

6.1 Re-cap work done last year using CST Microwave Studio in ENGR 227: Electromagnetics and RF Engineering.

6.2 Work through in-built tutorials.

6.3 Work through online tutorials on websites such as YouTube

7 Virtually Implement the LIBO Structure – 40 Hours

The LIBO structure, an existing linear accelerator, will be implemented using the software program CST Microwave Studio. This program allows cavities, made from specified materials, to be built and assessed in terms of their properties when an RF field is applied. It can also return several figures of merit specific to cavity design, allowing operational assessment of the structure without actually building it.

The cavity will therefore be built to fulfil several operational criterion. The main three of which can be said to be: operation at 24 MeV, resonant frequency of 3 GHz at the correct modes of operation and a coupling coefficient (K) of 4.5%. For clarity and efficiency, a breakdown of the tasks needed to perform these criterion has been constructed.

7.1 Sketch the cavity – parameterising each dimension and noting down what each parameter refers to on the sketch.

7.2 Sweep the sketch though a circular path, creating the 3D structure.

7.3 Collect the specified operational characteristics from Dr G. Burt.

7.4 Calculate the width of the structure and change the relevant parameters.

7.5 Use parameter sweeps to optimise the dimensions of the structure in order to operate at the resonant frequency specified.

7.6 Optimise the Coupling parameters until the specified coupling coefficient is met.

7.7 Re-tune for the operational frequency.

7.8 Simulate for set figures of merit and calculate the modified pointing vector.

8 Virtually Implement the Annular Coupled Structure – 60 Hours

Following the virtual implementation of the LIBO structure using CST Microwave Studio, the cavity to be built will be designed and optimised in the same manner. This time the design stage will be much more time consuming as the features of the cavity will not be referenced to an existing structure but will have to be designed from scratch. However this will be compensated by the increased skill in using the program gained from designing the LIBO structure.

Once designed, the annular coupled structure (ACS) will be optimised as before and to the same specified values as the LIBO structure. This will provide a comparison of operational characteristics between the LIBO and the ACS. This comparison will act as a performance rating for the cavity, as it will be compared to an existing structure (even though at a different energy range). In terms of a list of sub-tasks necessary to complete this stage, the same tasks as for the LIBO structure will be carried out although, as described, some will vary in complexity.

8.1 Sketch the cavity – parameterising each dimension and noting down what each parameter refers to on the sketch.

8.2 Sweep the sketch though a circular path, creating the 3D structure.

8.3 Collect the specified operational characteristics from Dr G. Burt.

8.4 Calculate the width of the structure and change the relevant parameters.

8.5 Use parameter sweeps to optimise the dimensions of the structure in order to operate at the resonant frequency specified.

8.6 Optimise the Coupling parameters until the specified coupling coefficient is met.

8.7 Re-tune for the operational frequency.

8.8 Simulate for set figures of merit and calculate the modified pointing vector.

9 Compose and Prepare Presentation – 10 Hours

A presentation will be constructed that details the project including what has already been done and what there is planned to do. The presentation will consist of a Microsoft PowerPoint presentation which will assist the content being relayed with visual aids and key bullet points. The presentation will not be tailored around the difficult technical aspects of the project but will rather seek to present and describe the processes to be undertaken in a way in which somebody being introduced to the concepts will understand. However the audience will be engineers and lecturers at a university, therefore there will be a small amount of technical content aimed at the undergraduate engineer.

9.1 Write a 10 minute presentation detailing project background, work done so far and work to be carried out.

9.2 Ensure all criterion set out in the Presentation marking scheme located in the Lancaster University Engineering Third Year Project Handbook is fulfilled.

10 Design Structure Using SolidWorks – 5 Hours

10.1 Implement the optimised annular coupled structure design in SolidWorks.

11 Converse with Technicians Regarding Construction – 1 Hour

In order to construct the cavity, engineering technicians at the university will be needed to assist in setting up and using the lathes and other machinery. Factors such as the change of engineering building and the

overload of the technicians may create a backlog of work and due to this, the technicians will be spoken to early on with respect to cavity construction.

11.1 Find out the best methods of construction and common errors encountered.

11.2 Finalise dates for construction with the technicians.

12 Commence Build of Annular Coupled Structure – 15 Hours

13 Design Testing Set-Up – 5 Hours

In order to design the testing set-up, technicians and RF engineers will have to be conversed with in order to see which pieces of equipment are available for use and at which times they will be available. By scheduling a time slot the testing will not be delayed and will not throw the project off-track.

14 Test Annular Coupled Structure – 15 Hours

15 Design Higher Voltage Annular Coupled Structure – 20 Hours

15.1 Optimise the design again in CST Microwave Studio, but for a larger operational voltage.

16 Project Write Up – 60 Hours

17 Format Written Repot – 5 Hours

17.1 Ensure all content is included and formatted as specified in the Lancaster University Engineering Third Year Project Handbook.

18 Prepare for Viva – 5 Hours

18.1 Ensure all lab books are complete.

18.2 Prepare for interview-type questions.

19 Construct Poster – 5 Hours

19.1 Produce A2 poster which includes all of the points listed in the Lancaster University Engineering Third Year Project Handbook.

20 Prepare for Poster Presentation – 2 Hours

The total amount of estimated time spent on the project, from each of the listed tasks, was calculated to be 326 hours. This value is within ten percent of the 300 hour target and therefore the task lengths were seen to be applicable for a project of this type.

1.4 Risks to Project Success

A risk register was produced in order to assess factors which could pose as a risk to project success, analyse the weight of each risk and come up with mitigations and contingencies for each factor.

1.4.1 Risk Register

1.5 Brief Summary of Work Done to Date

Referring back to the project breakdown, each process up to step 12 has successfully been completed and, in terms of time management, the Gantt chart has been followed accurately. At this stage step 12 is underway and the annular coupled structure is being designed using CST Microwave Studio.

To represent the work done on the project thus far, once the literature review, risk assessment list, risk assessments and project plan (minus this section) were completed, the cavity design stage using CST Microwave Studio was started.

1.5.1 Cavity Design Stage

1.5.1.1 LIBO Structure

Firstly, as depicted in the project breakdown, previous work and tutorials were undertaken in order to gain familiarity with the software. A patch antenna was firstly made, followed by a hollow cylinder and a dipole antenna, Figure 79.

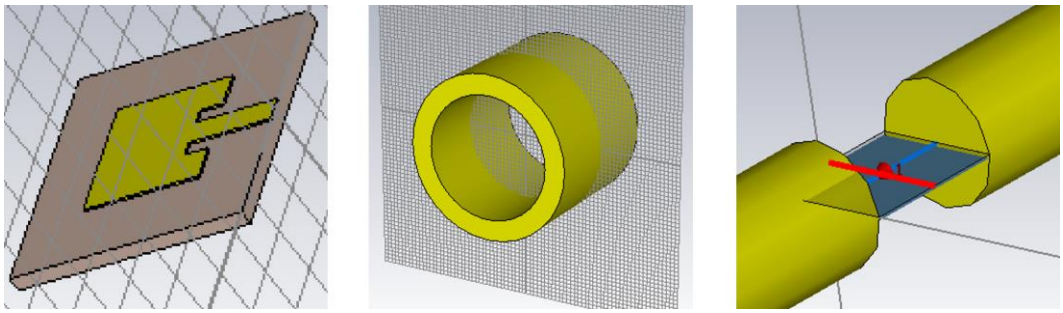

Figure 79 – Building Skills in CST MWS

Following this, as skills using CST Microwave studio had been built upon, the LIBO structure was then implemented using the software. Fistly, as specified in the project breakdown, the necessary dimensions of the structure were sketched and each dimension parametersied. The sketch, list of parameters and what these parameters prepresent can be seen in Figure 80.

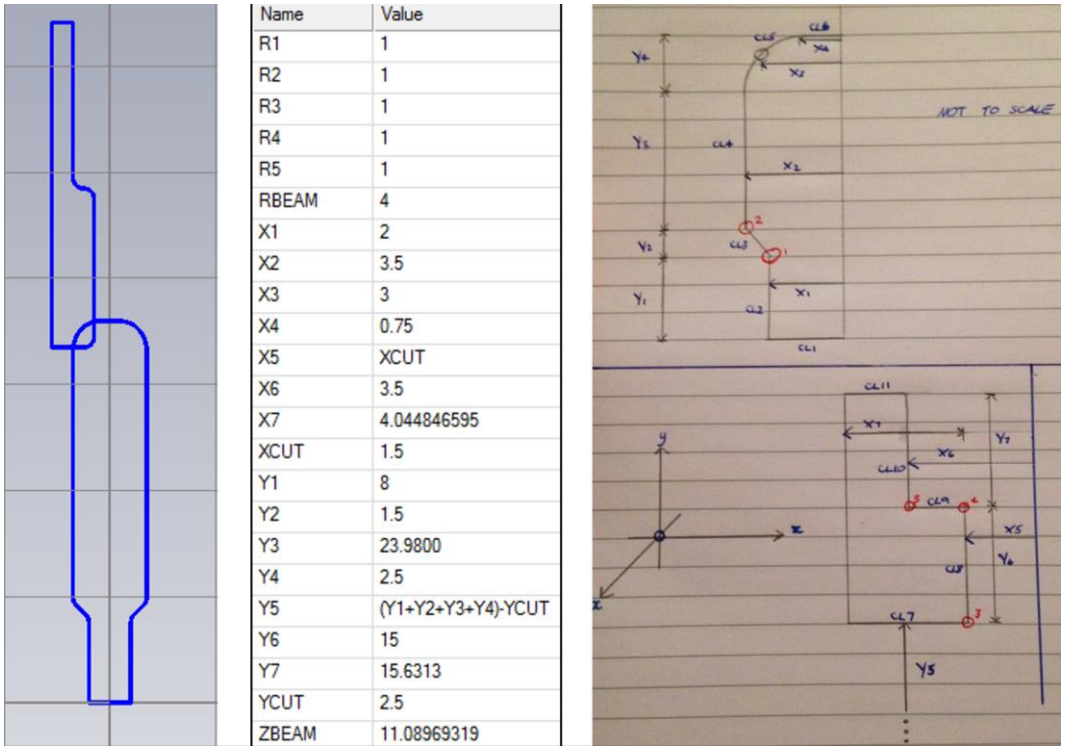

Name	Value
R1	1
R2	1
R3	1
R4	1
R5	1
RBEAM	4
X1	2
X2	3.5
X3	3
X4	0.75
X5	XCUT
X6	3.5
X7	4.044846595
XCUT	1.5
Y1	8
Y2	1.5
Y3	23.9800
Y4	2.5
Y5	(Y1+Y2+Y3+Y4)-YCUT
Y6	15
Y7	15.6313
YCUT	2.5
ZBEAM	11.08969319

Figure 80 – Initial LIBO Parameters

The sketch was then mirrored and swept around cricular paths in order to create the unit cell of the LIBO structure consisting of one accelerating cell and two half coupling cells. Once created, the unit cell was firstly set to a width that allowed acceleration at the correct energy. The structure was then optimised using parameter sweeps of several dimensions in order to return the correct accelerating and coupling modes at 3 GHz operational frequency. The optimised unit cell can be seen in Figure 81.

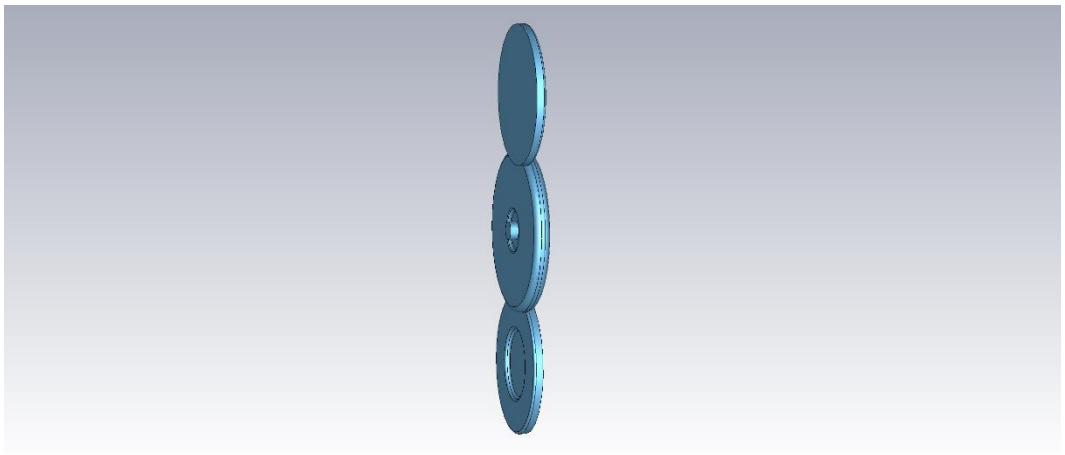

Figure 81 – Initial LIBO Structure

After the correct frequency in each operational mode was found, the intersection between the accelerating and coupling cells was changed in order to produce a coupling constant (K) of 4.5%. This value was found by using parameter sweeps and after a value of 4.5% was found the structure was re-tuned to get back to 3 GHz for each operational mode. This altered the K value so the intersection had to change once more. This iterative process was carried out until both values for the frequency and the coupling constant were met to the required level of accuracy.

Following the completion of the optmisation of the structure, several figures of merit were calculated or simulated in order to provide values for analysis. After the fist LIBO structure was completed, another version was designed to operate at a different energy. This allowed for comparison between operational characteristics at two energies (110 MeV and 24 MeV).

1.5.1.2 Annular Coupled Structure (ACS)

After completion of the LIBO structures, the cavity to be built was then sketched, designed and parameterised in CST Microwave Studio. This was done in the same way as the LIBO structure, meaning the process was much faster this time.

As before the structure was then altered in order to achieve operation at the correct energy and then optimised to achieve operation at 3GHz.

This is the stage of the project that has been reached at this current moment in time. A cross section of the structure thus far is shown in Figure 82.

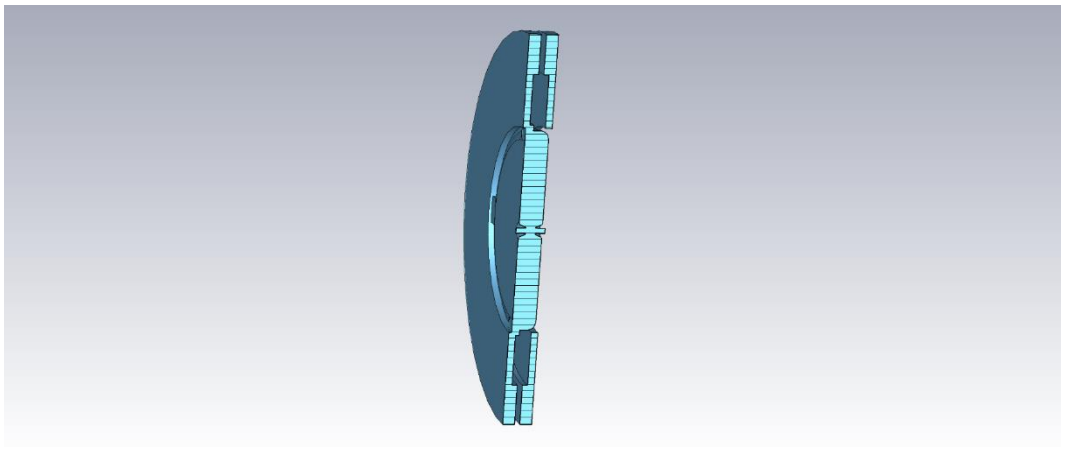

Figure 82 – ACS (Progress Thus Far)

2 Solidworks Drawing Sheets

3 Simulation Data